

AFRL-ML-WP-TR-2002-4060

AEROSPACE COMPOSITE MATERIALS

**Delivery Order 0002: Development and
Validation of Micromechanical Models for
Composites**



V. Buryachenko

E. Iarve

R. Kim

S. Sih

G. P. Tandon

**University of Dayton Research Institute
300 College Park Avenue
Dayton, OH 45469-0168**

MARCH 2002

Interim Report for 30 November 2000 – 29 November 2001

Approved for public release; distribution is unlimited.

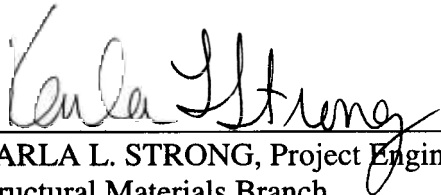
**MATERIALS AND MANUFACTURING DIRECTORATE
AIR FORCE RESEARCH LABORATORY
AIR FORCE MATERIEL COMMAND
WRIGHT-PATTERSON AIR FORCE BASE, OH 45433-7750**

NOTICE

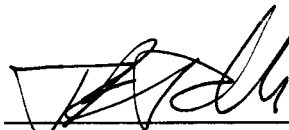
Using government drawings, specifications, or other data included in this document for any purpose other than government procurement does not in any way obligate the U.S. Government. The fact that the government formulated or supplied the drawings, specifications, or other data does not license the holder or any other person or corporation; or convey and rights or permission to manufacture, use, or sell any patented invention that may relate to them.

This report has been reviewed by the Office of Public Affairs (ASC/PA) and is releasable to the National Technical Information Service (NTIS). At NTIS, it will be available to the general public, including foreign nations.

This technical report has been reviewed and is approved for publication.



KARLA L. STRONG, Project Engineer
Structural Materials Branch
Nonmetallic Materials Division



TIA BENSON TOLLE, Acting Chief
Structural Materials Branch
Nonmetallic Materials Division



ROBERT M. SUSNIK, Deputy Chief
Nonmetallic Materials Division
Materials and Manufacturing Directorate

Copies of this report should not be returned unless return is required by security considerations, contractual obligations, or notice on a specific document.

REPORT DOCUMENTATION PAGE					Form Approved OMB No. 0704-0188	
<p>The public reporting burden for this collection of information is estimated to average 1 hour per response, including the time for reviewing instructions, searching existing data sources, gathering and maintaining the data needed, and completing and reviewing the collection of information. Send comments regarding this burden estimate or any other aspect of this collection of information, including suggestions for reducing this burden, to Department of Defense, Washington Headquarters Services, Directorate for Information Operations and Reports (0704-0188), 1215 Jefferson Davis Highway, Suite 1204, Arlington, VA 22202-4302. Respondents should be aware that notwithstanding any other provision of law, no person shall be subject to any penalty for failing to comply with a collection of information if it does not display a currently valid OMB control number. PLEASE DO NOT RETURN YOUR FORM TO THE ABOVE ADDRESS.</p>						
1. REPORT DATE (DD-MM-YY) March 2002		2. REPORT TYPE Interim		3. DATES COVERED (From - To) 11/30/2000 – 11/29/2001		
4. TITLE AND SUBTITLE AEROSPACE COMPOSITE MATERIALS Delivery Order 0002: Development and Validation of Micromechanical Models for Composites				5a. CONTRACT NUMBER F33615-00-D-5006		
				5b. GRANT NUMBER		
				5c. PROGRAM ELEMENT NUMBER 62102F		
6. AUTHOR(S) V. Buryachenko E. Iarve R. Kim S. Sih G. P. Tandon				5d. PROJECT NUMBER 4347		
				5e. TASK NUMBER 32		
				5f. WORK UNIT NUMBER 02		
7. PERFORMING ORGANIZATION NAME(S) AND ADDRESS(ES) University of Dayton Research Institute 300 College Park Avenue Dayton, Ohio 45469-0168				8. PERFORMING ORGANIZATION REPORT NUMBER UDR-TR-2002-00033		
9. SPONSORING/MONITORING AGENCY NAME(S) AND ADDRESS(ES) Materials and Manufacturing Directorate Air Force Research Laboratory Air Force Materiel Command Wright-Patterson Air Force Base, OH 45433-7750				10. SPONSORING/MONITORING AGENCY ACRONYM(S) AFRL/MLBCO		
				11. SPONSORING/MONITORING AGENCY REPORT NUMBER(S) AFRL-ML-WP-TR-2002-4060		
12. DISTRIBUTION/AVAILABILITY STATEMENT Approved for public release; distribution is unlimited.						
13. SUPPLEMENTARY NOTES Report contains color.						
14. ABSTRACT (Maximum 200 Words) Mechanics modeling and verification of a variety of systems continues to be examined. Systems successfully examined include the single filament cruciform test, identification of failure modes in composites, woven fabric composite, carbon foams, the fiber pushout test, and slanted free-edge plies. Techniques used include concentric cylinder modeling, finite element method, B-spline approximation, and in situ observation of damage during testing via scanning electron microscopy (SEM). The iteration method was found to be superior to the Fourier transform method of modeling inhomogeneous composites except where an analytical solution is required. This knowledge was then applied to functionally graded materials and to computer-generated models of locally nonuniform composites. The radial distribution function for fiber locations and second-order intensity functions are needed to predict properties beyond estimating their bounds.						
15. SUBJECT TERMS mechanics modeling, micromechanics, elastic modulus, tensile strength, Young's modulus, cruciform test, epoxy composites, carbon foams, axisymmetric damage model, finite element method, FEM, B-spline approximation, B-SAM, woven composite, fiber pushout test, free-edge analysis, microstructure, SEM, random structures, iteration method, Fourier transform method, radial distribution function, statistical second-order quantities						
16. SECURITY CLASSIFICATION OF:			17. LIMITATION OF ABSTRACT: SAR	18. NUMBER OF PAGES 170	19a. NAME OF RESPONSIBLE PERSON (Monitor) Karla L. Strong 19b. TELEPHONE NUMBER (Include Area Code) (937) 255-3104	
a. REPORT Unclassified	b. ABSTRACT Unclassified	c. THIS PAGE Unclassified				

TABLE OF CONTENTS

<u>Section</u>		<u>Page</u>
	EXECUTIVE SUMMARY	1
1	MIXED-MODE FAILURE CRITERIA USING CRUCIFORM GEOMETRY	4
1.1	SUMMARY AND RECOMMENDATIONS	12
2	DAMAGE EVOLUTION AND FAILURE MODELING IN UNIDIRECTIONAL GRAPHITE/BMI COMPOSITE	13
2.1	SUMMARY AND RECOMMENDATIONS	23
3	MICROMECHANICAL RESPONSE OF A MULTIPHASE COMPOSITE	24
4	SINGLE-FIBER PUSHOUT CONSIDERING INTERFACIAL FRICTION AND ADHESION	31
5	PARAMETRIC DESIGN, ANALYSIS, AND TESTING OF A MODEL WOVEN COMPOSITE WITH A CRUCIFORM GEOMETRIC CONFIGURATION	33
5.1	NUMERICAL RESULTS AND PARAMETRIC STUDY	35
5.1.1	Unit Cell of Plain-Weave Composite	35
5.1.2	One-Dimensional Model Laminate with Cruciform Geometry	38
5.2	EXPERIMENT AND VALIDATION	42
5.3	SUMMARY AND RECOMMENDATIONS	44
6	ASYMPTOTIC STRESS ANALYSIS OF LAMINATED COMPOSITES WITH SLANTED FREE EDGE	47
6.1	ASYMPTOTIC ANALYSIS	48
6.2	FULL-FIELD NUMERICAL CALCULATION	55
6.3	RESULTS	59
6.4	SUMMARY AND RECOMMENDATIONS	77
7	MECHANICAL MODELING AND PREDICTION OF BULK PROPERTIES OF OPEN-CELL CARBON FOAM	79
7.1	MODELING OF CARBON FOAM	81

TABLE OF CONTENTS (Continued)

<u>Section</u>		<u>Page</u>
	7.1.1 Characterization of Geometry of Unit Cell of Carbon Foam	81
	7.1.2 Determination of Boundary Condition	87
7.2	NUMERICAL CALCULATION	88
	7.2.1 Prediction Method of Effective Bulk Moduli of Foam	88
	7.2.2 Results: Polyurethane Foam	94
	7.2.3 Results: Carbon Foam with Isotropic Properties	95
	7.2.4 Results: Carbon Foam with Anisotropic Properties	97
7.3	SUMMARY AND RECOMMENDATIONS	102
8	SCANNING ELECTRON MICROSCOPY INVESTIGATION OF DEFORMATION IN THE VICINITY OF A MODE II CRACK TIP IN UNIDIRECTIONAL TOUGHENED EPOXY COMPOSITES	104
	8.1 SPECIMEN PREPARATION	104
	8.2 EXPERIMENTAL PROCEDURE	105
	8.3 RESULTS AND DISCUSSION	105
	8.4 CONCLUSIONS	109
9	NONLOCAL MODELS OF STRESS FIELD CONCENTRATIONS AND EFFECTIVE THERMOELASTIC PROPERTIES OF RANDOM STRUCTURE COMPOSITES [48]	110
	9.1 THE GENERAL SCHEME	113
	9.2 NUMERICAL RESULTS	115
	9.3 CONCLUDING REMARKS	119
10	MICROMECHANICS OF NONLOCAL EFFECTS IN GRADED MATERIALS	122
	10.1 GENERAL SCHEME OF THE APPROACH PROPOSED	125
	10.2 PREVIOUS NUMERICAL RESULTS	125
11	QUANTITATIVE DESCRIPTION AND NUMERICAL SIMULATION OF RANDOM MICROSTRUCTURES OF COMPOSITES AND THEIR EFFECTIVE ELASTIC MODULI [59]	127
	11.1 STATISTICAL DESCRIPTION AND NUMERICAL SIMULATION OF RANDOM STRUCTURE COMPOSITES	130
	11.2 EFFECTIVE ELASTIC PROPERTIES	140
	11.3 SUMMARY AND RECOMMENDATIONS	141

TABLE OF CONTENTS (Concluded)

<u>Section</u>		<u>Page</u>
12	PUBLICATIONS AND PRESENTATIONS	144
	REFERENCES	147
	LIST OF ACRONYMS	152

LIST OF FIGURES

<u>Figure</u>		<u>Page</u>
1	Cruciform Specimen with Fiber Oriented at Angle θ to the Loading Direction	4
2	(a) Visual Observation of Interfacial Debonding in a 45-degree Off-Axis Specimen; (b) Magnified View of Illuminated White Region Shown in (a)	6
3	Variation of Interfacial Radial Stress Concentration Factor with Off-Axis Angle	8
4	Variation of Interfacial Shear Stress Concentration Factor with Off-Axis Angle	8
5	Failure Envelope for Off-Axis Cruciform Specimens	11
6	Composite Stress-Strain Curve for IM7/5250-4 Composite	16
7	Acoustic Emission Count as a Function of Load Level	16
8	Typical Fiber Breaks Observed During Tensile Loading of IM7/5250-4 Composite	16
9	Large Row of Fiber Breaks in a Single Plane Observed Close to Failure Load	17
10	Histogram of Measured Distance between Multiple Fiber Breaks	17
11	Matrix Cracks Bridged by Fibers	17
12	Interfacial Debonding Accompanied by Fiber Break	18
13	Measured Distribution of IM7 Fiber Tensile Strength	20
14	Shear Stress at the Interface	22
15	Fiber Axial Stress at the Interface	22
16	Radial Stress at the Interface	23
17	Matrix Axial Stress at the Interface	23
18	Microstructure of Woven Nextel 720/AS	27

LIST OF FIGURES (Continued)

<u>Figure</u>		<u>Page</u>
19	Magnified View of Microstructure Showing Matrix Cracks Due to Processing	27
20	Effective Thermoelastic Moduli of Woven Nextel 720/AS Composite as a Function of Transverse Crack Spacing	27
21	Overlapping Cubic B-Spline Functions with Seven Subdivisions	34
22	Unit Cell of a Plain-Weave Composite	36
23	Interfacial Normal and Shear Stress Distributions of a Unit Cell of a Plain-Weave Textile Composite	37
24	Dimensions and Geometry of One Quarter of a Cruciform Specimen	39
25	Normalized In-Plane Longitudinal and Out-of-Plane Shear Stress Concentration Factors Along the Middle of Transverse Fill Yarn in 1-D Model Laminate	40
26	Ratio of Stress Concentration Factors of Woven to those of Fillet with Various Dimensions of the Cruciform Specimen Geometry	41
27	Ratio of Stress Concentration Factors of Woven to those of Fillet with Various Yarn Waviness Ratio	43
28	Comparison of Measured and Modeled Cross-Section Profiles of Model Woven Composite	44
29	Axial Strain Comparison between B-SAM Predictions and Moiré Interferometry Measurements	45
30	Global and Local Coordinate Systems in Asymptotic Analysis	49
31	Laminated Composite Plate with a Slanted Edge	56
32	Overlapping Cubic B-Spline Functions with Seven Subdivisions	57
33	Mapping of Homogeneous Domain in x -Space to a Unit Cube in ξ -Domain	57
34	Distribution of Real and Imaginary Parts of the Roots with Various Slanted Angles	60

LIST OF FIGURES (Continued)

<u>Figure</u>		<u>Page</u>
35	Distribution of Magnitudes of Singular Stress Components with Two Roots for $\phi = 1^\circ$	62
36	Stress Distribution in Global xyz -Axes by Asymptotic and Numerical Analyses near Singular Point Along Straight Lines Parallel to the Interface between Two Plies	63
37	Stress Distribution in Local rst -Axes with $\psi = 1^\circ$ by Asymptotic and Numerical Analyses Along Contours of Constant Radii with the Center at the Singular Point	64
38	Distribution of Magnitudes of Singular Stress Components with a Complex Root, $\lambda_1 = 0.9646 + 0.0968 i$, for $\phi = 60^\circ$	67
39	Stress Distribution in Global xyz -Axes by Asymptotic and Numerical Analyses Near Singular Point Along Straight Lines Parallel to the Interface between Two Plies	68
40	Stress Distribution in Local rst -Axes with $\phi = 30^\circ$ by Asymptotic and Numerical Analyses Along Contours of Constant Radii with the Center at the Singular Point	69
41	Distribution of Magnitudes of Singular Stress Components with Two Roots for $\phi = 45^\circ$	70
42	Stress Distribution in Global xyz -Axes by Asymptotic and Numerical Analyses Near Singular Point Along Straight Lines Parallel to the Interface between Two Plies	71
43	Stress Distribution in Local rst -Axes with $\psi = 45^\circ$ by Asymptotic and Numerical Analyses Along Contours of Constant Radii with the Center at the Singular Point	72
44	Distribution of Magnitudes of Singular Stress Components with Two Roots for $\phi = 60^\circ$	74
45	Stress Distribution in Global xyz -Axes by Asymptotic and Numerical Analyses Near Singular Point Along Straight Lines Parallel to the Interface between Two Plies	75

LIST OF FIGURES (Continued)

<u>Figure</u>		<u>Page</u>
46	Stress Distribution in Local <i>rst</i> -Axes with $\phi = 60^\circ$ by Asymptotic and Numerical Analyses Along Contours of Constant Radii with the Center at the Singular Point	76
47	Microstructure of Carbon Foam	80
48	Points and Lines in a Cube and a Tetrahedron for Generating a Unit Cell of Carbon Foam	82
49	A Tetrahedron and Spheres to Generate a Unit Cell of Carbon Foam	83
50	Unit Cells of Carbon Foam with Various Porosities	83
51	One of Four Subtetrahedra Considering Symmetry in Figure 48	84
52	Cross-Sectional Slices During Bubble-Forming Process (R is the Radius of Spheres)	84
53	Intersection of a Subtetrahedron and Bubble Spheres ($\sqrt{2}a < R < \frac{2\sqrt{6}}{3}a$)	85
54	A Sub-subtetrahedron Discretized into Finite Volumes Along a Ligament Axis	86
55	3-D Mesh versus 1-D Beam Mesh of the Unit Cell of Carbon Foam	87
56	An Imaginary Tetrahedron inside which a Unit Cell of the Foam is Located	89
57	Relation between Bulk Density, Porosity and Bubble Size for Open-Cell Foams	90
58	Coordinate Systems for Rotating Unit Cell for Simulating Random Orientation	92
59	Variation of Young's Moduli of Unit Cells of Isotropic Foam on the Changes of Angles in Cartesian Coordinate Axes, with the First Rotation in the y -Axis and the Second Rotation in the z -Axis	92
60	Variation of Young's Moduli of Unit Cells of Isotropic Foam on the Changes of Angles in Cartesian Coordinate Axes, with the First Rotation in the z -Axis and the Second Rotation in the y -Axis	92

LIST OF FIGURES (Continued)

<u>Figure</u>		<u>Page</u>
61	Variation of Young's Moduli of Unit Cells of Isotropic Foam on the Change of Angles in Spherical Coordinate Axes	93
62	Prediction of Bulk Young's Moduli of Polyurethane Foam at Various Densities	95
63	Prediction of Bulk Poisson's Ratio of Polyurethane Foam at Various Densities	96
64	Prediction of Bulk Tensile Moduli of Carbon Foam at Various Densities	97
65	Prediction of Bulk Tensile Moduli of Carbon Foam at Various Densities with Several Assumed Ligament Properties of Carbon Material	98
66	Prediction of Bulk Poisson's Ratio of Carbon Foam at Various Densities	98
67	Prediction of Bulk Tensile Moduli of the Carbon Foam Predicted with Isotropic and Anisotropic Properties of Foam Ligaments	100
68	Prediction of Bulk Tensile Moduli of the Carbon Foam Predicted with Isotropic and Anisotropic Properties of Foam Ligaments	100
69	Variation of Bulk Tensile Moduli of the Carbon Foam with the Increase of Longitudinal Modulus of Foam Ligament	101
70	Prediction of Bulk Poisson's Ratio of the Carbon Foam Predicted with Isotropic and Anisotropic Properties of Foam Ligaments	101
71	Prediction of Bulk Poisson's Ratio of the Carbon Foam Predicted with Isotropic and Anisotropic Properties of Foam Ligaments	102
72	SEM Image of the Mode II Crack Tip Region at Two Consecutive Load Levels	106
73	SEM Image of the Mode II Crack Tip Region in the Resin-Rich Region of the Sandwich Specimen	107
74	Fully Extended Interlaminar Crack at (a) 186-lb Loading and (b) 226-lb Loading	108
75	Compression Fiber Failure on Inner Surface of the Bottom Face Sheet at 226-lb Load	109

LIST OF FIGURES (Continued)

<u>Figure</u>		<u>Page</u>
76	Variation of the Effective Shear Modulus μ^* as a Function of a Concentration of the Inclusions c	116
77	The Functions and their First Derivatives versus Argument x_1 : $f_2(x_1)$ (solid line), $f_1(x_1)$ (dot-dashed line), $f_1'(x_1)$ (dotted line)	118
78	The First Few Iterations of Statistical Averages $\langle \sigma_{11} \rangle_I(x_1)$ versus x_1 Estimated for the Functions $f_2(x_1)$ and Nonstop $g(r)$ by the MEFM	119
79	Variation of the Effective Modulus L_{2222}^* as a Function of a Coordinate x_2 Estimated by: MEFM and Nonstep Function $g(r)$ (dashed line), MEFM and Step Function $g(r)$ (dot-dashed line), Mori-Tanaka and Nonstep $g(r)$ (dotted line), Mori-Tanaka and Step Function $g(r)$ (dotted line)	126
80	Variation of Statistical Average Stresses Inside the Inclusions $\langle \sigma_{22} \rangle_I(x_2)$ (solid line) and $\langle \sigma_{12} \rangle_I(x_2)$ (dot-dashed line) for the External Loading at the Infinity $\sigma_{ij}^\infty = \delta_{2j}\delta_{ij}$ and $\sigma_{ij}^\infty = \delta_{11}\delta_{ij}$, respectively, and a Step Function g	126
81	The Radial Distribution Functions $g(r)$ versus Relative Radius r/a Estimated by the HCM at $c=0.55$ (solid line) and $c=0.5$ (dotted line), and by HCSM at $c=0.55$ (dot-dashed line) and $c=0.5$ (dashed line)	133
82	Histogram of Fractions $p(n_i)$ of Testing Window Containing n_i Inclusions Generated by the HCM (solid curve) and by the HCSM (dotted curve)	134
83	Length of Monte Carlo Simulation N^{MC}/N versus an Area Fraction c Appropriate to the HCM (solid curve) and to the HCSM (dotted curve)	135
84	The Radial Distribution Functions $g(r)$ versus Relative Radius r/a Estimated by the IPSM at $c=0.65$, $N=3700$: 150 Shaking (solid curve), 100 Shaking (dashed curve), 30 Shaking (dot-dashed curve), 10 Shaking (dotted curve)	136
85	The Radial Distribution Functions $g(r)$ versus Relative Radius r/a : Single Sample 546-0181 (dashed curve), Averaged Over 10 Samples of 546-0161 (dotted curve), at $c=0.65$, Averaged Over 10 Samples of 546-0181 (dot-dashed curve), Averaged Over Eight Materials Produced by the Different Technological Regime (solid curve)	137

LIST OF FIGURES (Concluded)

<u>Figure</u>		<u>Page</u>
86	Radial Distribution Functions $g(r)$ versus Relative Radius r/a Estimated by the Modified CRM at $c=0.60$ (dashed curve), $c=0.65$ (dot-dashed curve), $c=0.70$ (dotted curve), $c=0.75$ (solid curve)	138
87	Radial Distribution Functions $g(r)$ versus Relative Radius r/a Estimated by the Modified CRM at $N=811$ and $c=0.90$ (solid curve), $c=0.85$ (dotted curve), $c=0.80$ (dot-dashed curve), $c=0.75$ (dashed curve)	138
88	Radial Distribution Functions $g(r)$ versus Relative Radius r/a Estimated by the Numerical Simulation (solid curve), from Experimental Data (dotted curve), by the Analytical Approximation [54] (dot-dashed curve)	139
89	Variation of the Effective Shear Modulus μ^* as a Function of a Concentration of the Inclusions c	140
90	Variation of the Relative Effective Shear Modulus $\mu^*/\mu^{(0)}$ as a Function of a Concentration of the Inclusions c Estimated by the MEFM with $g(r)$ [54] (dot-dashed line), by the MEFM with the RDF Simulated by the Modified CRM (solid curve), by the MEFM with Well Steered $g(r)$ (dashed curve), and by the MEFM with Experimentally Estimated RDF o	141

LIST OF TABLES

<u>Table</u>		<u>Page</u>
1	Elastic Properties of Constituents	6
2	Applied Stress at Debonding and Maximum Stress Concentration Factors as a Function of Off-Axis Angle	10
3	Material Properties Used in Analysis	19
4	Stresses in Undamaged IM7/5250-4 Composite, $\Delta T = -205^{\circ}\text{C}$, $\sigma_c = 0$	20
5	Stresses in Undamaged IM7/5250-4 Composite, $\Delta T = 0$, $\sigma_c = 1$	20
6	Comparison of Experiments with Predictions Simulating Various Failure Modes	29
7	Material Properties of AS4/3501-6	59
8	Predicted Effective Young's Moduli and Poisson's Ratio of an Isotropic Foam	94

FOREWORD

This report was prepared by the University of Dayton Research Institute under Air Force Contract No. F33615-00-D-5006, Delivery Order No. 0002. The work was administered under the direction of the Nonmetallic Materials Division, Materials and Manufacturing Directorate, Air Force Research Laboratory, Air Force Materiel Command, with Karla L. Strong (AFRL/MLBCO) as Project Engineer.

This report was submitted in March 2002 and covers work conducted from 30 November 2000 through 29 November 2001.

EXECUTIVE SUMMARY

The cruciform specimen design was modified to characterize the fiber-matrix interface under combined transverse and shear loading, which allowed a mixed-mode failure envelope to be constructed. The micromechanical failure modes in a unidirectional IM7/5250-4 composite under tensile loading parallel to the fibers to identify initiation and growth of microdamage were analyzed using the axisymmetric damage model (ADM) of a concentric cylinder. The effective thermoelastic moduli of a damaged multiphase woven oxide-oxide composite was computed and compared to experiment. It was shown that additional damage mechanisms, such as fiber-matrix interfacial debonding, delamination or effective matrix degradation, could lead to lower estimates of the Young's modulus in the thickness direction. The fiber pushout test was described using solutions to several boundary value problems using two numerical methods, namely ADM and finite element method (FEM). The study illustrated the complexity of micromechanical stress fields at the fiber-matrix interface and proposed some guidelines to examine in these key boundary value problems.

A B-spline analysis method (B-SAM) with overlapping B-spline approximation functions of displacements along with a curvilinear transformation was developed and successfully applied to a three-dimensional analysis of a woven textile composite including incorporation of cruciform unit-cell specimens. The optimum cruciform geometric configuration to generate failure in the gage section was determined parametrically and confirmed by Moiré interferometry.

Accurate stress fields of laminated composites with slanted free edges near ply interfaces were calculated for various slanted angles based on the B-SAM. The behavior of the power of

singularity was highly dependent on the slanted angles of the free edge with excellent agreement with the two-term singular asymptotic solution.

Carbon foam was modeled with three-dimensional microstructures to develop a basic understanding of the performance of open-cell foam materials. The microstructural properties were then correlated with the bulk properties through this model, which should provide a basis for establishing a process-property relationship and optimizing foam properties. The predictions indicated that the effective bulk moduli of the carbon foam were dependent more on the transverse modulus of the foam ligaments than on the longitudinal one, while the Poisson's ratio was dependent on both the longitudinal and transverse moduli.

Mode II cracks were observed *in situ* using a high resolution Philips XL30 E-SEM. Interlaminar crack tip features were examined in unidirectional fiber-reinforced composites with and without the resin-rich areas at the midsurface of the laminate and face sheet failure in sandwich plates. Further work is required in order to investigate the Mode II crack extension mechanism in resin-rich regions.

Nonlocal models of stress field concentrations were developed to examine the effective elastic properties of random structures in composites (i.e., fibers within bundles). The iteration method and the Fourier transform method were both examined, each with its own series of advantages and disadvantages. The obtained relations depend on the values associated with the mean distance between inclusions, and do not depend on the other characteristic size. The iteration method was found to be superior to the Fourier transform method in all cases except when an analytically explicit relation is required.

The models above were applied to functionally graded materials, which are statistically inhomogeneous. The use of small clusters of homogeneous materials allowed an analysis of

these statistically inhomogeneous materials. This can be considered similar to the analysis of imbedded polymer crystals in an amorphous mass or the percolation of chains in a polymer.

As part of the above modeling, the random organization of fibers within bundles in composites was examined. The particle reorganization induced in a computer simulation by shaking is subjected only to geometrical constraints, whereas for real structures the packing is far more complicated. Our simulation technique is able to isolate the fundamental geometrical constraints from other physics-mechanical and chemical effects, and the results provide a valuable benchmark for evaluating sophisticated packing schemes used to model real composite materials. While taking a single point probability density (volume fraction) into account can provide a rough estimation of bounds of effective properties, more informative characteristics of the point set are obtained using statistical second-order quantities (such as two-point probability density, second-order intensity function, radial distribution function, and nearest neighbor distribution), which examine the association of a point relative to other points.

1. MIXED-MODE FAILURE CRITERIA USING CRUCIFORM GEOMETRY

The single-fiber cruciform design was successful in eliminating the influence of free-edge stresses, which were present in transverse testing of conventional straight-sided specimens. In this work, the cruciform specimen design was modified [1] to characterize the fiber-matrix interface under a combined state of transverse and shear stresses. This was achieved by utilizing a cruciform specimen in which the wings of the cruciform specimen were not perpendicular to the loading direction. Instead, the ratio of the normal to shear loading was governed by the amount of angle the fiber (oriented along Z') made with the loading direction (X -axis), as seen in Figure 1. Note that this figure is a schematic of the cross section passing through the midplane in the thickness direction of the off-axis cruciform test geometry. The fiber extends across the full width ($2l$) of the sample and is centered with respect to specimen thickness (t). The angle θ between the fiber axis and the loading direction is referred to as the off-axis angle.

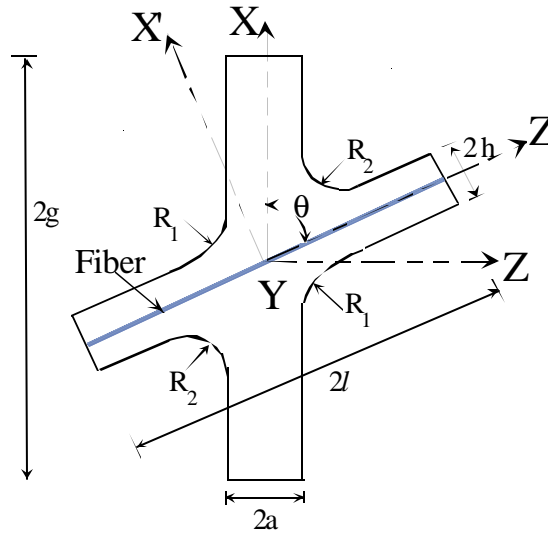


Figure 1. Cruciform Specimen with Fiber Oriented at Angle θ to the Loading Direction

In this study five off-axis angles, namely 15, 30, 45, 60 and 75 degrees, were investigated in a model system consisting of 140- μm -diameter silicon carbide (SCS-0) fiber in Epon 828

epoxy. The epoxy resin (from Shell Chemical Co.) was cured with a polyetheramine (Jeffamine D-230 from Texaco, Inc.) for 14 days at ambient temperature. Curing at ambient temperature¹ eliminated thermal residual stresses, which were otherwise induced from the mismatch in coefficients of thermal expansion of fiber and matrix, and were therefore not considered in this work. Model single-fiber off-axis cruciform samples were made using standard fiberglass epoxy end tabs with the following specifications: wing height (2h) equals 5.08 mm, loading arm width (2a) equals 7.62 mm, sample width (2l) equals 38.1 mm, grip-to-grip distance (2g) equals 50.8 mm, and fillet radii of curvature, R_1 and R_2 , equal 7.62 mm and 2.54 mm, respectively.

Initiation and growth of interface debonds were detected optically by observation of variations in the intensity of light reflected from the surface of the fiber during loading. The reflected light technique [3] has been extensively utilized to detect debonding in textile-sized fibers, such as 15- μ m-diameter Nicalon fiber, and 7- μ m-diameter AS4 graphite fiber. During the test, illumination was set at an intensity such that before loading, the fiber surface was on the verge of being shiny. This lighting produced a bright area along the approximate centerline of the fiber that was present throughout the test. The reflective centerline area is not to be confused with the debond. For this work we concentrated our efforts on measuring the stress level at which debonding initiates in off-axis cruciform specimens. The magnification was adjusted to a level great enough to allow the debond length to be determined accurately while being low enough to maintain the maximum field of view. The tradeoff between field of view and magnification was necessary for the best opportunity of capturing the initiation of debonding, since the entire gage length could not be imaged at once.

¹ Chemical shrinkage in room temperature-cured epoxies could be significant [2]. However, shrinkage-induced strains were neglected in this study since no data was available for Epon 828 cured with polyetheramine. Current effort is underway to estimate these quantities and will be reported elsewhere.

Figure 2a is a photomicrograph of a cruciform specimen with the fiber oriented at 45 degrees with respect to the loading direction. Note the white line in the central region of the cruciform sample in the gage area. This picture was taken with the sample illuminated by a light source, and the white line that we are seeing in this image is the light, which is reflected, by the debonded fiber-matrix interface. Figure 2b is a magnified view of the central region of the sample and clearly shows the illuminated white area corresponding to the debonded interface. These micrographs in Figure 2 are therefore a visual confirmation of fiber-matrix debonding that took place in a cruciform specimen, and the length of the reflective (white) region is an approximate measurement of the extent of debonding.

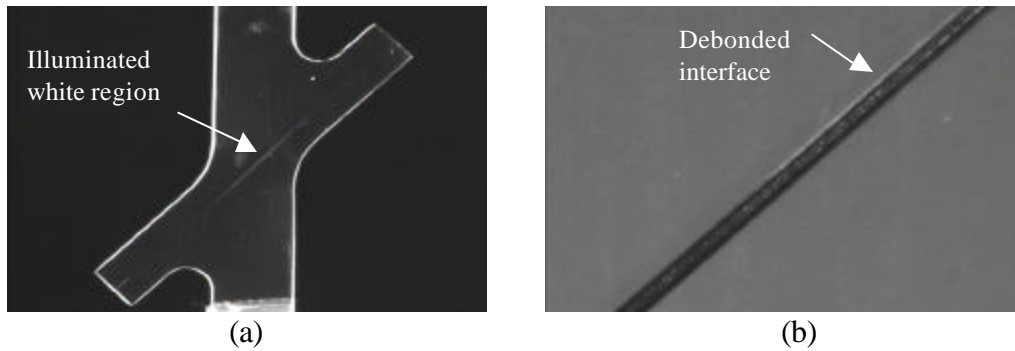


Figure 2. (a) Visual Observation of Interfacial Debonding in a 45-degree Off-Axis Specimen; (b) Magnified View of Illuminated White Region Shown in (a).

The single-fiber off-axis cruciform specimen was analyzed using 3-D FEA employing the ABAQUS code [4]. The SiC reinforcement and epoxy matrix were modeled with 3-D eight-node brick elements with the elastic properties listed in Table 1.

**Table 1
Elastic Properties of Constituents**

Constituents	E, GPa	n
SCS-0	400.0	0.15
Epoxy	3.44	0.35

The fiber-matrix interface was assumed to be perfectly bonded, since we wanted to evaluate the stress distribution in the sample prior to damage. Due to the large number of degrees of freedom that were anticipated (because of 3-D modeling), meshes were generated such that computational efficiency would be maintained without sacrificing accuracy. Finer subdivisions were employed in the regions where the stress gradient was expected to be high, such as along the fiber-matrix interface and in the fillet regions. The finite element (FE) model was loaded by applying tension along the X-axis (as shown in Figure 1) by means of constant displacement of the end nodes to simulate clamped-end conditions.

The variations of radial ($\sigma_{x'x'}$) and shear ($\sigma_{x'z'}$) stresses at the fiber-matrix interface along the fiber length are shown in Figures 3 and 4, respectively, as a function of off-axis angle, θ . These stresses were evaluated in the X'-Z' plane located at Y=0 (i.e., through the x-section passing through the midplane in the thickness direction). For parametric analysis, the smaller radius of curvature, R_2 , was additionally reduced to 1.524 mm for a 30-degree specimen and to 0.318 mm for a 15-degree specimen. This reduction was done in order to maintain a circular fillet, with a 150-degree rotation for the 30-degree off-axis specimen and a 165-degree rotation for the 15-degree off-axis specimen.

As expected, the radial stress concentration factor was the largest for the 90-degree specimen, and the magnitude decreased as the off-axis angle θ was reduced. On the other hand, the shear stress at the interface was maximum for a 45-degree off-axis specimen, as seen in Figure 4. With smaller values of the off-axis angle, it was observed that the peak in the shear stress distribution became broader and flattened out. Thus, even though the maximum shear stress was reduced as the off-axis angle was lowered below 45 degrees, significant values of shear stresses now occurred over larger fiber lengths in the central region of the cruciform

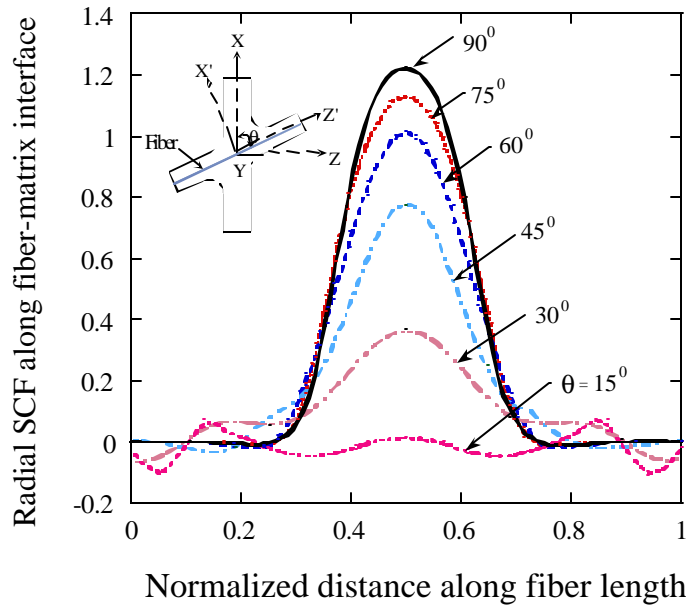


Figure 3. Variation of Interfacial Radial Stress Concentration Factor with Off-Axis Angle.

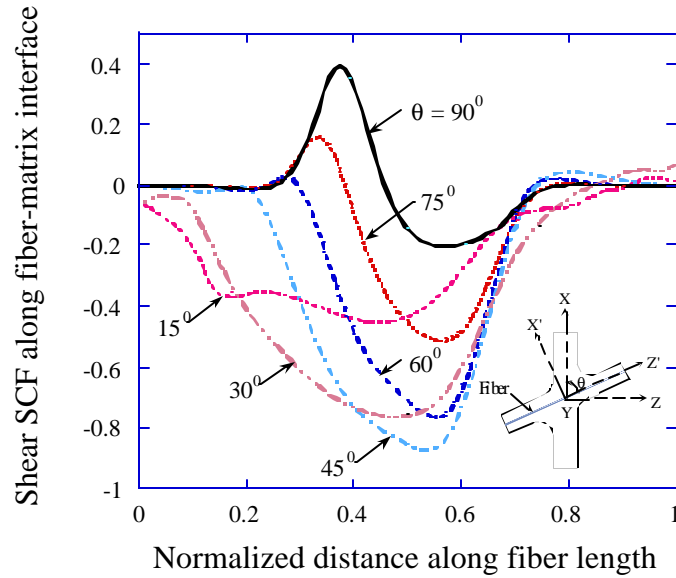


Figure 4. Variation of Interfacial Shear Stress Concentration Factor with Off-Axis Angle.

specimen. Also, the location of the maximum shear stress changed with the cruciform geometry and did not necessarily occur at the same location where the interfacial radial stress was a maximum. Moreover, because of unequal values of radii of curvature ($R_1 = 7.62$ mm and

$R_2 = 2.54$ mm), the shear stress was no longer antisymmetric (the two shear stress peaks had different width and amplitude) about the loading axis and was not zero at the specimen center.

A minimum of eight samples were considered for each one of the three off-axis angles considered, namely, 30, 45 and 60 degrees. Table 2 lists the average value (over all specimens) of externally applied stress at debond initiation measured for the specimens tested along with the maximum radial and shear stress concentration factors evaluated at the fiber-matrix interface as a function of off-axis angle. As a first approximation, the maximum stress criteria [5] could be employed to predict failure initiation in the off-axis cruciform specimens, since we had demonstrated that debonding initiated in the interior region of the specimen, which was free of initial stress singularities. Both the initiation and growth criteria, however, could depend on interaction between interfacial shear and normal stresses and their respective modes of energy release rates. Instead of utilizing both the maximum radial and shear stress concentration factors, we also considered the following two alternate options: (i) use the maximum radial stress concentration factor and the shear stress concentration at the location of maximum radial stress, or (ii) use the maximum shear stress concentration factor and the radial stress concentration at the location of maximum shear stress. In either of these two cases, we did not obtain significant differences (less than five percent) in the stress concentration values compared to the present approach. There was yet one more option possible and that was to use the radial and shear stress concentration factors at the location of debond initiation. However, precise measurement of the failure initiation site was not made for the specimens tested. Thus, in the absence of the exact location, the maximum values of stress concentration factors served as useful approximations.

Table 2
Applied Stress at Debonding and Maximum Stress Concentration Factors
as a Function of Off-Axis Angle

Off-Axis Angle (°)	Applied Stress at Debonding (MPa)	Standard Deviation (MPa)	Maximum Radial Stress Concentration Factor	Maximum Shear Stress Concentration Factor
30	41.37	6.49	0.3825	0.7413
45	32.3	3.40	0.7741	0.8529
60	31.7	5.03	0.9938	0.7402
90	33.4	2.3	1.267	0

The data for the 90-degree transverse specimen listed in Table 2 were taken from our earlier work [3]. For that 90-degree geometry (with equal values of fillet radii of curvature), microscopic examination of the fracture surface had revealed [6] a smooth fiber surface which was indicative of failure occurring due to normal stress alone. Further, the radial stress was maximum in the loading direction at the specimen center, while the shear stress was zero at that location. Those stress concentration values were therefore entered in Table 2 for the 90-degree specimen. In contrast, none of the off-axis cruciform samples tested in this study (30-, 45- and 60-degree specimens) failed along the fiber length. The average applied stresses at debond initiation for different off-axis angles were multiplied with their corresponding stress concentration factors and the results plotted in the normal-shear stress space, as shown in Figure 5.

A quadratic failure envelope given by

$$s^2 + c_1 t^2 = c_2 \quad (1)$$

fit the experimental data rather reasonably well. The constants c_1 and c_2 were evaluated using the measured value of interfacial normal strength and the 45-degree off-axis cruciform data. The constant c_1 was estimated as 1.5, while the shear strength of the interface was extrapolated as 34.5 MPa. The empirical curve given by Equation (1) was found to be a good fit to the

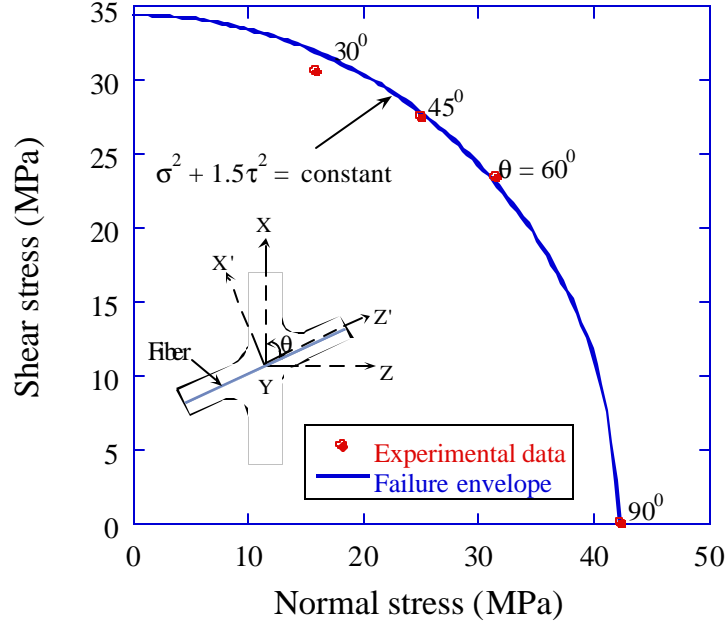


Figure 5. Failure Envelope for Off-Axis Cruciform Specimens.

remainder of the off-axis data (i.e., 30- and 60-degree measurements). Note that for this part of the study we had neglected the cure shrinkage-induced stresses since no data were available for Epon 828 cured with polyetheramine. Current effort is underway to estimate these quantities, and when properly accounted for, it would result in a horizontal shifting of the failure envelope to the left. Nevertheless, the proposed off-axis specimen design promises to be an elegant method for extrapolating the shear strength of the fiber-matrix interface, although an independent assessment of the shear strength would be a valuable test of the proposed failure criteria. Other test methods, such as torsional loading of a shear analog to the cruciform-shaped specimen, or torsional loading of a rectangular composite [7], are currently being explored to evaluate the shear strength of the fiber-matrix interface, which will be subsequently compared with the estimated value.

1.1 SUMMARY AND RECOMMENDATIONS

The results of the present investigation were highly encouraging, since a simple polynomial fit to the data from two different angles was seen to predict the measurements at other off-axis angles. The scatter in the data was relatively small, while the analytical model remained quick and efficient to run, similar to the 90-degree cruciform geometry developed earlier. Failure initiation took place in the interior region of the specimen, which was free of initial stress singularities. Thus, the evaluated strength values were not influenced by the free-edge effects which seem to dominate some of the more common test methods, such as slice compression, microindentation, pushout and fragmentation, used to characterize the shear strength of the fiber-matrix interface.

2. DAMAGE EVOLUTION AND FAILURE MODELING IN UNIDIRECTIONAL GRAPHITE/BMI COMPOSITE

In this study an integrated experimental and analytical approach was initiated to examine and predict the micromechanical failure modes in a unidirectional composite when subjected to tensile loading parallel to the fibers. Understanding and modeling of failure in advanced composite materials involves several different and interactive failure modes within the constituents of each ply and between plies of a composite laminate. This in turn results in a need for accurate modeling of the stress distribution within the plies and its constituents at the micromechanical scale. An investigation of the initiation and propagation of damage, such as an interfacial debond or a matrix crack, must be based on appropriate failure criteria. Clearly both the initiation and growth criteria may depend on interaction between shear and normal stresses and their respective modes of energy release. Numerous failure scenarios are therefore possible given the right conditions, i.e., particular combinations of relative properties of the constituents, ultimate strengths and critical energy release rates. Our objective was to base failure on fundamental properties of the constituent materials, such as fiber, matrix, and interface. This approach will provide the basis for developing a fundamental understanding of the failure mechanisms that will lead to appropriate failure criteria for a unidirectional ply with a minimum number of tests.

In this work we have provided direct and indirect evidence of the existence of a number of basic modes of initial damage. Unfortunately, it was not possible to observe directly the development and growth of damage, especially that which existed in the interior of a sample. Rather, surface observations were taken intermittently throughout the loading history, and optical and scanning electron microscopy was performed on the failure surface. This provided a fairly

comprehensive picture of the failure events that had taken place but left unanswered questions regarding the sequence of these events. These questions were then addressed by the micromechanics models [8,9] to postulate logical failure scenarios.

The material system was carbon fiber-reinforced, toughened bismaleimide, IM7/5250-4. This system exhibits characteristics ideal for a generic study of this nature; it is well characterized and exhibits consistent properties. A unidirectional panel was laid up from the unidirectional prepreg and was cured in an autoclave in accordance with the manufacturer's recommended cure cycle. Nonperforated Teflon bleeder plies were used to make smooth finished surfaces of the specimen. The cured composite panel was postcured for six hours at 230°C in an oven. Rectangular coupons were cut from the panels using a diamond-impregnated saw blade. Specimens were 12.5 mm wide with a gage length of 150 mm. One of the specimen surfaces was polished using 2-micron and 0.5-micron polishing powder to enhance the microscopic image for microdamage detection. Prior to testing, the polished specimen surface was examined under a microscope. No damage was observed in any as-processed specimen. All specimens were then stored in a desiccated cabinet until testing. Fiberglass/epoxy end-tabs were bonded to the specimens prior to testing, which was done at room temperature.

All specimens were loaded in tension at a strain rate of 0.02/min. These specimens were subjected to initial loading ranging from 60 percent to 95 percent of the ultimate strength and unloaded for microscopic examination. Acoustic emission (AE) was monitored in all tests to determine onset of damage and subsequent failure processes in the specimen during loading. Photomicrographs with 400 to 600 magnification were taken randomly in the central region (~10 mm long) of the polished surface to record damage such as fiber breakage, matrix microcracking and fiber/matrix debonding. It was assumed that these observations were representative of

damage accumulation over the length of the specimen, since it was physically not possible to examine the entire surface. This will be verified subsequently by making random observations of damage accumulation in other regions at a later time.

Figures 6 and 7 show a typical stress-strain curve and AE count, respectively, for an IM7/5250-4 unidirectional composite. For this specimen the first significant AE event occurred at 9.34 kN, probably resulting from onset of damage. However, upon unloading, no visible damage was detected under the optical microscope. It is possible that microcracks may have closed upon unloading, and we were therefore unable to observe them. Future effort will be directed to examine initiation of microdamage under *in situ* loading. Further increase of AE activity with applied load is indicative of additional damage accumulation.

Figures 8, 9, 11 and 12 show photomicrographs of various damage mechanisms observed during loading. These photomicrographs were taken from a specimen that was loaded to a composite stress of 2380 MPa (failure stress was 2586 MPa). Numerous fiber breaks were observed, as shown in Figures 8 and 9. While some of the fiber breaks were isolated, as shown in Figure 8, there was clearly a large row of fiber breaks lying along a single plane, as shown in Figure 9. This latter feature was mostly observed close to final failure of the unidirectional specimen. In addition, multiple breaks of some fibers were also observed, as shown in Figure 8. This suggests that stress transfer had taken place in some regions such that high value of the redistributed fiber axial stress had developed. Figure 10 is a histogram of measured distances between multiple fiber breaks. While there was certainly some scatter in the measured values, the average distance between multiple breaks of individual fibers was approximately 75 microns (average of 130 fiber break distances).

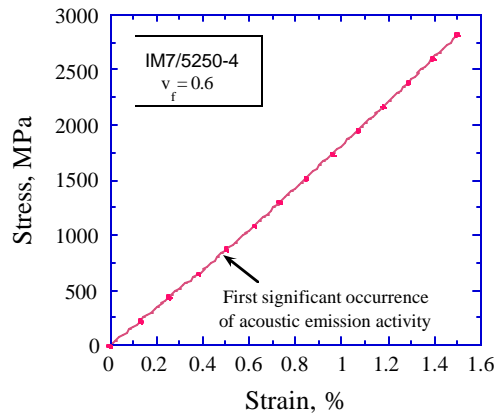


Figure 6. Composite Stress-Strain Curve for IM7/5250-4 Composite.

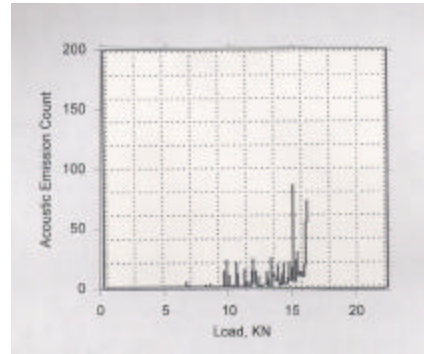


Figure 7. Acoustic Emission Count as a Function of Load Level.

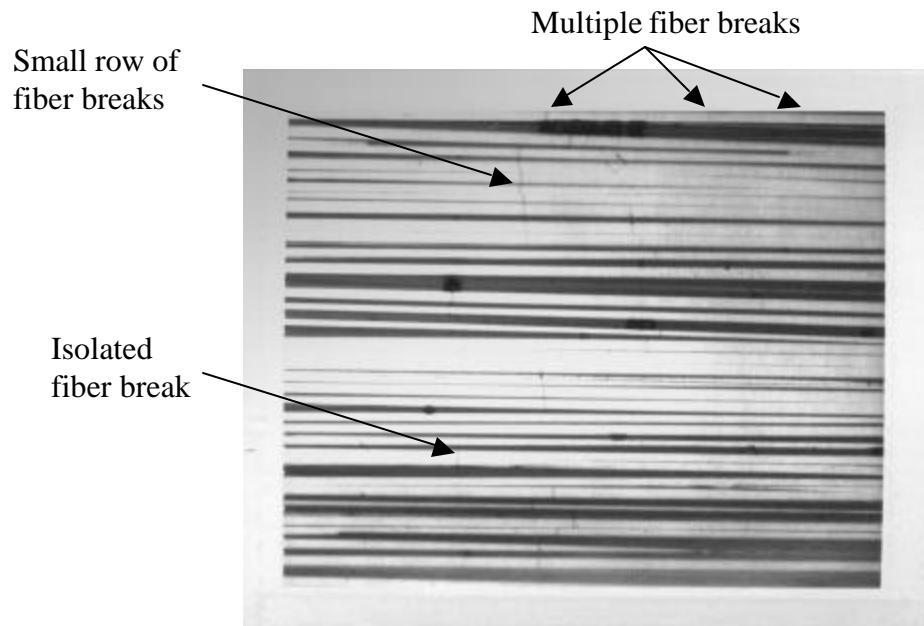


Figure 8. Typical Fiber Breaks Observed During Tensile Loading of IM7/5250-4 Composite.

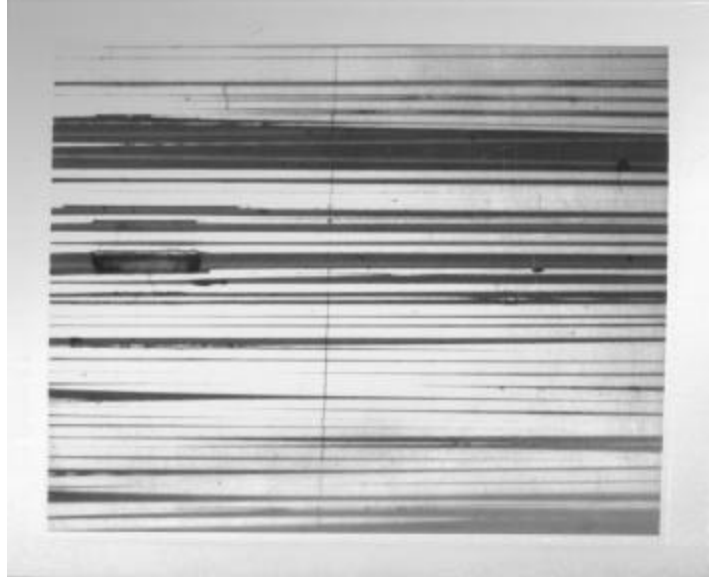


Figure 9. Large Row of Fiber Breaks in a Single Plane Observed Close to Failure Load.

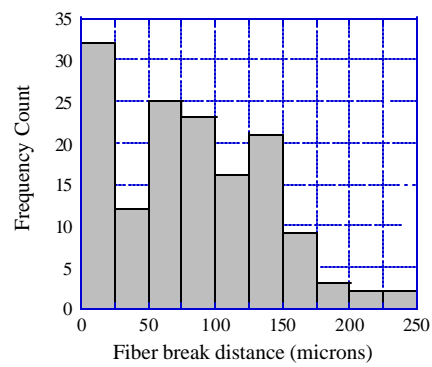


Figure 10. Histogram of Measured Distance between Multiple Fiber Breaks.

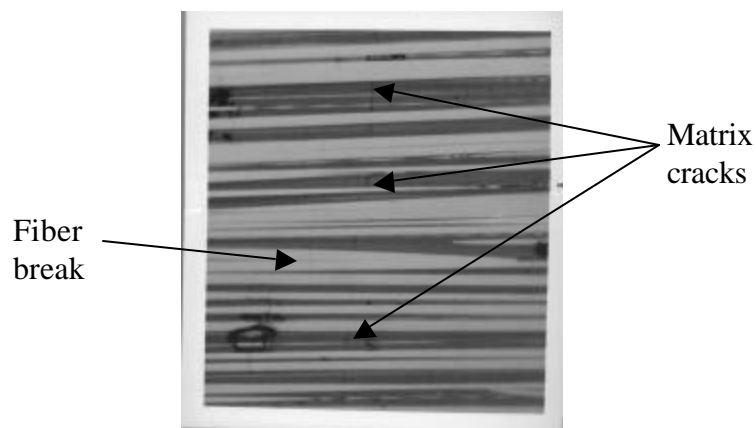


Figure 11. Matrix Cracks Bridged by Fibers.

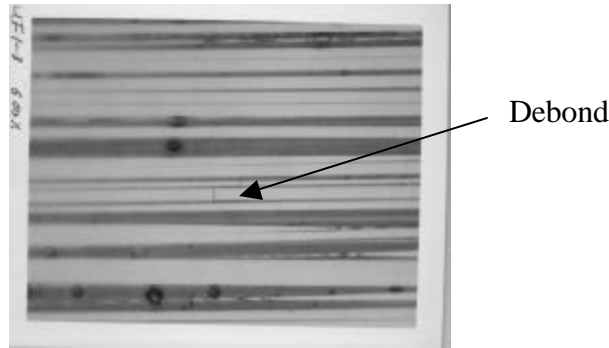


Figure 12. Interfacial Debonding Accompanied by Fiber Break.

In addition to fiber breaks, we also observed matrix cracks normal to and bridging the fibers, as shown in Figure 11. In some cases it was seen that the matrix cracks occurred in a single plane, which was different from the plane in which fibers broke. The matrix cracks were rather widely distributed. Finally, we also observed debonding of the fiber-matrix interface in conjunction with fiber break, as shown in Figure 12. However, not all broken fibers had a debonded interface at the broken fiber end. From the photomicrographs, an average value of debond length was measured as 24 microns.

The information obtained from the photomicrographs just described, however valuable, was incomplete since we did not know the applied stress levels at which the various events took place. Table 3 lists the thermoelastic properties of IM7 fiber and 5250-4 matrix, where E , ν , G and α represent Young's modulus, Poisson's ratio, shear modulus, and coefficient of thermal expansion, respectively, while the subscripts T and A on the material properties denote the directions transverse and parallel to the fiber axis, respectively. The properties of the matrix were measured in the laboratory. The fiber axial Young's modulus was taken from the Hercules data sheet [10], while the remainder of the properties were back-calculated using NDSANDS [11]

Table 3
Material Properties Used in Analysis

Property	Material	
	IM7 Fiber	5250-4 Matrix
E_T (GPa)	19.5	4.28
E_A (GPa)	276	4.28
ν_T	0.7	0.36
ν_A	0.28	0.36
G_A (GPa)	70	1.57
$\alpha_T (10^{-6}/^\circ\text{C})$	3.8	46.8
$\alpha_A (10^{-6}/^\circ\text{C})$	-0.05	46.8
Ultimate strength (MPa)	4224	77
Fracture toughness ($\text{MPa m}^{1/2}$)	-	0.88

in conjunction with the measured unidirectional ply properties (fiber volume fraction equals 0.6 and fiber diameter is 4.5 microns). The fiber tensile strength was also measured, as shown in the histogram in Figure 13, with an average value of 4.05 GPa. Our intention was to apply the micromechanics models [8,9,11], using the input data in Table 3, to deduce what we could about the initiation of damage and to postulate reasonable failure properties, wherever necessary, to carry out the analysis of subsequent failure sequences.

To determine the damage initiation event, we calculated the stresses in fiber and matrix corresponding to the composite stress at which the first significant AE activity took place. Tables 4 and 5 list the computed stresses, using the generalized plain strain model [11], under a thermoelastic cooldown and uniaxial tension, respectively. Of the five specimens tested, the first occurrence of significant AE activity took place at an average composite stress of 812 MPa. At this composite stress value, the fiber and matrix axial stresses were calculated as 1303 MPa and 76 MPa, respectively (including residual stresses). Note that the major contribution to the matrix axial stress came from the residual stress problem.

It was now possible to conceive of two different scenarios of damage initiation. In the first case, comparing the matrix stress (76 MPa) with its strength value (77 MPa), it was very

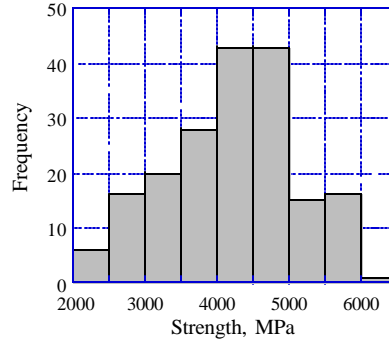


Figure 13. Measured Distribution of IM7 Fiber Tensile Strength.

Table 4
Stresses in Undamaged IM7/5250-4 Composite,
DT = -205°C, $s_c = 0$

	Radius, mm	s_z , MPa	s_q , MPa	s_r , MPa
Fiber	0	-36.5	-13.0	-13.0
	2.25	-36.5	-13.0	-13.0
Matrix	2.25	54.6	52.0	-13.0
	2.905	54.6	39.0	0

Table 5
Stresses in Undamaged IM7/5250-4 Composite,
DT = 0, $s_c = 1$

	Radius, mm	s_z , MPa	s_q , MPa	s_r , MPa
Fiber	0	1.65	-0.000507	-0.000507
	2.25	1.65	-0.000507	-0.000507
Matrix	2.25	.0261	0.00203	-0.000507
	2.905	.0261	0.00152	0

likely that matrix microcracking would take place at or close to the corresponding composite stress level. The full-cell crack model of Pagano and Brown [12] was used to simulate an annular matrix crack initiating at the midpoint between fibers. As the crack grew, the tip of the matrix crack advanced toward the fiber-matrix interface. We found that the potential energy release rate at the matrix crack tip attained a peak value as the crack tip approached the interface.

However, the model predicted that there was insufficient driving force to mobilize the crack, since the calculated peak value (1.1 J/m^2) was much less than the critical value, G_{Ic} (157.5 J/m^2).

The latter value was determined via the relation

$$G_{Ic} = K_{Ic}^2 \frac{1 - \nu_m^2}{E_m}, \quad (2)$$

where K_{Ic} was the fracture toughness of the matrix material. Consequently, additional damage had to occur before the matrix crack became unstable.

We also examined the fiber and matrix stresses at the interface as the matrix crack approached the interface. For these calculations, the fiber radius was $2.25 \text{ }\mu\text{m}$, while the outer matrix radius was set at $2.905 \text{ }\mu\text{m}$ in order to obtain 60 percent fiber volume fraction. The tip of the matrix crack was successively placed at a radius of 2.7, 2.5875, 2.43, 2.3175 and 2.25 microns, to simulate an advancing matrix crack. It was found that the radial stress at the interface remained largely compressive away from the matrix crack plane, while the shear stress value exhibited a peak in its behavior, as shown in Figure 14. The axial stress in the fiber was also found to increase in magnitude in a region near the matrix crack plane as the matrix crack approached the interface, as seen in Figure 15. It is to be noted that the large ADM stress values at the crack tip were merely approximations of elastic singularities. Away from the plane of the matrix crack, the fiber axial stress recovered its far-field value. Thus, secondary damages in the form of either shear debonding of the interface or fiber breakage in the plane of the matrix microcrack, were possible with matrix microcracking as the initiating damage event. In the second scenario we compared the fiber axial stress (1303 MPa) at the first occurrence of a significant AE event to its average ultimate strength (4224 MPa). The use of maximum stress as a failure criterion implied no fiber breakage at the composite stress level (812 MPa), even though

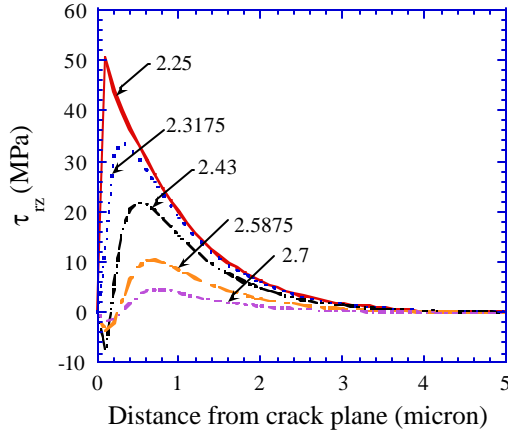


Figure 14. Shear Stress at the Interface.

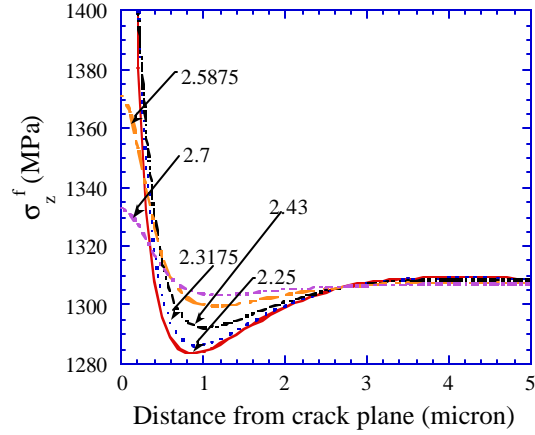


Figure 15. Fiber Axial Stress at the Interface.

there was considerable scatter (standard deviation equals 894 MPa) in the measured strength values. However, when the composite stress was increased to 1300 MPa, the fiber axial stress increased to 2110 MPa, which was well within the scatter band of fiber failure. Thus, it was very likely that fiber failure would take place at the higher composite stress value.

Next, we assumed that fiber cracking was a damage initiation event and put a penny-shaped crack in the fiber in the analytical model [8]. Similar to the matrix microcracking problem, we observed the variation of stresses at the fiber-matrix interface as the penny-shaped fiber crack grew from a radius of 1.35 μm to 2.25 μm . As shown in Figure 16, it was found that the interfacial radial stress near the fiber break plane was tensile and increased in magnitude as the crack advanced toward the fiber-matrix interface. The other significant stress component was the axial stress in the matrix, which was also tensile and increased considerably with crack growth, as seen in Figure 17. Thus, secondary damages in the form of either tensile debonding of the interface or matrix microcracking, were possible with fiber cracking as the initiating damage event. The potential energy release rate at the crack tip was also calculated. However, the calculated values could not be compared to the critical energy release rate since no fracture toughness information was available for IM7 fiber.

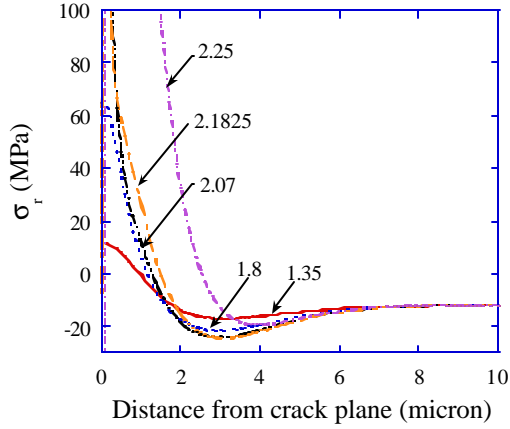


Figure 16. Radial Stress at the Interface.

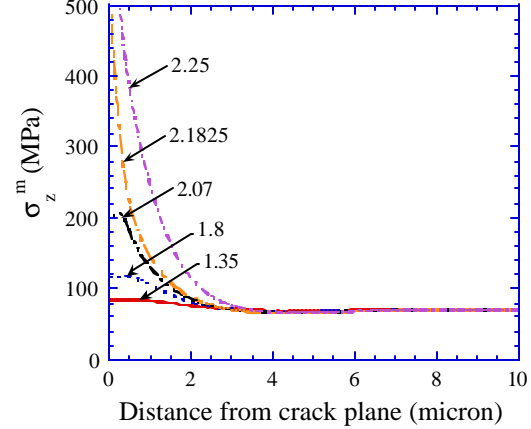


Figure 17. Matrix Axial Stress at the Interface.

2.1 SUMMARY AND RECOMMENDATIONS

The work presented in this study is part of an ongoing effort to support the failure analysis of a unidirectional laminate. Damage observations were made on IM7/5250-4 composite at some selected stress levels. We calculated fiber and matrix stresses at the first sign of damage initiation and examined in some depth two possible damage modes. Some initial predictions were made based on the micromechanics model in conjunction with the limited experimental data that were currently available. The present analysis seemed to favor matrix microcracking (over fiber breakage) as the initiating damage event. However, this could not be verified because no visible damage was observed in the microscope upon unloading from that stress level. The proposed failure scenarios need to be validated by making *in situ* damage observations. Also, the validity of the secondary damage modes needs to be established by making additional observations at other intermediate composite stress levels. Subsequent analytical work will also examine debonding of the fiber-matrix interface in conjunction with fiber breakage and/or matrix microcracking.

3. MICROMECHANICAL RESPONSE OF A MULTIPHASE COMPOSITE

The objectives of this effort were to support the development of a revolutionary ultra-compact combustor in the areas of material selection and analytical modeling. Oxide-oxide ceramic-matrix composites consisting of oxide fibers embedded in an oxide matrix are currently the subject of increased interest due to their inherent resistance to oxidation and excellent tensile and fatigue properties at room and elevated temperatures. In this work we considered 2-D reinforcement of Nextel 720 fibers in an eight-harness satin weave architecture in a matrix consisting of alumina particles, voids, inherent cracks due to the processing conditions, and a silica bonding agent. Predicted quantities included the thermomechanical effective moduli, thermal conductivity tensor and phase stresses due to processing conditions. The effective composite properties, in turn, will serve as input parameters in a 3-D FEM to analyze the stress fields in the combustor under operational conditions. A feedback loop between the FEM and the micromechanical model can now be established to define the evolution of the service-induced damage.

The approach followed a building block scenario in which the microstructure was homogenized at various levels depending on the particular quantities being sought. Firstly, the effective moduli of the multiphase matrix material were computed by use of a three-phase version of the Mori-Tanaka scheme [13-15]. These results were compared with multilevel representations of particles, voids, and binder possible with the NDSANDS model [11]. Secondly, the effect of yarn crimp on the 3-D effective moduli of a composite were determined by comparison of a fabric reinforcement model [16] with that for a cross-ply laminate and also with the straight-fiber micromechanical stiffness model NDSANDS [11]. Since the as-processed composite was known to contain a fairly well defined distribution of cracks normal to the fiber

directions, we next determined the effective moduli of a damaged ply, using the known crack spacing in the Schoeppner-Pagano model [17] and the moduli from Pagano's 3-D exact laminate elasticity theory [18]. Finally, the two cracked layers were assembled and the moduli computed from the exact laminate theory. It was these results which were then compared to experiment and used to assess the quality of the various assumptions invoked in the calculations, and to define the influence of the damage on the effective moduli. Some of those steps are demonstrated below as significant results.

For the material system under consideration, the homogenized matrix consisted of the stiff alumina particles finely dispersed in silica with a significant amount of porosity. We therefore assumed that both the alumina particles and the pores were spherical in shape. Using the handbook material properties of alumina ($E=310$ GPa, $\nu=0.15$, $\alpha=8.5 \text{ e-}6/^{\circ}\text{C}$, $\mu=10$ W/m-K) and silica ($E=72$ GPa, $\nu=0.16$, $\alpha=0.5 \text{ e-}6/^{\circ}\text{C}$, $\mu=1.75$ W/m-K), the effective matrix properties were evaluated as

$$E_m = 69.8 \text{ GPa}, \nu_m = 0.18, \alpha_m = 7.44 \text{ e-}6/^{\circ}\text{C}, \mu_m = 2.66 \text{ W/m-K}$$

using particle and void content of 0.52 and 0.34, respectively, in the matrix. Secondly, the effect of yarn crimp on the 3-D effective moduli of a composite was determined. The homogenized matrix moduli were assumed in this comparison. The fabric itself was an eight-harness satin, which could also be approximated by a cross-ply laminate. Assuming that no initial damage was present and using $E_f=262$ GPa, $\nu_f=0.25$, $\alpha_f=6.0 \text{ e-}6/^{\circ}\text{C}$, $\mu_f=5.9$ W/m-K, for Nextel 720 fiber, we evaluated the following properties for the undamaged fabric,

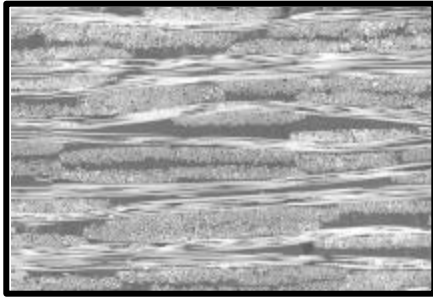
$$\begin{aligned} E_x = E_y = 136.3 \text{ GPa}, E_z = 116 \text{ GPa}, \nu_{xy} = 0.1859, \nu_{xz} = \nu_{yz} = 0.2130 \\ G_{xy} = 49.42 \text{ GPa}, G_{xz} = G_{yz} = 48.75 \text{ GPa}, \alpha_x = \alpha_y = 6.502 \text{ e-}6/^{\circ}\text{C}, \alpha_z = 6.719 \text{ e-}6/^{\circ}\text{C} \\ \mu_x = \mu_y = 3.935 \text{ W/m-K and } \mu_z = 3.752 \text{ W/m-K}, \end{aligned}$$

where x-y was the fabric plane and z was the thickness direction, and the fiber volume fraction was 0.45. These computed thermoelastic constants using NDSANDS [11] were in very good agreement with the analytical results of Naik [16], where the actual fiber architecture shown in Figure 18 was considered in a unit cell, thereby supporting our approximation of the fabric.

$$E_x = E_y = 71 - 87 \text{ GPa}, E_z = 47 - 53 \text{ GPa}, \nu_{xy} = 0.07 - 0.11, \nu_{xz} = \nu_{yz} = 0.12, G_{xy} = 17 \text{ GPa}, \\ \alpha_x = \alpha_y = 5.85 - 6.73 \text{ e-6/}^\circ\text{C}, \alpha_z = 6.99 \text{ e-6/}^\circ\text{C}, \mu_x = 2.15 \text{ W/m-K}, \mu_z = 1.62 \text{ W/m-K},$$

so that the effective property predictions were much too high. However, on close examination, extensive damage in the form of transverse matrix cracking was observed as a result of the shrinkage which occurred during pyrolysis processing [19], as seen in Figure 19. These microcracks were distributed throughout the composite with spacing ranging from 50 to 200 μm prior to machining and testing and were simulated using the large radius axisymmetric damage model [17].

We next determined the effective moduli of a damaged ply using the known crack spacing in the Schoeppner-Pagano model [17] and the moduli from Pagano's 3-D exact laminate elasticity theory [18]. Finally, the two cracked layers were assembled and the composite moduli computed from the exact laminate theory. This procedure was repeated over the entire range of crack spacing measurements. The results of these calculations are shown in Figure 20. This modeling approach, which incorporated the presence of transverse cracking, was seen to produce very good agreement with the experimental measurements for all of the effective thermoelastic moduli, except E_z . Since the transverse cracks were aligned in the thickness direction, they did not influence the modulus in that direction, which remained unchanged from the previously reported undamaged value. Traditionally, a more simplified approach to modeling discrete damage is the property degradation model in which the stiffness of the load-carrying element is



1 mm

Figure 18. Microstructure of Woven Nextel 720/AS.



200 μm

Figure 19. Magnified View of Microstructure Showing Matrix Cracks Due to Processing.

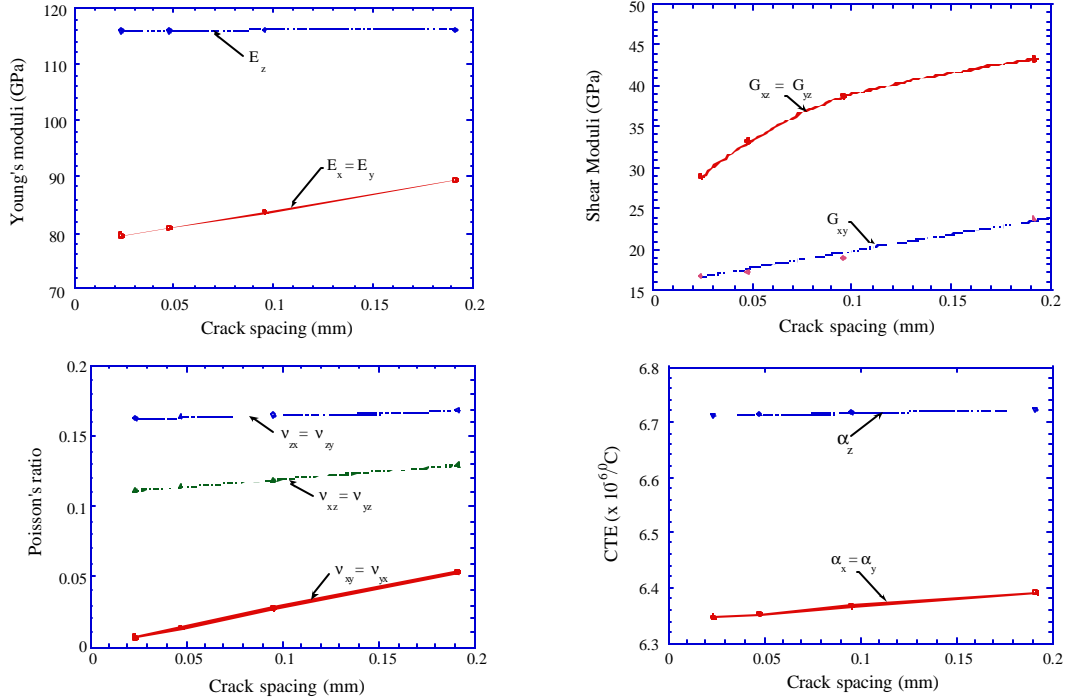


Figure 20. Effective Thermoelastic Moduli of Woven Nextel 720/AS Composite as a Function of Transverse Crack Spacing.

reduced to reflect the presence of damage. In the present case we degraded the elastic modulus of the matrix material. A parametric study revealed that a matrix elastic modulus of 20 GPa (reduced from undamaged value of 69.8 GPa) resulted in a reasonably good match with

experiments for composite Young's moduli in both thickness and in-plane directions, as shown in Table 6.

Next, to calculate more accurate phase stresses so that the failure characteristics could be predicted, we replaced the previous layer models with a concentric cylinder model [9] in which the distinct fiber and homogenized matrix phases were recognized, along with a micromechanical representation of the damage. The latter damage mode consisted of fiber-matrix debonding (over half the fiber surface) coupled with matrix cracks emanating from the debond tips (and aligned in the thickness direction). This model could now be checked for consistency with the damage observations. As shown in Table 6, the prediction of the in-plane Young's modulus from the micromechanics model [9] agreed well with the experimental data. As opposed to straight transverse cracks in the thickness direction in the laminate model [17], the micromechanics model, which considers 180-degree fiber-matrix debonding in conjunction with radial matrix cracking, now leads to a reduced modulus in the thickness direction (as compared to the undamaged value). The predicted value of E_z (72 GPa) was still higher than the average value of 50 GPa measured in the thickness direction. To realize the smaller values of E_z which were measured, we once again appeal to the layer model [17] but this time considered delamination between the 0- and 90-degree plies in addition to transverse cracking. It was assumed that ply delamination simulated fiber-matrix debonding, which could occur in conjunction with transverse cracking. The predictions of this simulation are also shown in Table 6 for a delamination length of 42 μm and transverse crack spacing of 48 μm . These predictions of Young's moduli seemed to reinforce the hypothesis that an additional damage mode, such as fiber-matrix debonding or delamination, was occurring in conjunction with transverse cracking, which in turn leads to a lower value of E_z and thus a better match with the measurements.

Table 6
Comparison of Experiments with Predictions Simulating Various Failure Modes

	$E_x = E_y$, GPa	E_z , GPa
Experimental Measurements	71-87	47-53
Laminate model {Undamaged}	136	116
Laminate model {Transverse cracking, 25 to 200 μm crack spacing}	80-89	116
Matrix Degradation { $E_m = 20$ GPa}	86	43
Micromechanics model {Transverse cracking + interfacial debonding}	86	72
Laminate model {Transverse cracking (48 μm crack spacing) + delamination (42 μm length)}	78	55

Lastly, Lu and Hutchinson [20] have shown that matrix cracking in combination with interfacial debonding has the potential for significantly reducing the overall longitudinal thermal conductivity of a unidirectional fiber-reinforced composite. Recently, Islam and Pramila [21] used FEM to consider combined effects of partial debonding and matrix cracking on the effective transverse thermal conductivity of fiber-reinforced composites. They concluded that the reduction of effective thermal conductivity may be as large as 50 percent when the interfacial conductance is reduced by two decades. In the absence of a suitable model for evaluating thermal conductivity of the damaged fabric, our analytical predictions for the undamaged fabric represent upper bound results and are therefore significantly higher than the measured values for the damaged fabric.

In summary, we have demonstrated that discrete damage modeling was *essential* for effective property estimation. From the mechanics viewpoint, we have provided a set of analytical tools and experimental protocol to enact true composite material design for high-temperature applications. Aside from the oxide-oxide class of composites (or possibly another form of ceramic-matrix composite), the methodology is also appropriate for application to

structural carbon-carbon composites which have numerous functions in thermal protection systems and other space vehicle applications.

4. SINGLE-FIBER PUSHOUT CONSIDERING INTERFACIAL FRICTION AND ADHESION

We completed work on this topic and published a journal paper [22] on this subject. The paper presented an effort to understand the complexity of stress distributions and deformation fields at the fiber-matrix interface in a typical single-fiber pushout specimen subjected to a variety of interface conditions. Two numerical methods, a stress-based Reissner's variational solution and the displacement-based FEA, were used to compute the numerical solutions. The fiber-matrix interface conditions considered included zones with perfect bonding, frictional contact (stick/slip) and open crack faces. The location, size, and progression of the interface zones were selected to mimic realistic (from experimental findings) and other typical interfacial damage growth during the pushout test. Load cases examined include the residual stress due to chemical shrinkage during specimen processing and the applied pushout loading. The discussion presented in the paper focused on two aspects of fiber pushout testing. The first aspect was extracting information pertaining to the material behavior from the load-displacement curves. The second aspect was deducing the nature of the interface from the test results with the assistance of the numerical simulations.

It was shown that the stress distributions and the progression of interface zones largely depend upon the initial state of the interface. Comparisons were made illustrating the differences in the stress fields due to adhesive (no relative axial displacement throughout the loading history) and stick (no relative axial displacement during the last load increment but may have nonzero total relative axial displacement) interface conditions. These differences could become extremely important in the interpretation of analytical results.

It was further pointed out that although knowledge of the initial damage and state of the interface in the specimen was required, the presence or absence of adhesion at the interface could

be inferred and characterized based on numerical simulations. An indicator for the presence of adhesion at the interface was the maximum load carried by the specimen. A three-step methodology was presented which, when used in concert with the experimental results, could be used for assessing the nature of the interface and the extent of adhesive bonding. However, one could not define the detailed zones if adhesion was present unless one determined the debond length throughout the test [perhaps by the nondestructive evaluation (NDE) method] or had a valid debond initiation criterion. Some of the suggested simulations extended beyond the normal pushout testing protocol.

Finally, given the properties and the initial state of the interface, the stress distributions at the fiber-matrix interface were shown to be affected by the size and order of the interface zones and the singularities at the zone transitions. The boundary conditions at the interface changed continuously with pushout loading leading to a continuous change in order and size of interfacial zones. A series of stress distributions were presented under several interface conditions to illustrate the complexity of stress distributions during interfacial zone growth in the single-fiber pushout testing. These stress distributions highlighted that neither simplified shear-lag analyses nor local asymptotic analyses could capture the stress fields that drove the interfacial damage development in this specimen. Accurate global analyses were necessary to capture the various mechanisms in progress during the pushout testing.

5. PARAMETRIC DESIGN, ANALYSIS, AND TESTING OF A MODEL WOVEN COMPOSITE WITH A CRUCIFORM GEOMETRIC CONFIGURATION

To achieve the optimum structural properties of state-of-the-art fabric reinforcements of woven composites, there is a need to develop a basic understanding of deformation and damage mechanisms. The failure in textile composites in general occurs in the vicinity of two perpendicular yarns crimping over and under each other. *In situ* experimental observation [23] of damage initiation in textile composites reveals that the damage initiates in the form of interface cracks in the vicinity of yarn crimping, which is strongly influenced by the interlaminar stresses at the interface region. Thus an accurate prediction of the interlaminar stresses at the interface region is needed to reliably analyze damage and failure in woven composites.

The B-SAM is a previously developed computer program for the 3-D analysis of anisotropic laminated composite structures, including bonded joints and bolted joints. The B-SAM has the advantage of an efficient modeling and solution scheme through the use of overlapping B-spline-based shape functions [24,25]. The overlapping nature of the approximation functions keeps a minimal bandwidth profile in the stiffness matrix of the system of equations. While the conventional FE (p-element) has C^0 continuity, m -th order spline functions have $C^{(m-1)}$ continuity, which yields continuous derivatives up to the $(m-1)$ -th order. Therefore, stress and strain fields as well as the displacements are evaluated continuously within the homogeneous domain (subregions) with the spline method. The homogeneous domain discretized with n subdivisions in one direction needs $(n+m)$ overlapping m -th order spline functions. Figure 21 shows an example of cubic splines overlapped on seven subdivisions. The spline functions are evaluated with a recursive formula developed earlier [26].

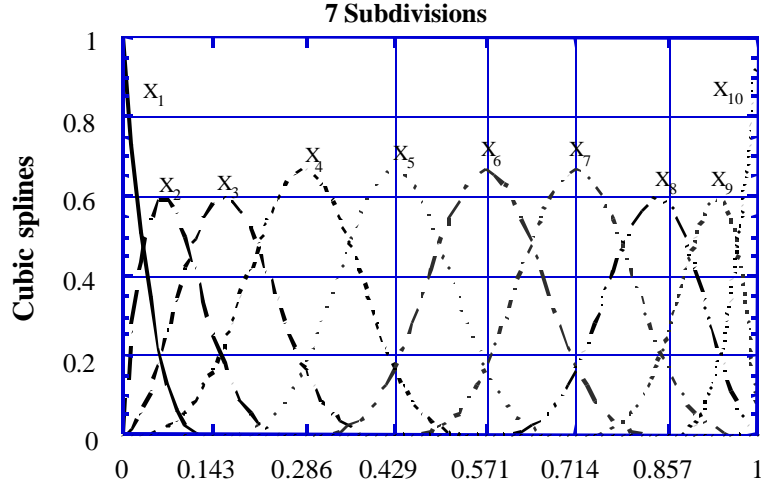


Figure 21. Overlapping Cubic B-Spline Functions with Seven Subdivisions.

The B-SAM was modified to accommodate the curved geometry of woven composites with a curvilinear transformation. Two tensor transformations were needed for setting up a global constitutive relation between the global stresses and strains: one for the fiber orientation along the yarns and the other for the yarn crimping with respect to the global coordinate system. The first one was for the coordinate transformation between material principal axes (on-axes) and off-axes following yarn crimping.

The B-SAM was applied to the analysis of a unit cell of a plain-weave textile composite to examine how well the solution satisfies interlaminar traction continuity conditions at the yarn interfaces. The B-SAM was also used to analyze a model woven composite with 1-D yarn crimping. The maximum stress failure criterion was applied to the stress field solution to predict the initial failure strength and the damage mode of the 1-D model laminate. As observed from experimental and numerical analysis of the model laminate with a straight edge, matrix cracking was initiated at the free edge of the transverse fill yarn perpendicular to the loading direction [27]. Such a failure mechanism, caused by the free edge, was not desirable for the analysis of

the woven composites because most of the interest lies in the effect of yarn crimping. Therefore, to eliminate the free-edge effect, cruciform specimens were used in this study.

In an attempt to validate analytical predictions, Moiré interferometry was employed to obtain an accurate full-field distribution of in-plane strain on the face of the cruciform specimen.

5.1 NUMERICAL RESULTS AND PARAMETRIC STUDY

5.1.1 Unit Cell of Plain-Weave Composite

The B-SAM was applied to the analysis of a unit cell of a plain-weave textile composite. The unit cell of the model was divided into several homogeneous subregions; each subregion was occupied by a characteristic fabric yarn or a matrix, as shown in Figure 22. L_x and L_y are the length of the unit cell in the x - (warp) and y - (fill) directions, and t_w and t_f half of the thickness of the warp and fill yarns, respectively. The yarns were assumed to be transversely isotropic, and the matrix was assumed to be isotropic. Each yarn and matrix subregion of the unit cell was discretized into several subdivisions in the longitudinal and transverse directions. Cubic splines were used as the approximation functions of the unknown variables in the x -, y - and z -directions. A boundary condition applied to the unit cell was as follows:

$$\begin{aligned} u(0, y, z) &= 0 \quad , \quad u(L_x, y, z) = U_o \\ v(x, 0, z) &= v(x, L_y, z) = 0 \\ w(x, y, 0) &= 0 \end{aligned} \tag{3}$$

Analysis was carried out to calculate the stress components along the yarn boundaries. The stresses calculated in the global coordinate axes were transformed into the local coordinate axes along the yarn crimping. Alternatively, these local stress components along the interfacial surfaces were related with global stress components by the slopes of the interfacial

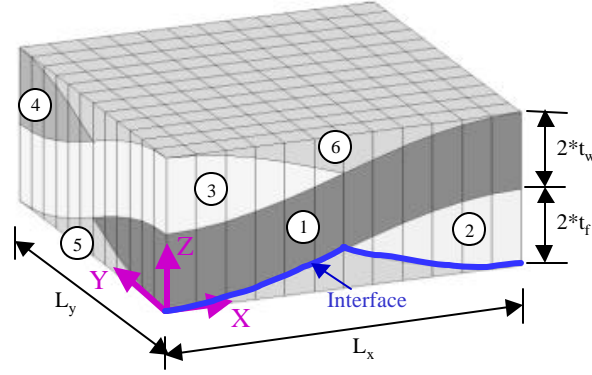


Figure 22. Unit Cell of a Plain-Weave Composite. Numbers in circles indicate the numbers of subregions. Subregions 1 and 4 represent warp yarns, 2 and 3 represent fill yarns, and 5 and 6 represent matrix material.

surfaces in the x - and y -directions ($h_{2,x}^{(k)}$ and $h_{2,y}^{(k)}$), where k denotes the subregion number. The normal and shear stress components along the yarn interface boundary were thus calculated with the following relations:

$$\begin{aligned}\hat{\mathbf{s}}_3^{(k)} &= \mathbf{s}_3^{(k)} - h_{2,x}^{(k)} \cdot \mathbf{s}_5^{(k)} - h_{2,y}^{(k)} \cdot \mathbf{s}_4^{(k)} \\ \hat{\mathbf{s}}_4^{(k)} &= \mathbf{s}_4^{(k)} - h_{2,x}^{(k)} \cdot \mathbf{s}_6^{(k)} - h_{2,y}^{(k)} \cdot \mathbf{s}_2^{(k)} \\ \hat{\mathbf{s}}_5^{(k)} &= \mathbf{s}_5^{(k)} - h_{2,x}^{(k)} \cdot \mathbf{s}_1^{(k)} - h_{2,y}^{(k)} \cdot \mathbf{s}_6^{(k)},\end{aligned}\tag{4}$$

where $\hat{\mathbf{s}}_i^{(k)}$ and $\mathbf{s}_i^{(k)}$ are the stress components at the interface of the k -th subregion in local and global coordinate axes, respectively. The subscript (k) will be dropped later in this section unless it explicitly refers to a different subregion.

Figure 23(b-d) shows the normal ($\hat{\mathbf{s}}_3 = \hat{\mathbf{s}}_z$) and shear ($\hat{\mathbf{s}}_4 = \hat{\mathbf{t}}_{yz}$, $\hat{\mathbf{s}}_5 = \hat{\mathbf{t}}_{xz}$) stress distributions along three interfacial lines in Figure 23(a). The stress distributions plotted with triangles and circles were evaluated from the upper and lower subregions, respectively. The results show an excellent agreement with the interfacial normal and shear stresses from the lower and the upper subregion, which indicates the present method is a reliable way of calculating the interlaminar stresses. Note that one of the shear stress distributions, Figure 23(c), shows a large

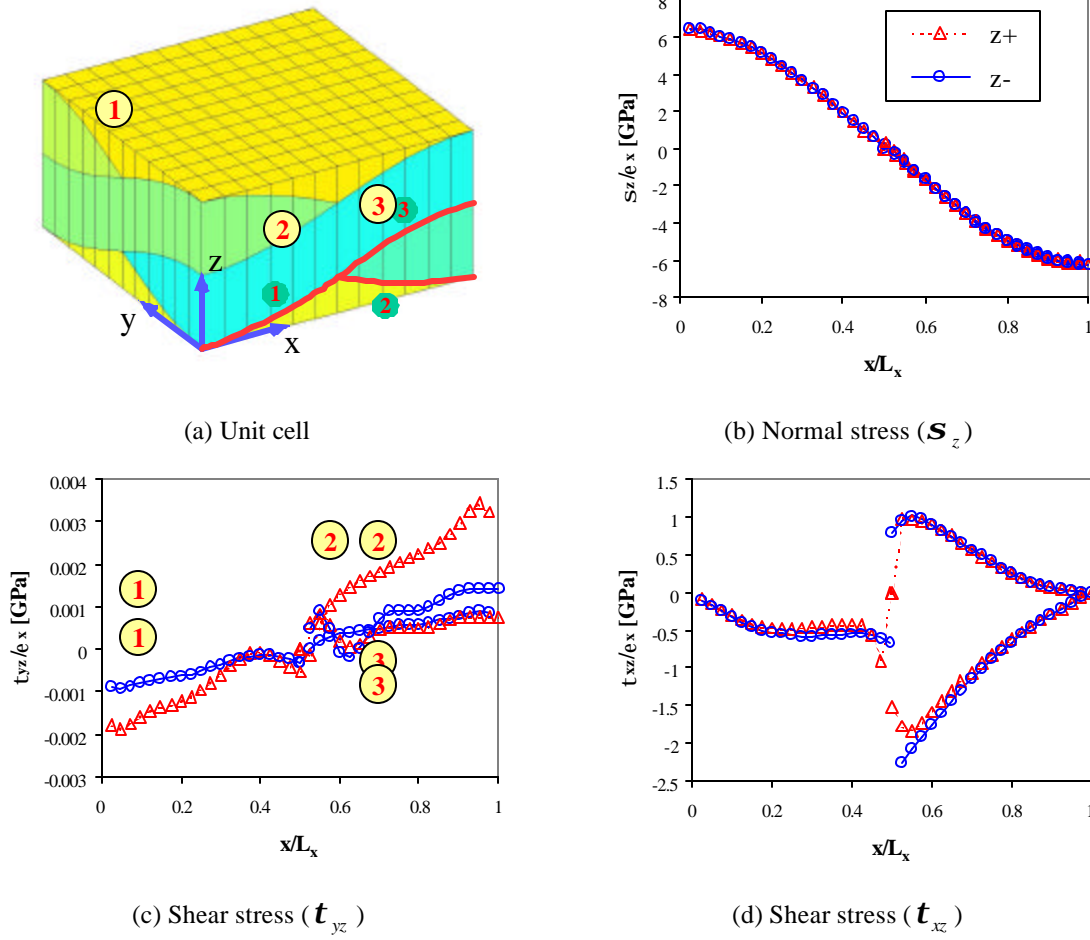


Figure 23. Interfacial Normal and Shear Stress Distributions of a Unit Cell of a Plain-Weave Textile Composite.

discrepancy between the lower and upper stress values. This component is numerically less significant than the other stress components, Figure 23(b,d), when comparing the absolute magnitude of the stress components. Figure 23(d) shows a shear stress jump in the middle of the distribution where the material properties are discontinuous. At this point the stress has weak singularity due to the material discontinuity and thus causes a high stress gradient. The reason for the stress singularity in the local shear stresses is that the stress components cannot be determined uniquely because of the zero thickness of subregion 3 at the singular point. While two subregions (subregions 5 and 1) were considered in calculating the interfacial stresses at the

left-hand side of $x = L_x/2$, three subregions (subregions 5, 3 and 1) were considered in the calculation at the right-hand side. In general, it was impossible to satisfy such a continuity condition at the singular point with polynomial approximation functions, including splines. At this singular point an asymptotic approach should be used to determine accurate stress components.

5.1.2 1-D Model Laminate with Cruciform Geometry

A model woven composite with 1-D yarn crimping was analyzed numerically and experimentally. The B-SAM yielded accurate and continuous stress field solutions in warp and fill yarn subregions. The solution also satisfied interlaminar traction continuity conditions at the yarn interfaces. The maximum stress failure criterion was applied to the stress field solution to predict the initial failure strength and the damage mode of the 1-D model laminate.

As observed from experimental and numerical analysis of the model laminate with a straight edge, the matrix cracking failure was initiated at the free edge of the transverse fill yarn perpendicular to the loading direction. Such a failure mechanism, caused by the free edge, was not desirable for the analysis of the woven composites because most of the interest lies in the effect of yarn crimping. Therefore, to eliminate the free-edge effect, cruciform specimens were used in this study. Figure 24 shows one quarter of the cruciform geometry that is cut by symmetric planes and meshed for numerical analysis.

The general configuration of the cruciform specimen was with arms loaded in tension and arms that were free from loading. The specimen had a $[90/0]_s$ stacking sequence everywhere except along the centerline of the unloaded arms where the stacking sequence was reversed to $[0/90]_s$. This resulted in a specimen with a 1-D woven configuration across the specimen width, extending down the unloaded arms. The purpose of the cruciform geometry

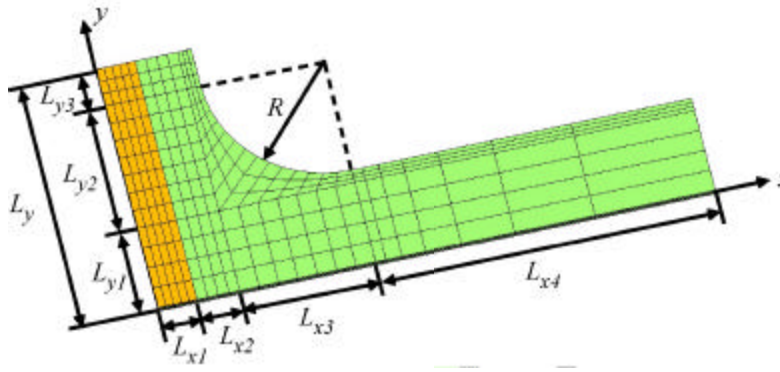


Figure 24. Dimensions and Geometry of One Quarter of a Cruciform Specimen.

was to position the free edge of the woven portion of the composites away from any loading (i.e. at the ends of the unloaded arms).

Nontrivial stress components were taken into account and applied by the maximum-stress failure criteria to calculate a failure index. The failure index (k) is the ratio of the stress component to the failure strength of the composite material. The stress concentration factors were calculated by taking all stress components at the bottom, middle and top surfaces of each yarn (lower fill [90°], middle warp [0°] and upper fill [90°]).

Figure 25 shows concentration factors of an in-plane longitudinal stress (\mathbf{s}_1) along the middle of the transverse fill yarn and out-of-plane shear stress (\mathbf{s}_5) along the middle of the longitudinal warp yarn. The stress concentration factors ($k_1 = \mathbf{s}_1/Y$, $k_5 = \mathbf{s}_5/S_{13}$) were normalized by a nominal stress concentration factor ($k_a = \mathbf{s}_a/Y$), where \mathbf{s}_a was an applied stress on the fill yarn away from the yarn crimping region, and Y and S_{13} were transverse and shear strengths of the fill and warp yarns, respectively. While the straight-edge specimen yielded the highest stress concentration at the free edge, the cruciform specimens eliminated the free-edge effect. Furthermore, the cruciform specimens yielded higher shear stress concentration at

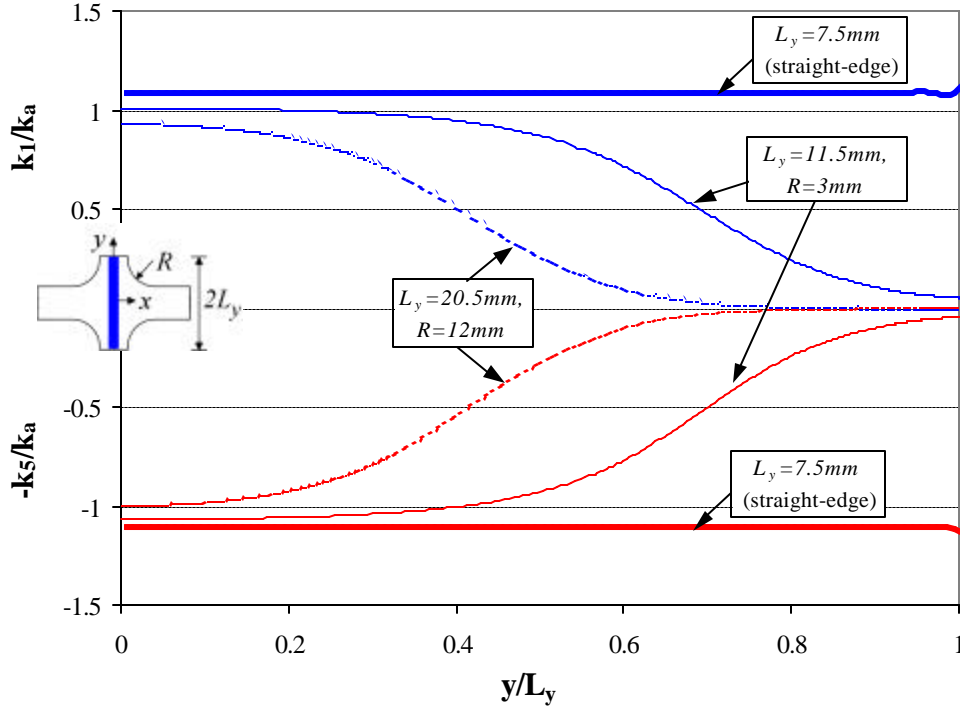


Figure 25. Normalized In-Plane Longitudinal and Out-of-Plane Shear Stress Concentration Factors Along the Middle of Transverse Fill Yarn in 1-D Model Laminate.

the longitudinal warp yarn than the axial stress concentration at the transverse fill yarn. The high shear stress concentration may cause the damage at the yarn crimping area in a delaminating failure mode, which may increase the yarn crimping effect of the woven composites.

While the cruciform specimens eliminated the free-edge problem and increased the yarn crimping effect, it caused a stress concentration at the fillet region as well. A parametric design study was conducted to determine the optimum cruciform geometric configuration for a 1-D model woven composite to identify a specimen configuration that leads to failure of the composite material caused by the textile configuration and not because of the external geometry of the specimen. The parametric study focused on producing a geometry where failure was more likely to occur in the center gage section of the specimen.

Figure 26 shows the ratio of stress concentration factors in the fillet region, $(k)_{fillet}$, to those of the woven region at the yarn crimp, $(k)_{woven}$. The stress analysis indicated that the transverse tensile stress was always maximum at the middle surface of the 90° ply in the fillet region, and therefore $(k)_{fillet} = \sigma_1 / Y$. Meanwhile, the woven stress concentration factor was calculated by the method described earlier, and therefore $(k)_{woven} = k_I$ or k_5 depending on the failure mode. Figure 26(a-c) shows that the fillet stress concentration was greater than the woven stress concentration.

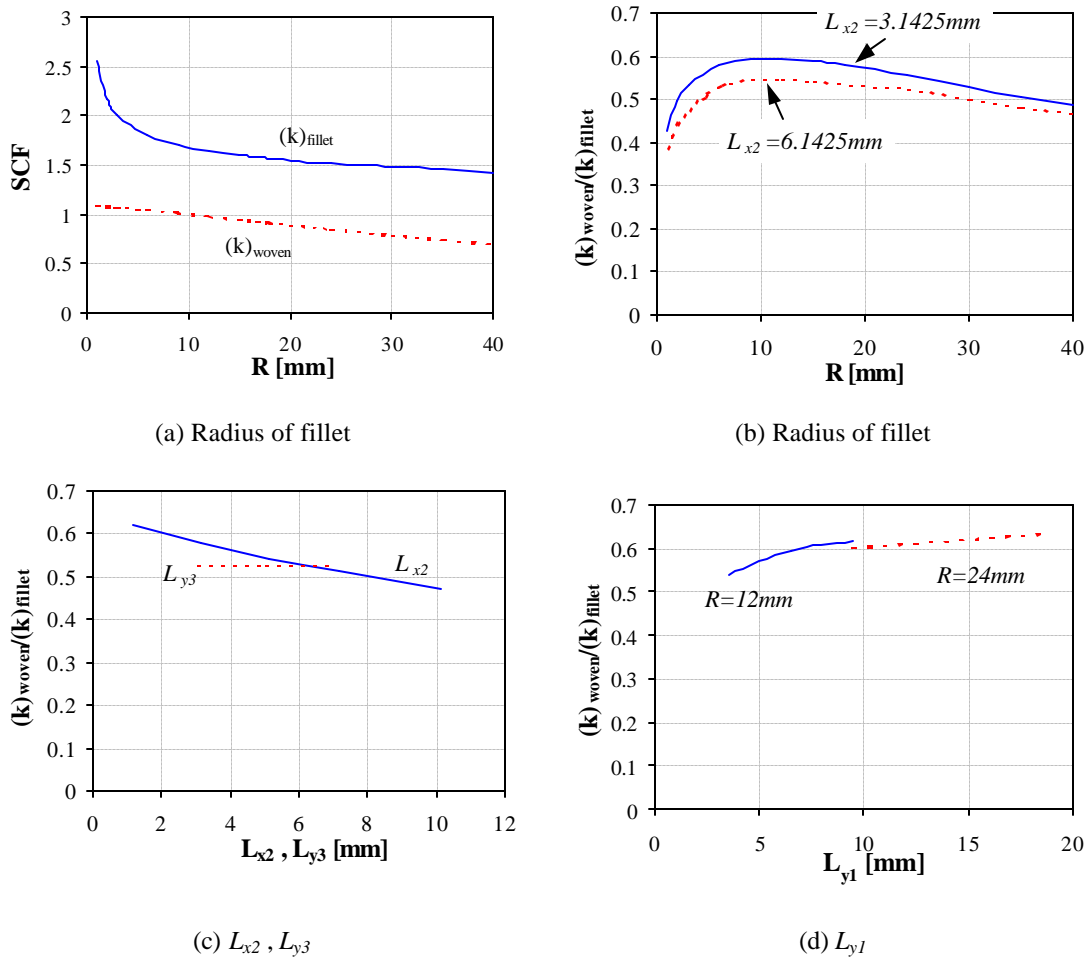


Figure 26. Ratio of Stress Concentration Factors of Woven to those of Fillet with Various Dimensions of the Cruciform Specimen Geometry.

The effect of the fillet stress concentration can be reduced by designing the cruciform specimens by varying the dimensions of the cruciform geometry. The fillet stress concentration reduced rapidly with the increase of the fillet radii, as shown in Figure 26(a,b). However, as the fillet radius increased further, the stress at the yarn crimp also became less concentrated, and the rate of the reduction of the woven stress concentration factor became greater than that of the fillet concentration factor. Therefore, an optimal fillet radius can be found to maximize the possibility of the failure due to the yarn crimp. The same effect can be achieved by decreasing L_{x2} or increasing L_{y1} , as shown in Figure 26(c,d). However, L_{y3} had no influence on the ratio of two stress concentrations.

While the woven stress concentration can be maximized with respect to the fillet stress concentration with optimal dimensions of the test specimens, it can be further affected by varying the yarn waviness ratio. Figure 27 shows a result of the parametric study by varying the yarn waviness ratio. Different yarn waviness ratios were obtained by changing L_{x1} in Figure 24. At low waviness ratio, the woven composite failed by transverse matrix cracking either in the lower or upper fill yarns. As the waviness ratio increases, out-of-plane shear failure became dominant at the middle warp yarn. Furthermore, at approximately $a/\lambda = 0.087$, the woven stress concentration exceeded the fillet stress concentration, so that we can expect the initial failure in the yarn crimp rather than in the fillet.

5.2 EXPERIMENT AND VALIDATION

Test specimens were prepared by embedding the model yarn crimping in a composite plate. After drilling four holes at the locations of the fillet, the plate was cut with a diamond saw in the longitudinal and transverse directions at points tangential to the hole edges. This produced the loaded and unloaded arms of the cruciform specimen.

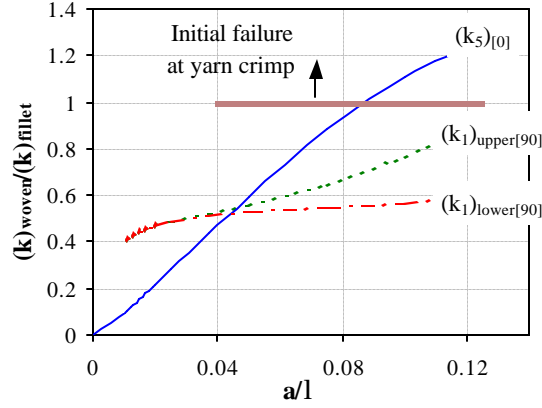


Figure 27. Ratio of Stress Concentration Factors of Woven to those of Fillet with Various Yarn Waviness Ratio.

The geometry of the test specimen was set based on the above parametric study as follows: $L_{x1} = 1/2 = 2$, $L_{x2} = 3.8575$, $L_{x3} = 10.0302$, $L_{x4} = 15.9893$, $L_{y1} = 7.1402$, $L_{y2} = 10.0302$, $L_{y3} = 0$, $R = 9.525$ (units in mm). Half of the thickness of the warp and fill yarns were measured by micrographs of the cross section as $t_w = 0.128$ mm and $t_f = 0.124$ mm, respectively, which made the yarn waviness ratio be $a/l = 0.063$. Figure 28 shows good agreement between the measured actual geometry and the modeled geometry expressed with sinusoidal functions.

Moiré interferometry [28] was employed to obtain a full-field distribution of displacements and strains on the face of a cruciform specimen of optimum geometry. A 1,200-lines/mm crossline diffraction grating was replicated onto the face of the cruciform specimen. The specimen was loaded to approximately 900 N, and displacement fringe patterns were recorded. Digital phase shifting of the type detailed in Lassahn, et al. [29] was used to produce a full-field digital array of displacement values over the central region of the specimen. Numerical differentiation was used to calculate the in-plane surface strain components.

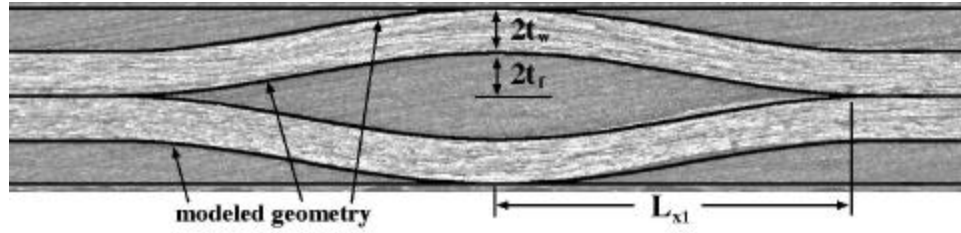


Figure 28. Comparison of Measured and Modeled Cross-Section Profiles of Model Woven Composite.

Figure 29 shows a comparison between B-SAM and Moiré interferometry results. The B-SAM results were scaled to match the far-field axial traction applied in the experiment. The Moiré interferometry results have been smoothed slightly. Also, because of slight bending of the specimen during the experiment, the Moiré results have been averaged in a symmetric arrangement about both the x -axis and the y -axis. Thus, the close-up Moiré results presented in Figure 29 are symmetric about the x - and y -axes.

Good agreement between the experimental and numerical results is clearly evident. The other two components of experimentally measured in-plane strains yielded similarly good agreement with the B-SAM results. All of the in-plane strain components showed rapid variation and high magnitude in the fillet region. However, only the axial strain showed significant variation in the region of yarn crimping. Nonaveraged Moiré results from the fillet region, not shown in this paper, also displayed a close match with the B-SAM predictions.

5.3 SUMMARY AND RECOMMENDATIONS

A B-SAM with overlapping B-spline approximation functions of displacements along with a curvilinear transformation was developed and applied to a 3-D analysis of a woven textile composite. Special interest was given to the reliable calculation of interlaminar stresses at the interfaces between yarn/yarn and yarn/matrix. A unit-cell of plain-weave composite and a model woven composite with 1-D yarn crimping were analyzed numerically to calculate the stresses

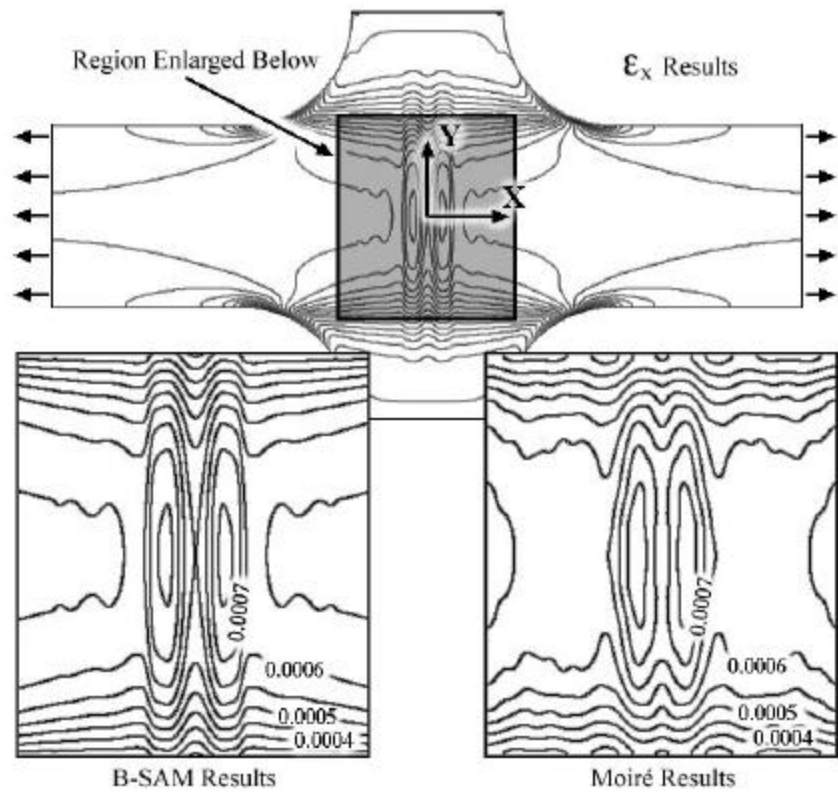


Figure 29. Axial Strain Comparison between B-SAM Predictions and Moiré Interferometry Measurements. (Note that the Moiré interferometry results were averaged in a symmetric manner about the x- and y-axes.)

and to predict failure strength and damage mode. Cruciform specimens were used to eliminate free-edge stress concentration of the model woven composite by positioning the free edge of the woven portion of the composites away from any loading.

A parametric design study was conducted to determine the optimum cruciform geometric configuration for the 1-D model woven composite to identify a specimen configuration that led to failure of the composite material caused by the textile configuration and not because of the external geometry of the specimen. The parametric study focused on producing a geometry where failure was more likely to occur in the center gage section of the specimen.

Moiré interferometry was employed to obtain an accurate full-field distribution of in-plane strains on the face of the cruciform specimen. These data showed good agreement with the numerical results obtained with B-SAM.

6. ASYMPTOTIC STRESS ANALYSIS OF LAMINATED COMPOSITES WITH SLANTED FREE EDGE

As lightweight and high stiffness/strength material, laminate composites have been used in many structural applications, such as airplanes, ships, automobiles, sporting goods, etc. An optimum design of the composite structures is based on an analysis of deformation and stress behavior of the composites. A prevailing method in the analysis of laminate composites is a ply-level homogenized model, which considers the lamina as homogeneous orthotropic material. The ply level model, however, results in singular stress behavior in the vicinity of the ply interface and laminate edge. The singular stress is caused by material discontinuity of the plies when the stress tries to satisfy traction continuity conditions at the laminate free edge.

Many attempts were made to solve the straight free-edge problems of laminated composites. A mixed approximation of displacement and stress components was proposed by Pagano [30,31] using Reissner's mixed variational principle. Without the precise singular stress terms, the mixed method demonstrated a highly reliable calculation of the stress fields including interlaminar stress components. Wang and Choi [32] constructed an infinite series elasticity solution for composite wedge near the ply interface and the wedge edge based on Lekhnitskii's complex variable stress function. The pioneering work by Wang and Choi [32] was extended by Folias [33] and Wang and Lu [34] to carry out an asymptotic solution for interlaminar stresses at the interface around an open-hole edge of a composite plate. They showed that the singular stress solution at the ply interface around the curvilinear hole edge is equivalent to that for the straight edge, provided that a ply orientation with respect to the direction tangential to the hole edge remains the same as the ply orientation in the straight edge, with respect to the edge

direction. Power of stress singularity was found to be dependent upon the location at the hole edge.

Iarve [35] developed a B-SAM for 3-D stress solution of laminated composites with the open hole. A numerically calculated stress solution near the hole edge by this method was compared with one given by the singular term from the asymptotic solution. At the singularity, the polynomial spline approximation did not capture directional nonuniqueness of singular stress functions. However, it was observed that the singular term of the asymptotic solution with appropriate coefficient and constant additive terms matched the full-field spline solution to a distance of approximately one half-ply thickness from the singular point. The large area of agreement suggested a hybrid method by superposing the singular term with the polynomial approximation to determine stress field more efficiently and reliably without a tremendously large amount of mesh refinement near the singular free edge.

The present work extended the asymptotic analysis to the problems where the straight free edge is no longer perpendicular to the ply interface. The slanted free edge can easily be found on composite joining, such as in countersunk open holes, scarf-lap bonded joints, etc. The asymptotic solution was to be compared with the full-field spline approximation. A good understanding of the singular behavior near the slanted edge will lead to the development of the hybrid method for the efficient and reliable stress analysis of slanted laminated composite structures.

6.1 ASYMPTOTIC ANALYSIS

For an asymptotic analysis, three coordinate systems were introduced for laminated plies with slanted free edges as follows (see Figure 30):

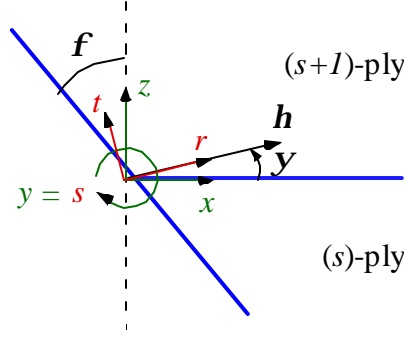


Figure 30. Global and Local Coordinate Systems in Asymptotic Analysis.

1. xyz : a global axis in a Cartesian coordinate system.
2. rst : a local axis in a Cartesian coordinate system.
3. hyz : a local axis in a cylindrical coordinate system.

Note that the local axes were variant with the angle (\mathbf{y}). An assumption was made that the laminate is infinitely long in the global y -direction (or local s -direction), so that the analysis was focused on a 2-D cross section on the global xz -plane (or local rt -plane). A singular point, which is the center of each coordinate system, was located at the intersection of the free edge and the interface between (s)-th and ($s+1$)-th plies.

In the local coordinate systems (hyz), \mathbf{h} is a dimensionless parameter defining the distance from the free edge, and \mathbf{y} is an angle defining the direction in which the singular point is approached. In this coordinate system, $0 \leq \mathbf{y} \leq \frac{\mathbf{p}}{2} + \mathbf{f}$ in the upper ply and $-\frac{\mathbf{p}}{2} + \mathbf{f} \leq \mathbf{y} \leq 0$ in the lower one, where \mathbf{f} is the slanted angle at the free edge.

The global (xyz) and the local Cartesian coordinate systems (rst) were related with the following local transformation:

$$\begin{Bmatrix} x \\ y \\ z \end{Bmatrix} = \begin{bmatrix} m_1 & 0 & -n_1 \\ 0 & 1 & 0 \\ n_1 & 0 & m_1 \end{bmatrix} \begin{Bmatrix} r \\ s \\ t \end{Bmatrix}, \quad (5)$$

where $m_1 = \cos \mathbf{y}$ and $n_1 = \sin \mathbf{y}$. Meanwhile, the global (xyz) and the local coordinate systems ($\mathbf{h}\mathbf{y}\mathbf{z}$) at the cross section were related with the following local transformation:

$$x = \mathbf{h} \cos \mathbf{y}, \quad y = -\mathbf{z}, \quad z - z^{(s)} = \mathbf{h} \sin \mathbf{y}, \quad (6)$$

where $\mathbf{h} \geq 0$ and $(-\mathbf{p}/2 + \mathbf{f}) \leq \mathbf{y} \leq (\mathbf{p}/2 + \mathbf{f})$. For an arbitrary function $F(\mathbf{h}, \mathbf{y}, \mathbf{z})$, one can write

$$\frac{\mathbb{I}F}{\mathbb{I}x} = \Lambda_t F, \quad \frac{\mathbb{I}F}{\mathbb{I}y} = -\frac{\mathbb{I}F}{\mathbb{I}z}, \quad \frac{\mathbb{I}F}{\mathbb{I}z} = \Lambda_n F, \quad (7)$$

where

$$\Lambda_t F = \cos \mathbf{y} \frac{\mathbb{I}F}{\mathbb{I}h} - \frac{\sin \mathbf{y}}{h} \frac{\partial F}{\partial \mathbf{y}}, \quad \Lambda_n F = \sin \mathbf{y} \frac{\mathbb{I}F}{\mathbb{I}h} + \frac{\cos \mathbf{y}}{h} \frac{\partial F}{\partial \mathbf{y}}, \quad (8)$$

Equations (7) and (8) are similar to the ones in the earlier asymptotic analysis for the laminated composites with open holes [35]. Therefore, we can utilize a similar approach to obtain solutions for the singular analysis. The Navier equations of equilibrium for a given ply can be written as

$$(\mathbf{A}\Lambda_t\Lambda_t + \mathbf{B}\Lambda_n\Lambda_t + \mathbf{C}\Lambda_n\Lambda_n) \begin{Bmatrix} u_x \\ u_y \\ u_z \end{Bmatrix} = 0, \quad (9)$$

where the symmetric square (3 x 3) matrices, \mathbf{A} , \mathbf{B} , and \mathbf{C} , are expressed as follows:

$$\mathbf{A} = \begin{bmatrix} Q_{11} & Q_{16} & 0 \\ & Q_{66} & 0 \\ \text{symm} & & Q_{55} \end{bmatrix}^{(s)}, \quad \mathbf{B} = \begin{bmatrix} 0 & 0 & Q_{13} + Q_{55} \\ & 0 & Q_{36} + Q_{45} \\ \text{symm} & & 0 \end{bmatrix}^{(s)}, \quad \mathbf{C} = \begin{bmatrix} Q_{55} & Q_{45} & 0 \\ & Q_{44} & 0 \\ \text{symm} & & Q_{33} \end{bmatrix}^{(s)}, \quad (10)$$

where $Q_{ij}^{(s)}$ are off-axis stiffness coefficients for the s -th ply. A contracted notation is used for the stiffness and stress components if not identified otherwise, so that indices $(i, j = 1, \Lambda, 6)$ correspond to xx, yy, zz, yz, xz, xy , respectively.

According to the earlier asymptotic analysis [35], a homogeneous solution of the displacement field of the Navier equations in Eq. (9) was found in the form of

$$u_i^{(s)} = \mathbf{h}^I \sum_{k=1}^6 f_k^{(s)} (\sin \mathbf{y} + \mathbf{m}_k^{(s)} \cos \mathbf{y})^I d_{ki}^{(s)}, \quad i = 1, 2, 3, \quad (11)$$

where $f_k^{(s)}$ and \mathbf{I} are arbitrary complex constants to be determined from the boundary conditions. Characteristic values, $\mathbf{m}_k^{(s)}$, are eigenvalues of the following sixth-order polynomial characteristic equation,

$$\det[\mathbf{A}\mathbf{m}_k^2 + \mathbf{B}\mathbf{m}_k + \mathbf{C}] = 0 \quad (12)$$

and $d_{ki}^{(s)}$ are eigenvectors of the following characteristic matrix,

$$(\mathbf{A}\mathbf{m}_k^2 + \mathbf{B}\mathbf{m}_k + \mathbf{C}) \begin{Bmatrix} d_{k1} \\ d_{k2} \\ d_{k3} \end{Bmatrix} = 0. \quad (13)$$

It will be understood that coefficients \mathbf{m}_k and vectors d_{ki} are constant for each ply; therefore, the superscript s is subsequently omitted unless needed for clarity.

For orthotropic materials Eq. (12) yields six different roots such that $\mathbf{m}_k = -\mathbf{m}_{k+3}$, $k = 1, 2, 3$.

For isotropic materials there are only two different roots, $\pm\sqrt{-1}$ of triple multiplicity. Since the solution in Eq. (11) is valid only if all characteristic roots are distinct, the isotropic material is treated as a slightly orthotropic material by perturbing the elastic properties, E and \mathbf{n} , with a coefficient of anisotropy ($t = 10^{-7}$) such that

$$\begin{aligned}
E_1 &= (1+t)E, \quad E_2 = E_3 = E, \\
\nu_{12} &= \nu_{13} = \nu, \quad \nu_{23} = (1+10t)\nu, \\
G_{23} &= \frac{E}{2(1+\nu_{23})}, \quad G_{12} = G_{13} = (1+t)G_{23}
\end{aligned} \tag{14}$$

The stress components in the global (xyz) coordinates are expressed as

$$\mathbf{s}_{ij} = C_{ijkl} \mathbf{e}_{kl} = \frac{C_{ijkl}}{2} \left(\frac{\partial u_k}{\partial x_l} + \frac{\partial u_l}{\partial x_k} \right) \tag{15}$$

or in the contracted notation,

$$\mathbf{s}_i = Q_{ij} \mathbf{e}_j, \tag{16}$$

where the stress components \mathbf{s}_i correspond to $\mathbf{s}_{xx}, \mathbf{s}_{yy}, \mathbf{s}_{zz}, \mathbf{s}_{yz}, \mathbf{s}_{xz}, \mathbf{s}_{xy}$, and the strain components \mathbf{e}_i correspond to $\mathbf{e}_{xx}, \mathbf{e}_{yy}, \mathbf{e}_{zz}, 2\mathbf{e}_{yz}, 2\mathbf{e}_{xz}, 2\mathbf{e}_{xy}$ for $i=1, \dots, 6$, respectively. By substituting Eq. (11) into Eq. (15), one can obtain the global stress components as follows:

$$\begin{aligned}
\mathbf{s}_i &= I h^{l-1} \sum_{k=1}^6 f_k (\sin \mathbf{y} + \mathbf{m}_k \cos \mathbf{y})^{l-1} [\mathbf{m}_k (Q_{i1} d_{k1} + Q_{i6} d_{k2}) + Q_{i3} d_{k3}], \quad i=1, 2, 3, 6 \\
\mathbf{s}_i &= I h^{l-1} \sum_{k=1}^6 f_k (\sin \mathbf{y} + \mathbf{m}_k \cos \mathbf{y})^{l-1} [Q_{i5} d_{k1} + Q_{i4} d_{k2} + \mathbf{m}_k Q_{i5} d_{k3}], \quad i=4, 5
\end{aligned} \tag{17}$$

The power I and the coefficients f_k are to be determined from the boundary conditions at the interface between the two plies and at the free edges. The displacement and traction continuity conditions at the interface between the s -th and $(s+1)$ -th plies yield

$$\begin{aligned}
u_x^{(s)} &= u_x^{(s+1)}, \quad u_y^{(s)} = u_y^{(s+1)}, \quad u_z^{(s)} = u_z^{(s+1)}, \\
\mathbf{s}_{zz}^{(s)} &= \mathbf{s}_{zz}^{(s+1)}, \quad \mathbf{s}_{xz}^{(s)} = \mathbf{s}_{xz}^{(s+1)}, \quad \mathbf{s}_{yz}^{(s)} = \mathbf{s}_{yz}^{(s+1)} \quad \text{at } \mathbf{y} = 0,
\end{aligned} \tag{18}$$

and the traction-free boundary conditions at the slanted free edges in s -th and $(s+1)$ -th plies yield

$$\begin{aligned}
\mathbf{s}_{rt}^{(s)} &= \mathbf{s}_{st}^{(s)} = \mathbf{s}_{tt}^{(s)} \quad \text{at } \mathbf{y} = -\frac{\mathbf{p}}{2} + \mathbf{f} \\
\mathbf{s}_{rt}^{(s+1)} &= \mathbf{s}_{st}^{(s+1)} = \mathbf{s}_{tt}^{(s+1)} \quad \text{at } \mathbf{y} = \frac{\mathbf{p}}{2} + \mathbf{f}.
\end{aligned} \tag{19}$$

The stress components, $\{\mathbf{s}\}_{rst}$, in the local coordinates (rst) are obtained from the global stress components, $\{\mathbf{s}\}_{xyz}$, as follows:

$$\{\mathbf{s}\}_{rst} = \begin{bmatrix} m_1^2 & 0 & n_1^2 & 0 & 2m_1n_1 & 0 \\ 0 & 1 & 0 & 0 & 0 & 0 \\ n_1^2 & 0 & m_1^2 & 0 & -2m_1n_1 & 0 \\ 0 & 0 & 0 & m_1 & 0 & -n_1 \\ -m_1n_1 & 0 & m_1n_1 & 0 & m_1^2 - n_1^2 & 0 \\ 0 & 0 & 0 & n_1 & 0 & m_1 \end{bmatrix} \{\mathbf{s}\}_{xyz}, \tag{20}$$

Equations (18) and (19) form a homogeneous system of 12 linear equations with 12 unknowns, $f_k^{(s)}$ and $f_k^{(s+1)}$, $k = 1, \Lambda, 6$, such that

$$\begin{aligned}
\mathbf{M} \cdot \mathbf{f} &= \mathbf{0} \\
\mathbf{f} &= \{f_1^{(s)}, \Lambda, f_6^{(s)}, f_1^{(s+1)}, \Lambda, f_6^{(s+1)}\}^T,
\end{aligned} \tag{21}$$

where \mathbf{M} is a coefficient matrix of $f_k^{(s)}$ and $f_k^{(s+1)}$. Nontrivial solutions of Eq. (21) are obtained by requiring the determinant of the coefficient matrix (\mathbf{M}) to be equal to zero. The determinant of the system of equations becomes a transcendental equation, which yields an infinite number of roots for the parameter \mathbf{I} . Note that only roots with $0 < \text{Re}(\mathbf{I}) < 1$ provide unbounded stresses, which dominate the solution for $\mathbf{h} \ll 1$. The roots for the determinant were found numerically using the Secant method. Two initial guesses of \mathbf{I} were used to obtain the determinants, $g(\mathbf{I}_0)$ and $g(\mathbf{I}_1)$. A new root (\mathbf{I}_2) was then refined by

$$\mathbf{I}_2 = \mathbf{I}_1 - \frac{g(\mathbf{I}_1)(\mathbf{I}_1 - \mathbf{I}_0)}{g(\mathbf{I}_1) - g(\mathbf{I}_0)}. \tag{22}$$

After setting \mathbf{I}_1 to \mathbf{I}_0 and \mathbf{I}_2 to \mathbf{I}_1 , the procedure repeated until $\mathbf{I}_2 \approx \mathbf{I}_1$. For a given root of \mathbf{I} , the coefficients $f_k^{(s)}$ and $f_k^{(s+1)}$, $k = 1, \Lambda, 6$, can only be obtained with an arbitrary multiplicative factor. Therefore, one of the coefficients in \mathbf{f} was set to one.

With the solution of Eq. (21), the stress components in Eq. (15) can be rewritten as

$$\mathbf{s}_i = \sum_{j=1}^{\infty} K_j \mathbf{h}^{I_j-1} \bar{\mathbf{s}}_i(\mathbf{I}_j, \mathbf{y}), \quad i = 1, \Lambda, 6, \quad (23)$$

where $\bar{\mathbf{s}}_i(\mathbf{I}_j, \mathbf{y})$ are determined by the asymptotic solution and normalized so that

$\bar{\mathbf{s}}_3(\mathbf{I}_j, -\mathbf{p}/2 + \mathbf{f}) = 1$. Even though the stress terms in Eq. (23) do not provide the full-field solution of the 3-D problem, the singular stress terms are expected to correlate with the full-field solution for $\mathbf{h} \ll 1$. The constants (K_j) are only given by comparing the asymptotic solution with the full-field numerical solution for $\mathbf{h} \ll 1$. As stated earlier, the singular stresses are obtained only for roots with $0 < \text{Re}(\mathbf{I}) < 1$. However, when the constants were determined by the full-field solution, we also have to consider the roots with $\text{Re}(\mathbf{I}) > 1$ as long as the roots are close to one, because of weak character of the singularity [35]. With a finite number of the roots (\mathbf{I}_j , $j = 1, \Lambda, n$), which only provide meaningful magnitudes of the stress components for $\mathbf{h} \ll 1$, Eq. (23) is rewritten as

$$\mathbf{s}_i = F_i + \sum_{j=1}^n K_j \mathbf{h}^{I_j-1} \bar{\mathbf{s}}_i(\mathbf{I}_j, \mathbf{y}), \quad i = 1, \Lambda, 6, \quad (24)$$

where the additives (F_i) are also given by comparing the asymptotic solution with the full-field numerical solution.

6.2 FULL-FIELD NUMERICAL CALCULATION

The full-field numerical analysis was performed with a laminated composite plate of orthotropic plies having a slanted edge, as shown in Figure 31. The slanted angle from the global z -axis was denoted as θ . The thickness of each ply was denoted as h , and other dimensions in x - and y -directions, when measured along the interface between the plies, were denoted as L_x and L_y , respectively. Total thickness of the laminated plate is denoted as H . The plate was loaded with a constant displacement (u^o) in the y -direction under the following boundary conditions:

$$\begin{aligned} u_y(x, 0, z) &= 0, \quad u_y(x, L_y, z) = u^o \\ u_x(L_x, y, z) &= u_z(x, y, 0) = u_z(x, y, H) = 0. \end{aligned} \quad (25)$$

Zero values of u_x and u_z displacements restrained the movement of the planes in their perpendicular directions, which simulated the plane of symmetry.

The full-field 3-D solution was obtained based on spline approximation of displacement and interlaminar stress components in curvilinear coordinates. The stress distributions recovered near the free edge and interface between plies were to match the closed-form asymptotic solution results. The B-SAM is a previously developed computer program for the 3-D analysis of anisotropic laminated composite structures, including bonded joints and bolted joints. The B-SAM has the advantage of an efficient modeling and solution scheme through the use of overlapping B-spline-based shape functions [36]. Furthermore, the spline approximation eliminates artificial discontinuities of stress and strain components within homogeneous domains.

The overlapping nature of the approximation functions keeps a minimal bandwidth profile in the stiffness matrix of the system of equations. While the conventional FE

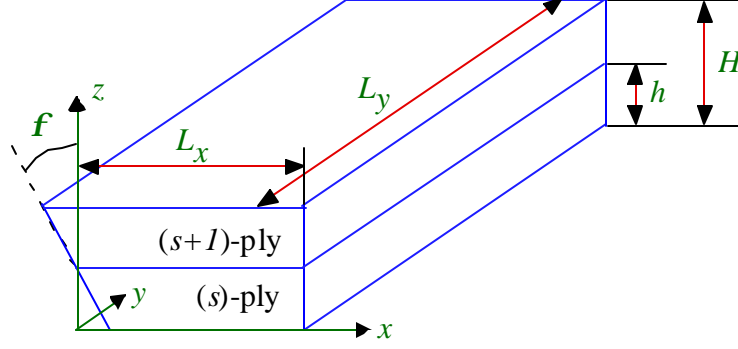


Figure 31. Laminated Composite Plate with a Slanted Edge.

(p -element) has C^0 continuity, m -th order spline functions have $C^{(m-1)}$ continuity, which yields continuous derivatives up to the $(m-1)$ -th order. Therefore, stress and strain fields as well as the displacements are evaluated continuously within the homogeneous domain (subregions) with the spline method for $m \geq 2$. The homogeneous domain discretized with n subdivisions in one direction needs $(n+m)$ overlapping m -th order spline functions. Figure 32 shows an example of cubic splines overlapped on seven subdivisions. Construction of a set of the spline functions was achieved with a recursive formula developed earlier [35].

The B-SAM analysis needs to define the given homogeneous domain in \mathbf{x} -space with continuous functions in \mathbf{x} -space defined by a unit cube, so that any variables and their derivatives were determined from the functions continuously within the domain. Figure 33 shows a cross section with slanted edges on the xz -plane mapped to the \mathbf{x} -domain.

The coordinates in the \mathbf{x} -domain were correlated with the ones in the x -domain as follows:

$$x = \sum_{a=1}^4 N_a(\mathbf{x}) x_a, \quad y = L_y \mathbf{x}_y, \quad z = \sum_{a=1}^4 N_a(\mathbf{x}) z_a, \quad (26)$$

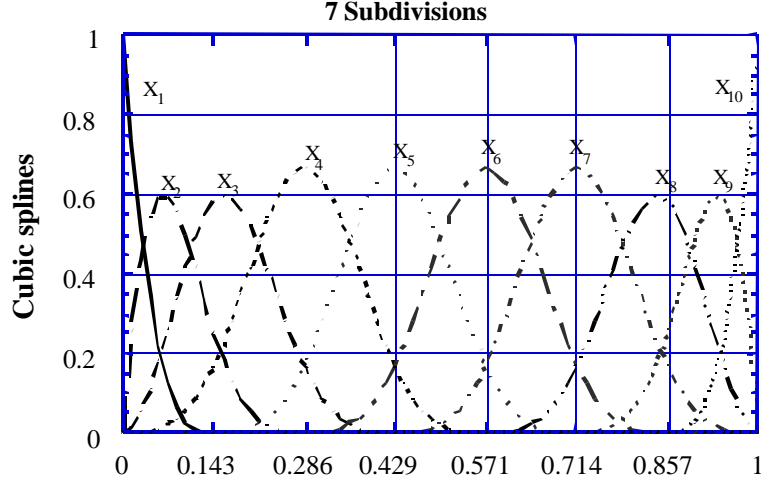


Figure 32. Overlapping Cubic B-Spline Functions with Seven Subdivisions.

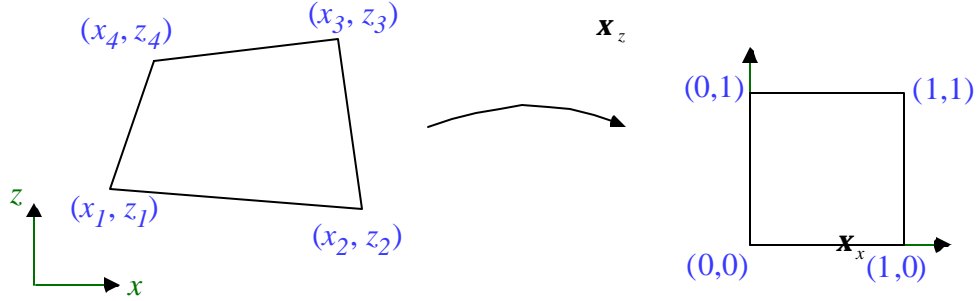


Figure 33. Mapping of Homogeneous Domain in \mathcal{X} -Space to a Unit Cube in \mathcal{X} -Domain.

where

$$N_1 = (1 - \mathbf{x}_x)(1 - \mathbf{x}_z), \quad N_2 = \mathbf{x}_x(1 - \mathbf{x}_z), \quad N_3 = \mathbf{x}_x \mathbf{x}_z, \quad N_4 = (1 - \mathbf{x}_x) \mathbf{x}_z. \quad (27)$$

Note that Eqs. (26) and (27) are valid only for the geometry with a uniform cross section along the y -axis. The slanted geometry in different planes should be used with a different formula.

The variational procedure in the B-SAM yielded a system of equations for spline approximation coefficients of the displacement components. Strains and stresses were then directly calculated with the derivatives of the displacement approximation coefficients. All stress components presented in this section were normalized with an average stress (\mathbf{s}_o). The

average stress was calculated with the stress components in the loading direction on the cross section perpendicular to the loading direction, such that

$$\mathbf{s}_o = \frac{\int \int_z \mathbf{s}_{yy}(x,0,z) dA}{A} . \quad (28)$$

Quadratic or cubic splines used for displacement approximation were continuously differentiable at all points in the ply. Therefore, all strain and stress components were continuous inside each ply. Meanwhile, the interlaminar strains and stresses calculated in adjacent plies may be discontinuous at their common interface. However, the interlaminar stress components at the adjacent plies must be of equal value with each other to satisfy the traction-continuity condition at the interface. This interlaminar stress continuity condition as well as the zero traction condition at the slanted free edge will be investigated by comparing with the analytic asymptotic analysis in this work.

The accuracy of the numerical solution to satisfy the conditions described above was mesh dependent. Different subdivisions were tried to determine a reasonably refined mesh for the given geometry and the material properties. Nonuniform mesh was used to concentrate the subdivisions to the singular point at the intersection of the free edge and the interface between the plies. The number of subdivisions in a direction in the domain was denoted as n . The domain was subdivided into $(n+1)$ points $(p_i, i = 0, \Lambda, n)$ in that direction. A space ratio (q) of the nonuniform mesh was given such that,

$$q = \frac{p_{i+1} - p_i}{p_i - p_{i-1}}, \quad i = 1, \Lambda, (n-1) . \quad (29)$$

6.3 RESULTS

A symmetric AS4/3501-6 laminated composite plate with a lay-up of $[45/-45]_s$ was considered for the asymptotic and numerical analysis. The dimensions of the plates are $L_y = 10$ mm and $t = 0.125$ mm, and the material properties of the AS4/3501-6 ply are listed in Table 7.

Table 7
Material Properties of AS4/3501-6

E_x [GPa]	$E_y = E_z$ [GPa]	$\nu_{xy} = \nu_{xz}$	ν_{yz}	$G_{xy} = G_{xz}$ [GPa]	G_{yz} [GPa]
139	10.34	0.3	0.55	5.52	3.31

The asymptotic analysis was first performed at the $[45/-45]$ interface with various slanted angles (θ). The characteristic values (\mathbf{m}_k) in Eq. (13) were $\pm 0.2827 i$, $\pm 0.8581 i$ and $\pm 1.209 i$ for both 45 and -45 plies. The slanted angles varied from 0 to 90 degrees in one-degree increments. As stated earlier, the roots (\mathbf{I}) were found in the range of $0 < \text{Re}(\mathbf{I}) < 1$ and $\text{Re}(\mathbf{I}) > 1$ as long as the roots are close to one. The power of singularity is $1 - \mathbf{I}$. Distribution of real and imaginary parts of the roots with respect to the slanted angle is plotted in Figure 34 with solid and dotted lines, respectively. The roots were pure real numbers with $0^\circ \leq \theta \leq 2^\circ$ and $38^\circ \leq \theta \leq 90^\circ$, while nonzero imaginary parts of the roots existed with $3^\circ \leq \theta \leq 37^\circ$. When the root was a complex number with the non-zero imaginary part, the second root was the conjugate of the roots. The power of singularity increased significantly, as the slanted angle increased to be greater than 45 degrees.

The full-field numerical analysis used the mesh in the homogeneous domains with the following number of subdivisions (m) and the space ratio (q):

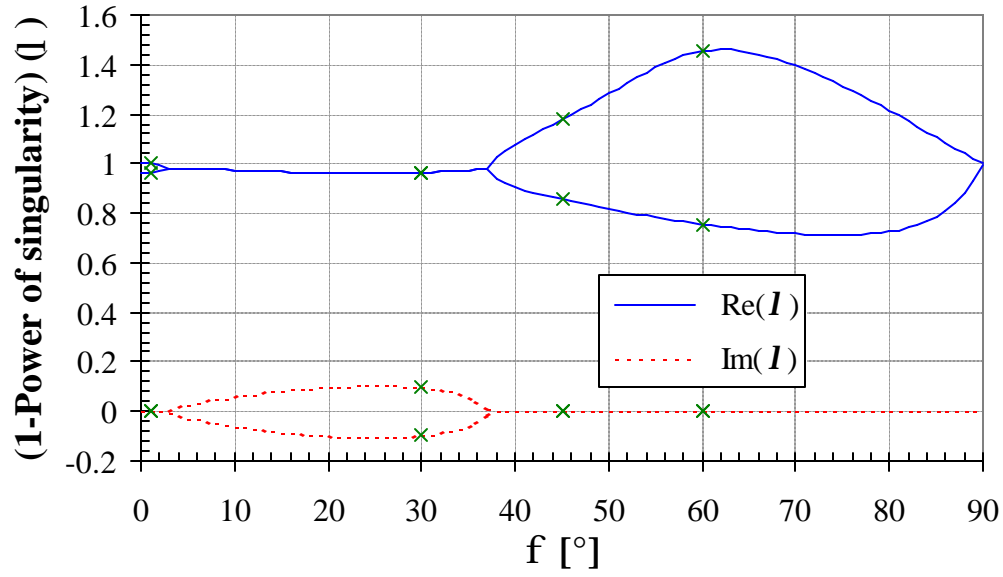


Figure 34. Distribution of Real and Imaginary Parts of the Roots with Various Slanted Angles.

1. $m = 24, q = 1.2$ in the x -direction for both plies.
2. $m = 6, q = 0.5$ in the y -direction for both plies.
3. $m = 10, q = 2.0$ in the z -direction for lower -45° ply.
4. $m = 10, q = 0.5$ in the z -direction for upper 45° ply.

The multiplicative factors (K_j) and the additives (F_i) in Eq. (24) were determined by comparing the stress components from the asymptotic solution with ones from the full-field numerical calculation. In later figures, the stress components from numerical and asymptotic solutions will be plotted with solid and dotted lines, respectively. The stress results were compared in two different ways:

1. Stress distributions in global xyz -axes along straight lines parallel to the interface line between the plies: The distance between two lines was represented with a dimensionless parameter, $z^* = (z - z^{(s)})/h$, where z and $z^{(s)}$ are the coordinates of parallel and interface lines, respectively, and h is the thickness of the ply. The

distance was chosen at $z^* = \pm 0$, $z^* = \pm 0.02$ and $z^* = \pm 0.04$, where the positive values were for the lines in the upper 45 ply, and negative for the lines in the lower -45 ply.

2. Stress distributions in local rst -axes with $y = f$ along contours of constant radii with the center at the singular point: The radius of the contour was denoted as $r = h L_x$. The radius was chosen at $h = 0.02$, $h = 0.04$ and $h = 0.06$.

Four slanted angles were selected for representing distinguished cases as appeared in Figure 34, such that:

1. $f = 1^\circ$: Roots are two pure real numbers. Both roots are very close to and less than one. This case should be nearly identical to the problem with $f = 0^\circ$ [35].
2. $f = 30^\circ$: Roots are complex conjugated numbers. The magnitude of the complex root is very close to one.
3. $f = 45^\circ$: Roots are two pure real numbers. Both roots are fairly close to one, and one of the roots was greater than one.
4. $f = 60^\circ$: Roots are two pure real numbers. Both roots are far from one, and one of the roots was greater than one.

Note that the roots in Figure 34 are the only roots whose magnitudes are near one, whether the roots are pure real numbers or not.

$$\underline{f = 1^\circ}$$

Two roots found by the asymptotic analysis were $I_1 = 0.9626$ and $I_2 = 0.9987$. The second root was practically equal to one, which can be considered as a nonsingular root. Figure 35 shows distributions of amplitudes of the singular stress components in the global xyz -axes as

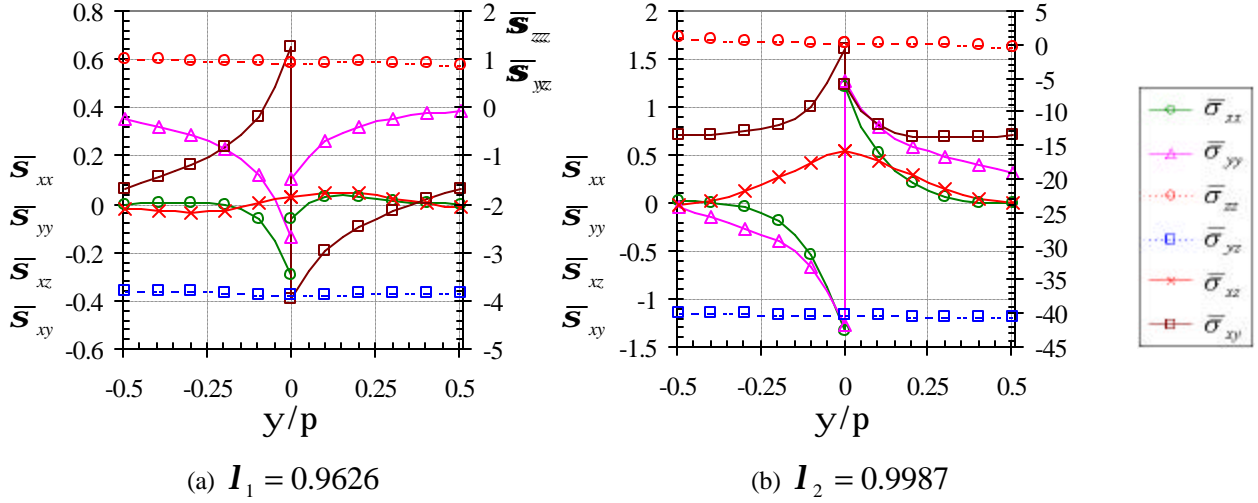
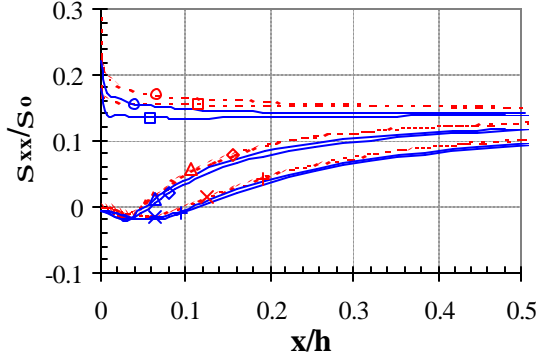


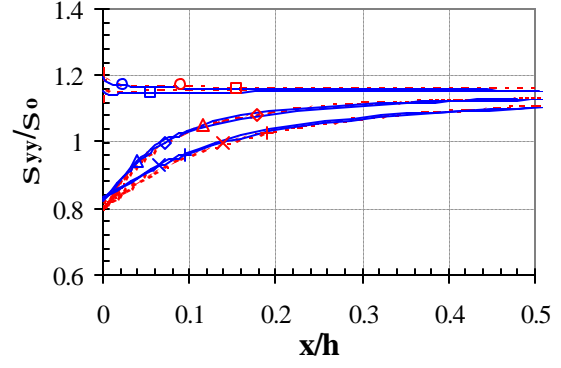
Figure 35. Distribution of Magnitudes of Singular Stress Components with Two Roots for $f = 1^\circ$.

functions of y for the two roots. Stress components \bar{S}_{zz} and \bar{S}_{yz} are nearly constant for both roots. The interlaminar stress components (\bar{S}_{zz} , \bar{S}_{yz} and \bar{S}_{xz}) were continuous at the ply interface ($y = 0$), which satisfied the traction continuity boundary condition in Eq. (18). With the slightly slanted angle of the free edge, all stress components became nonsymmetric with respect to $y = 0$, which were otherwise symmetric if $f = 0^\circ$ [35].

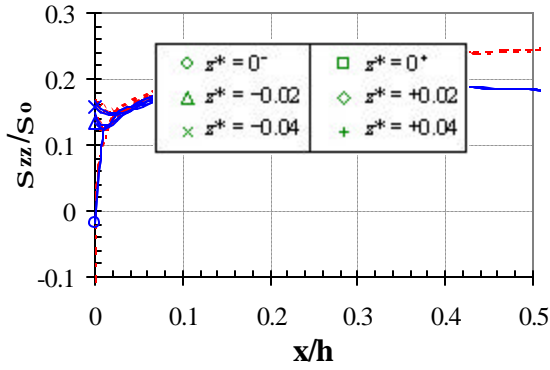
Figures 36 and 37 show stress distribution by asymptotic and numerical analyses in the global xyz -axes and the local rst -axes. The comparisons in both figures were made with the same multiplicative coefficients, $K_1 = -0.80$ and $K_2 = 0.08$, corresponding to the first and the second power of singularities. As stated earlier, the multiplicative coefficient of the second root was much less than that of the first root, since the second root, which was nearly one, contributed minimally to the asymptotic stress components. The additives in Figure 36 were $F_2 = 1.15$, $F_3 = 1.03$, $F_4 = 0.02$, $F_5 = -0.019$ and $F_1 = F_6 = 0$, and in Figure 37 were $F_2 = 1.15$,



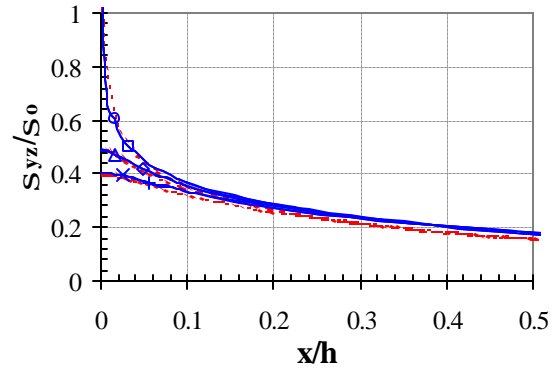
(a) In-plane normal stress (\mathbf{S}_{xx})



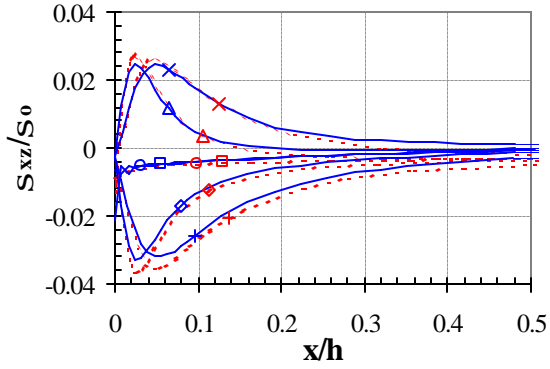
(b) In-plane normal stress (\mathbf{S}_{yy})



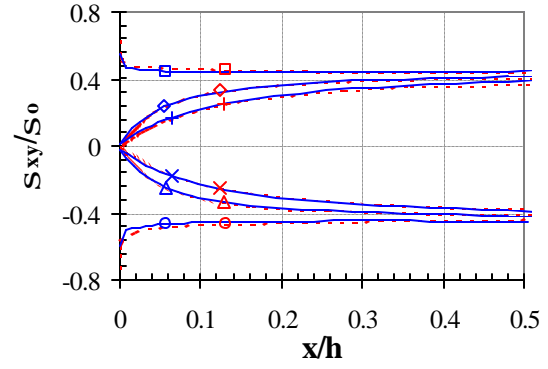
(c) Interlaminar normal stress (\mathbf{S}_{zz})



(d) Interlaminar shear stress (\mathbf{S}_{yz})

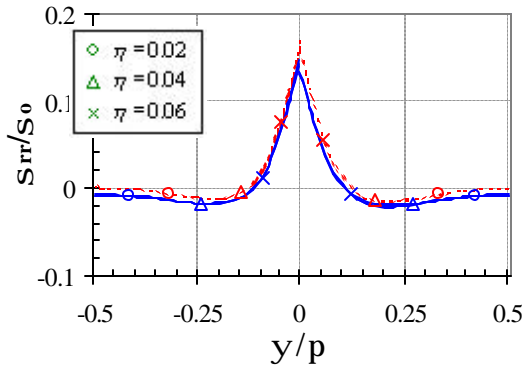


(e) Interlaminar shear stress (\mathbf{S}_{xz})

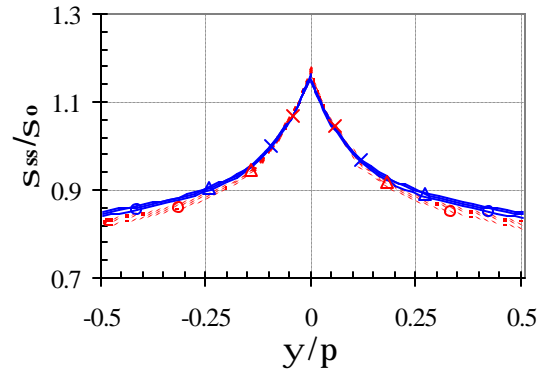


(f) In-plane shear stress (\mathbf{S}_{xy})

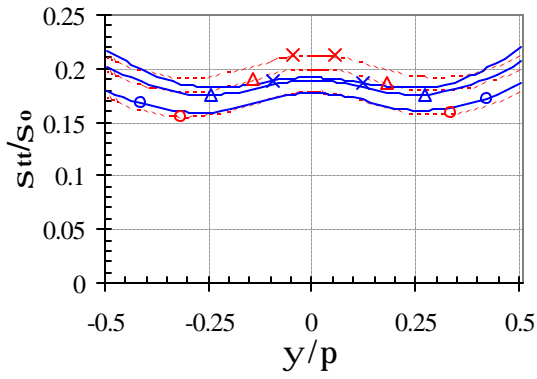
Figure 36. Stress Distribution in Global xyz -Axes by Asymptotic and Numerical Analyses near the Singular Point Along Straight Lines Parallel to the Interface between Two Plies.



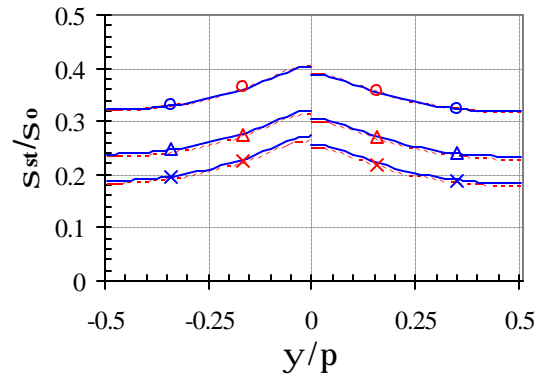
(a) In-plane normal stress (\mathbf{S}_{rr})



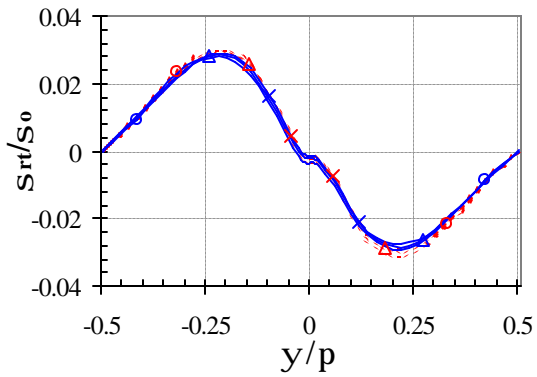
(b) In-plane normal stress (\mathbf{S}_{ss})



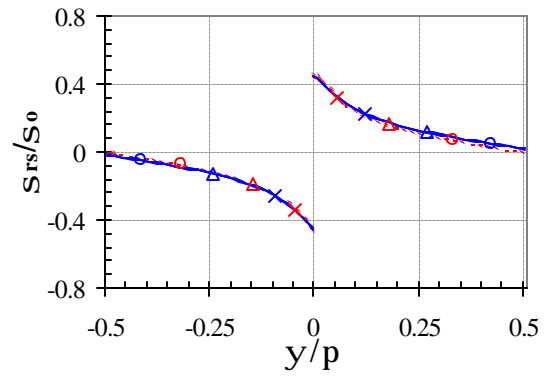
(c) Interlaminar normal stress (\mathbf{S}_{tt})



(d) Interlaminar shear stress (\mathbf{S}_{st})



(e) Interlaminar shear stress (\mathbf{S}_{rt})



(f) In-plane shear stress (\mathbf{S}_{rs})

Figure 37. Stress Distribution in Local rst -Axes with $y = 1^\circ$ by Asymptotic and Numerical Analyses Along Contours of Constant Radii with the Center at the Singular Point.

$F_3 = 1.02$, $F_4 = 0.03$ and $F_1 = F_5 = F_6 = 0$. Note that the same additives were used for both 45° and -45° plies.

In Figure 36, with the range of $x/h > 0.01$, excellent agreement was observed between the full-field numerical solution and two-term asymptotic one for all stresses with one set of the multiplicative factors and the additives. One exception was the interlaminar normal stress (\mathbf{s}_{zz}), which showed a rapid increase in the asymptotic solution as the point moved away from the singular point. All stress components grew infinitely on approaching the singular point along the interface line ($z^* = \pm 0$) in the asymptotic solution, but yielded finite values in the numerical solution. Three stress components ($\bar{\mathbf{s}}_{xx}$, $\bar{\mathbf{s}}_{xz}$ and $\bar{\mathbf{s}}_{xy}$) from both analyses were nearly equal to zero at the free edge ($\mathbf{y} = \pm \mathbf{p}/2 + \mathbf{f}$) if the parallel lines were not along the interface. Note that these stresses in the asymptotic solution were identically zero with the nonslanted edge problem ($\mathbf{f} = 0^\circ$).

In Figure 37, three stress components ($\bar{\mathbf{s}}_{rr}$, $\bar{\mathbf{s}}_{rs}$ and $\bar{\mathbf{s}}_{rt}$) from the asymptotic analyses were identically zero at the free edge ($\mathbf{y} = \pm \mathbf{p}/2 + \mathbf{f}$), which satisfied the traction-free boundary condition in Eq. (19), while the numerical solution yielded nearly zero stresses. Excellent agreement was also observed between the full-field numerical solution and two-term asymptotic one for all stresses along the three contours. One exception was again the interlaminar normal stress (\mathbf{s}_{tt}), which showed more discrepancy as the radius of the contour increased. This bigger discrepancy with the increase of the radius is consistent with the observation made in Figure 36, since the stress increased rapidly in the asymptotic solution as the point moved away from the singular point.

$$\underline{f = 30^\circ}$$

No real root was found near one with this slanted angle. Instead, a pair of the conjugated complex roots was only found by the asymptotic analysis with $I_1, I_2 = 0.9646 \pm 0.0968 i$. The complex roots resulted in complex numbers of the magnitudes of stress components (\bar{S}_i) and of the multiplicative coefficients (K_j). Note that the conjugated roots yielded the same distribution of real and imaginary parts of \bar{S}_i , and, therefore, only one of the roots was considered in the asymptotic calculation. The asymptotic stress components in Eq. (24) can be rewritten for the complex root as

$$\begin{aligned} \mathbf{s}_i &= F_i + K_1 \mathbf{h}^{I_1-1} \bar{S}_i(I_1, \mathbf{y}), \quad i=1, \Lambda, 6 \\ &= F_i + K_1 \mathbf{h}^{\text{Re}(I_1)-1} [\{\text{Re}(\bar{S}_i) \cos \mathbf{w} - \text{Im}(\bar{S}_i) \sin \mathbf{w}\} + i \{\text{Re}(\bar{S}_i) \sin \mathbf{w} + \text{Im}(\bar{S}_i) \cos \mathbf{w}\}], \end{aligned} \quad (30)$$

where $\mathbf{w} = \text{Im}(I_1) \ln|\mathbf{h}|$. With the complex number of K_j , Eq. (30) becomes

$$\begin{aligned} \mathbf{s}_i &= F_i + \bar{K}_1 \mathbf{h}^{\text{Re}(I_1)-1} \{\text{Re}(\bar{S}_i) \cos \mathbf{w} - \text{Im}(\bar{S}_i) \sin \mathbf{w}\} \\ &\quad + \bar{K}_2 \mathbf{h}^{\text{Re}(I_1)-1} \{\text{Re}(\bar{S}_i) \sin \mathbf{w} + \text{Im}(\bar{S}_i) \cos \mathbf{w}\}, \quad i=1, \Lambda, 6, \end{aligned} \quad (31)$$

where \bar{K}_1 and \bar{K}_2 are pure real numbers. Therefore, the complex roots also led to the two-term asymptotic solution.

Figure 38 shows distributions of amplitudes of real and imaginary parts of the singular stress components in the global xyz -axes as functions of \mathbf{y} for the complex root. The three interlaminar stress components are nearly constant in the real part, while no constant component is found in the imaginary part. The traction continuity boundary conditions were satisfied at the ply interface ($\mathbf{y} = 0$) in both parts.

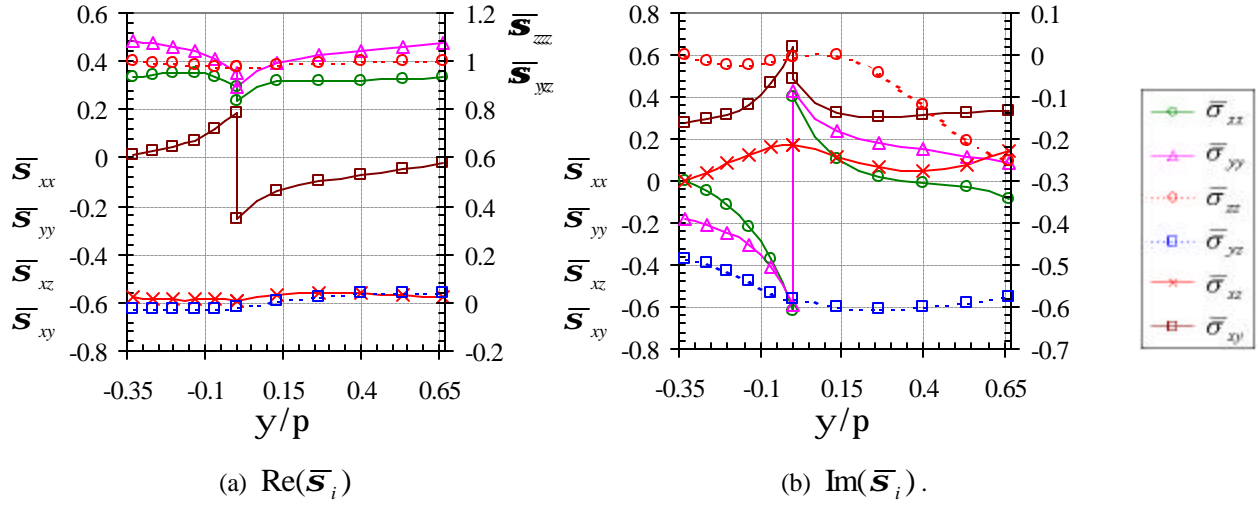
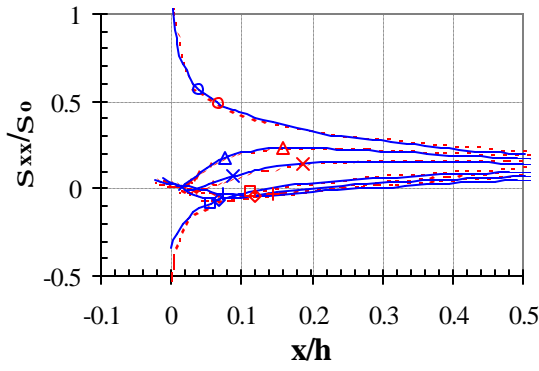


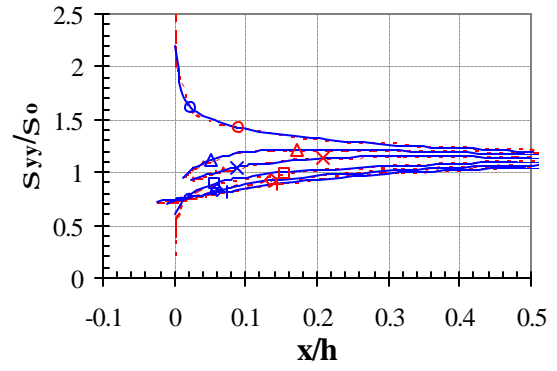
Figure 38. Distribution of Magnitudes of Singular Stress Components with a Complex Root, $I_1 = 0.9646 + 0.0968i$, for $f = 60^\circ$.

Figures 39 and 40 show stress distribution by asymptotic and numerical analyses in the global xyz -axes and the local rst -axes. The comparisons in both figures were made with the same multiplicative coefficients, $K_1 = -2$ and $K_2 = 0.2$ corresponding to the first and the second power of singularities. The additives in Figure 39 were $F_1 = -0.72$, $F_2 = 0.45$, $F_3 = -0.23$, $F_4 = -0.04$, $F_5 = 0.4$, and $F_6 = 0$, while in Figure 40 were $F_2 = 0.44$, $F_3 = -0.95$, $F_4 = -0.03$, and $F_1 = F_5 = F_6 = 0$.

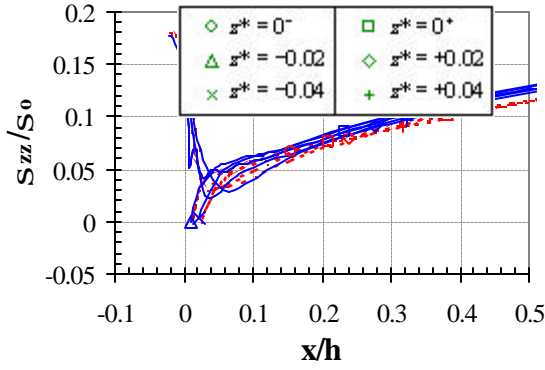
In Figure 39, with the range of $x/h > 0.01$, excellent agreement was observed between the full-field numerical solution and two-term asymptotic one for all stresses with one set of the multiplicative factors and the additives. One exception was the interlaminar normal stress (\mathbf{s}_{zz}), which showed a rapid increase in the asymptotic solution as the point moved away from the singular point. All stress components grew infinitely on approaching the singular point along the interface line ($z^* = \pm 0$) in the asymptotic solution, but yielded finite values in the numerical solution.



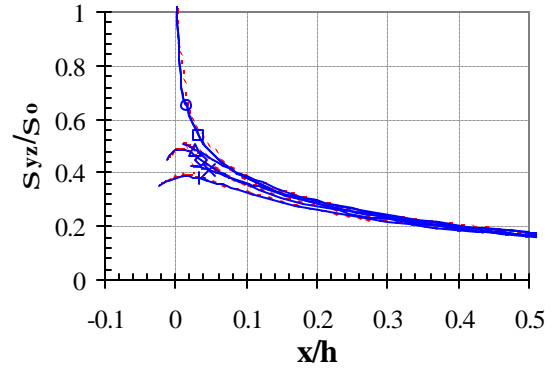
(a) In-plane normal stress (\mathbf{S}_{xx})



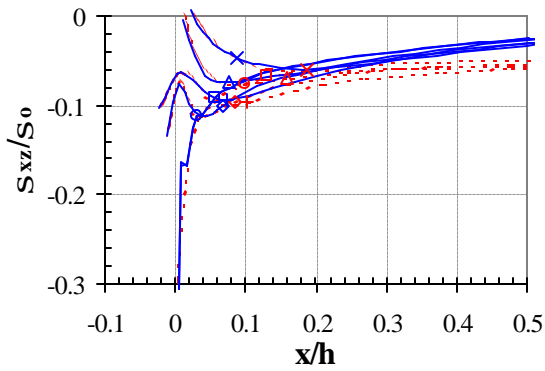
(b) In-plane normal stress (\mathbf{S}_{yy})



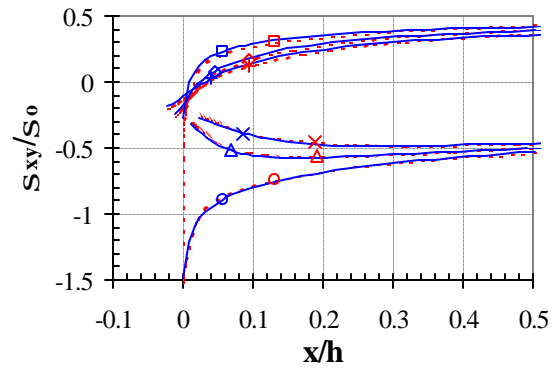
(c) Interlaminar normal stress (\mathbf{S}_{zz})



(d) Interlaminar shear stress (\mathbf{S}_{yz})

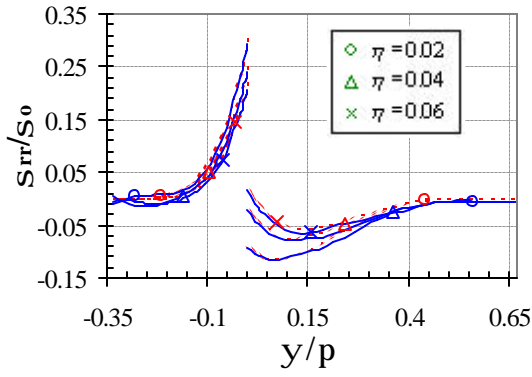


(e) Interlaminar shear stress (\mathbf{S}_{xz})

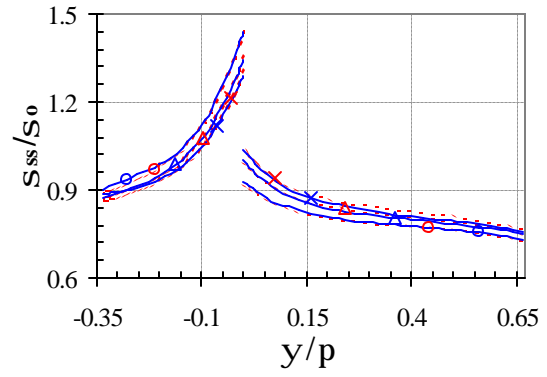


(f) In-plane shear stress (\mathbf{S}_{xy})

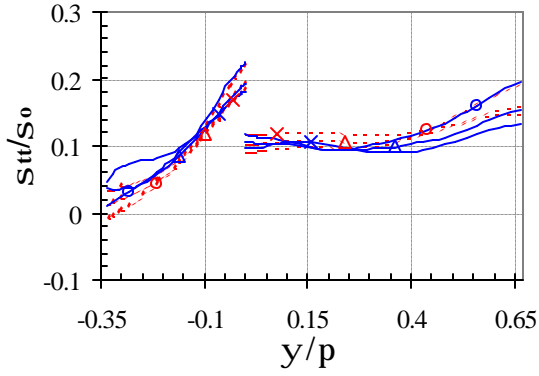
Figure 39. Stress Distribution in Global xyz -Axes by Asymptotic and Numerical Analyses near the Singular Point Along Straight Lines Parallel to the Interface between Two Plies.



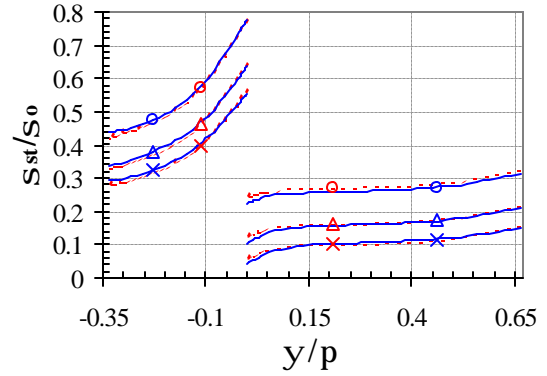
(a) In-plane normal stress (\mathbf{S}_{rr})



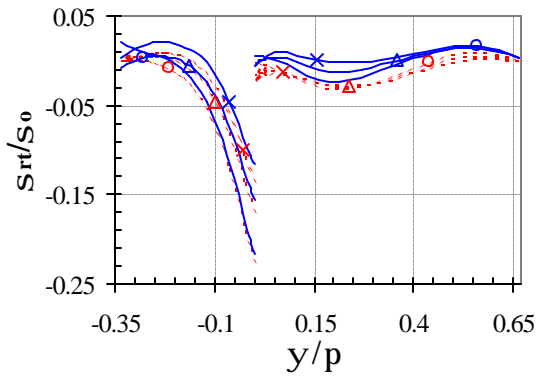
(b) In-plane normal stress (\mathbf{S}_{ss})



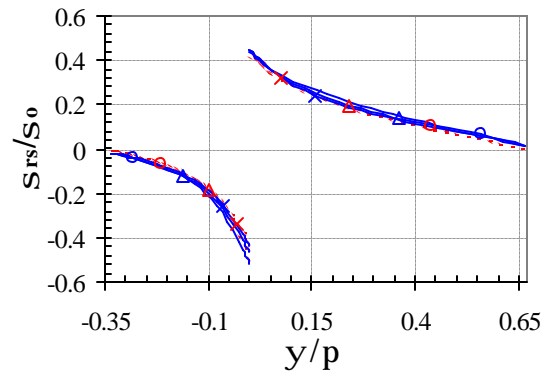
(c) Interlaminar normal stress (\mathbf{S}_{tt})



(d) Interlaminar shear stress (\mathbf{S}_{st})



(e) Interlaminar shear stress (\mathbf{S}_{rt})



(f) In-plane shear stress (\mathbf{S}_{rs})

Figure 40. Stress Distribution in Local rst -Axes with $f = 30^\circ$ by Asymptotic and Numerical Analyses Along Contours of Constant Radii with the Center at the Singular Point.

In Figure 40 three stress components (\bar{s}_{rr} , \bar{s}_{rs} and \bar{s}_{rt}) from the asymptotic analyses were identically zero at the free edge ($y = \pm p/2 + f$), which satisfied the traction-free boundary condition in Eq. (19), while the numerical solution yielded nearly zero stresses. Excellent agreement was also observed between the full-field numerical solution and two-term asymptotic one for all stresses along the three contours. One exception was again the interlaminar normal stress (s_{tt}), which showed more discrepancy as the radius of the contour increased.

$$\underline{f = 45^\circ}$$

Two roots found by the asymptotic analysis were $I_1 = 0.8543$ and $I_2 = 1.1770$. Both roots were significantly influential to the asymptotic behavior because of the weak singularity. Figure 41 shows distributions of amplitudes of the singular stress components in the global xyz -axes as functions of y for the two roots. None of the stress components is constant for both roots. The traction continuity boundary conditions were satisfied at the ply interface ($y = 0$).

Figures 42 and 43 show stress distribution by asymptotic and numerical analyses in the global xyz -axes and the local rst -axes. The comparisons in both figures were made with the

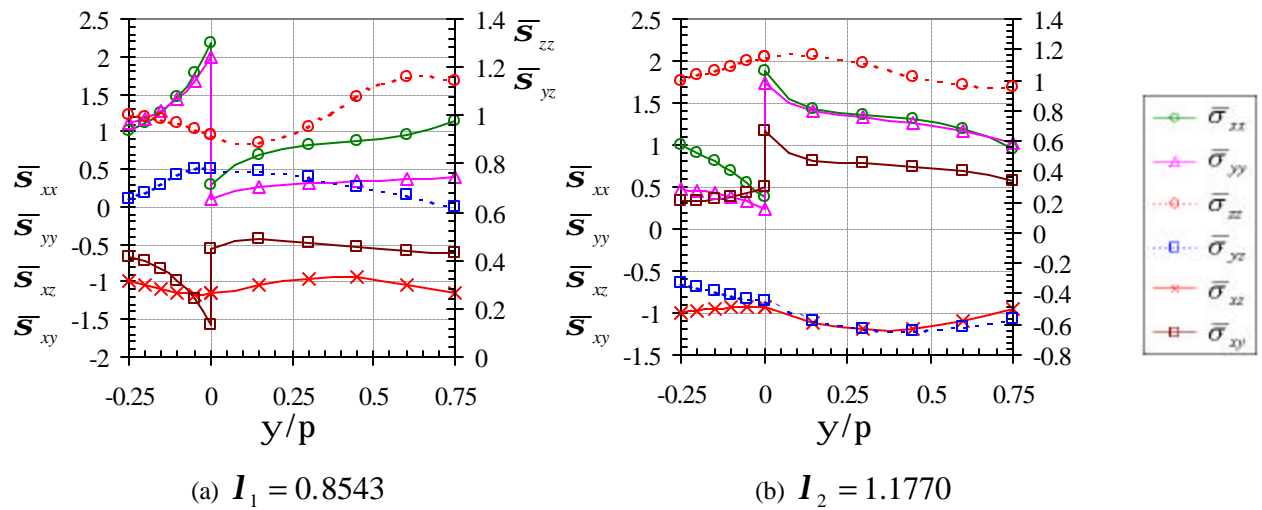
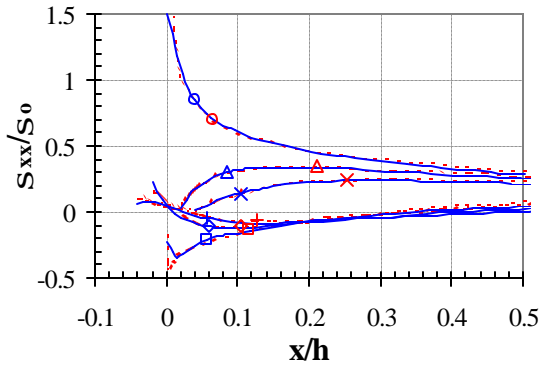
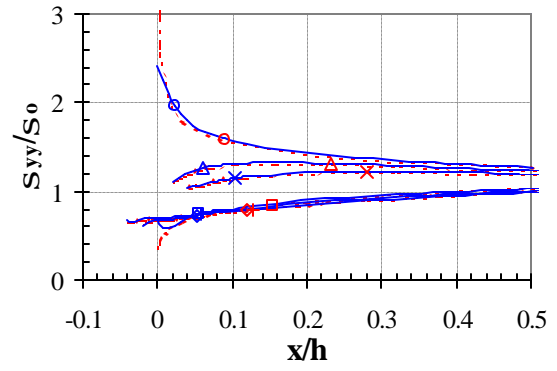


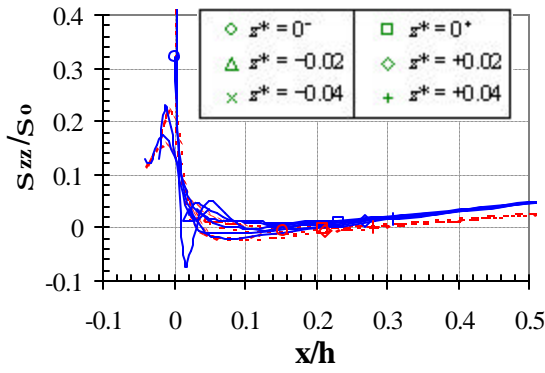
Figure 41. Distribution of Magnitudes of Singular Stress Components with Two Roots for $f = 45^\circ$.



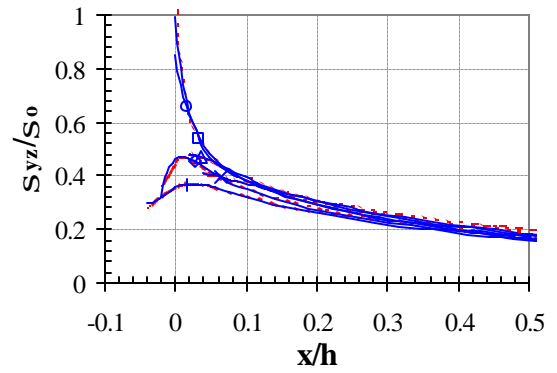
(a) In-plane normal stress (\mathbf{S}_{xx})



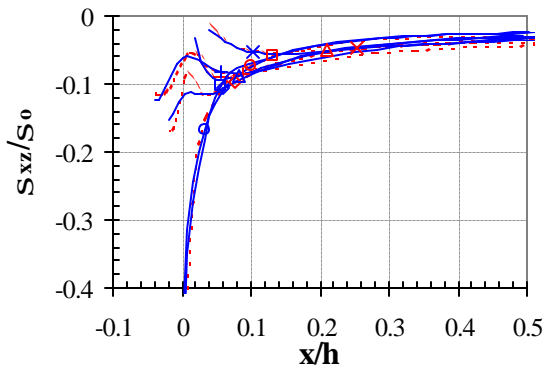
(b) In-plane normal stress (\mathbf{S}_{yy})



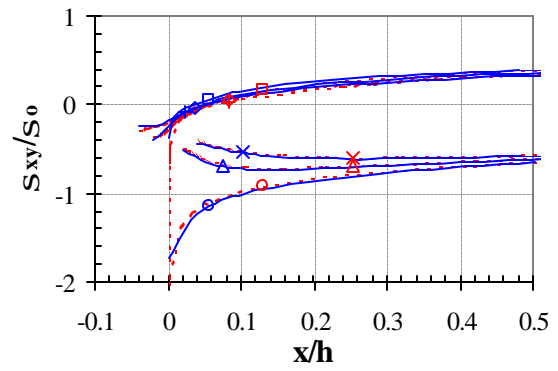
(c) Interlaminar normal stress (\mathbf{S}_{zz})



(d) Interlaminar shear stress (\mathbf{S}_{yz})

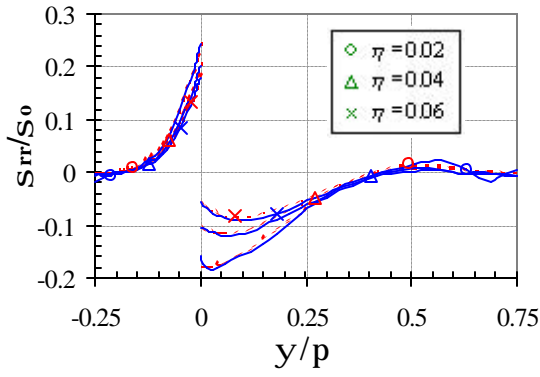


(e) Interlaminar shear stress (\mathbf{S}_{xz})

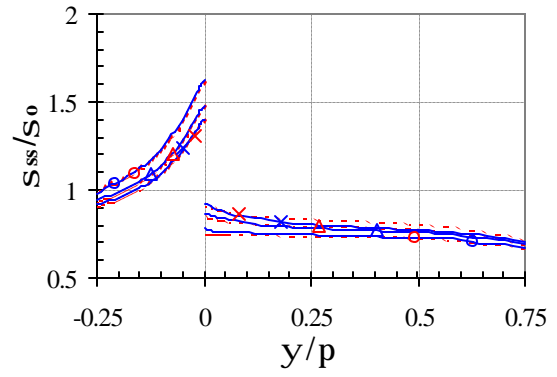


(f) In-plane shear stress (\mathbf{S}_{xy})

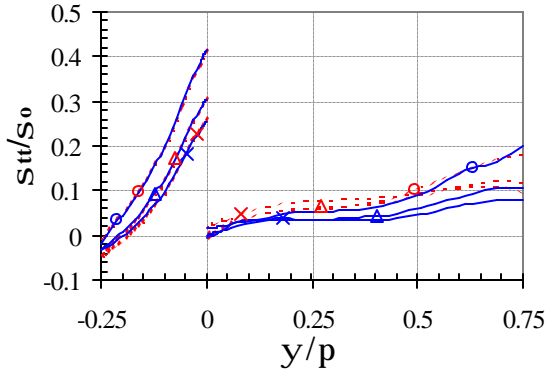
Figure 42. Stress Distribution in Global xyz -Axes by Asymptotic and Numerical Analyses near the Singular Point Along Straight Lines Parallel to the Interface between Two Plies.



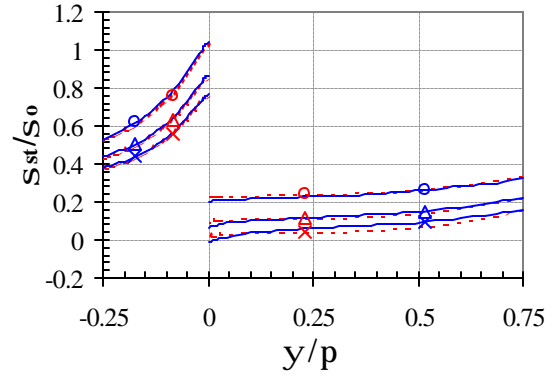
(a) In-plane normal stress (\mathbf{S}_{rr})



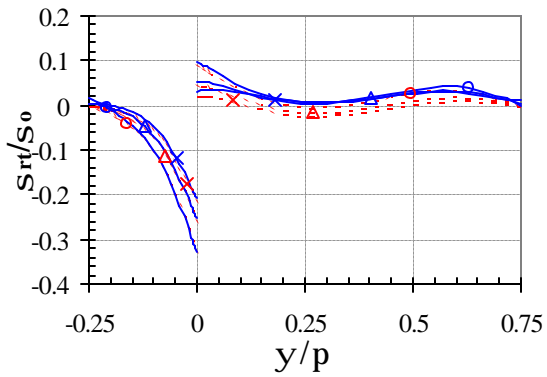
(b) In-plane normal stress (\mathbf{S}_{ss})



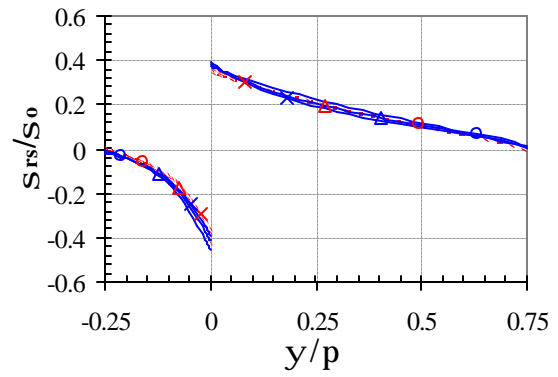
(c) Interlaminar normal stress (\mathbf{S}_{tt})



(d) Interlaminar shear stress (\mathbf{S}_{st})



(e) Interlaminar shear stress (\mathbf{S}_{rt})



(f) In-plane shear stress (\mathbf{S}_{rs})

Figure 43. Stress Distribution in Local rst -Axes with $y = 45^\circ$ by Asymptotic and Numerical Analyses Along Contours of Constant Radii with the Center at the Singular Point.

same multiplicative coefficients, $K_1 = 0.45$ and $K_2 = 0.9$, corresponding to the first and the second power of singularities. Two multiplicative coefficients were in the same order of magnitude, which indicated that both roots contributed similarly to the comparison of the two solutions. The additives in Figure 42 were $F_1 = -1.25$, $F_2 = -0.1$, $F_3 = -1.25$, $F_5 = 1.25$ and $F_4 = F_6 = 0$, and in Figure 43 were $F_2 = -0.1$, $F_3 = -2.5$ and $F_1 = F_4 = F_5 = F_6 = 0$.

In Figure 42, with the range of $x/h > 0.01$, excellent agreement was observed between the full-field numerical solution and two-term asymptotic one for all stresses with one set of the multiplicative factors and the additives. One exception was the interlaminar normal stress (\mathbf{s}_{zz}), which showed a rapid increase in the asymptotic solution as the point moved away from the singular point. All stress components grew infinitely on approaching the singular point along the interface line ($z^* = \pm 0$) in the asymptotic solution, but yielded finite values in the numerical solution.

In Figure 43 three stress components ($\bar{\mathbf{s}}_{rr}$, $\bar{\mathbf{s}}_{rs}$ and $\bar{\mathbf{s}}_{rt}$) from the asymptotic analyses were identically zero at the free edge ($\mathbf{y} = \pm \mathbf{p}/2 + \mathbf{f}$), which satisfied the traction-free boundary condition in Eq. (19), while the numerical solution yielded nearly zero stresses. Excellent agreement was also observed between the full-field numerical solution and two-term asymptotic one for all stresses along the three contours. One exception was again the interlaminar normal stress (\mathbf{s}_{tt}), which showed more discrepancy as the radius of the contour increased.

$$\underline{\mathbf{f} = 60^\circ}$$

Two roots found by the asymptotic analysis were $I_1 = 0.7562$ and $I_2 = 1.4538$. Both roots were significantly influential to the asymptotic behavior because of the weak singularity. Figure 44 shows distributions of amplitudes of the singular stress components in the global

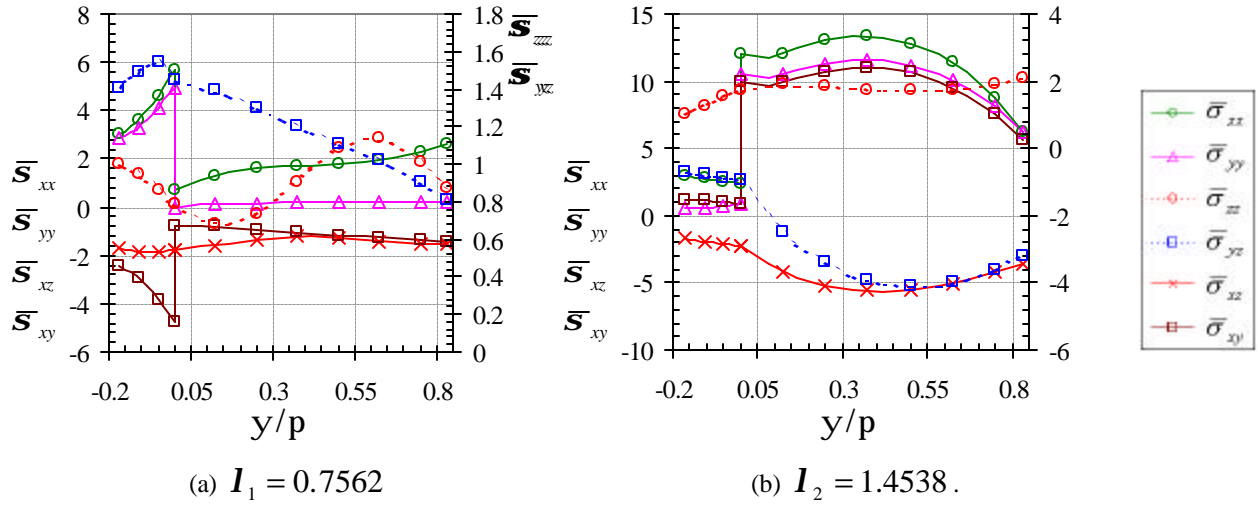
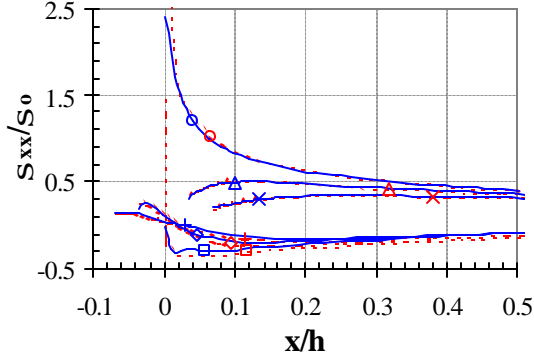


Figure 44. Distribution of Magnitudes of Singular Stress Components with Two Roots for $f = 60^\circ$.

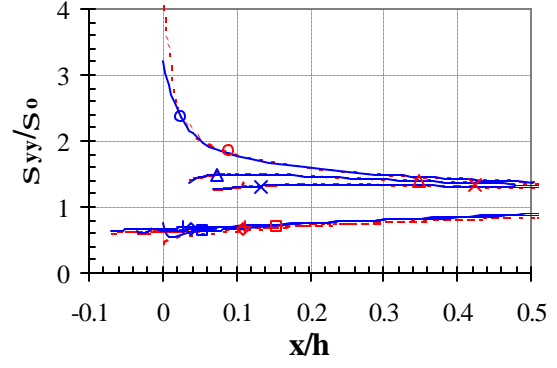
xyz -axes as functions of y for the two roots. None of the stress components is constant for both roots. The traction continuity boundary conditions were satisfied at the ply interface ($y = 0$).

Figures 45 and 46 show stress distribution by asymptotic and numerical analyses in the global xyz -axes and the local rst -axes. The comparisons in both figures were made with the same multiplicative coefficients, $K_1 = 0.11$ and $K_2 = 0.1$, corresponding to the first and the second power of singularities. Two multiplicative coefficients were in the same order of magnitude, which indicated that both roots contributed similarly to the comparison of the two solutions. The additives in Figure 45 were $F_1 = -0.72$, $F_2 = 0.45$, $F_3 = -0.23$, $F_4 = -0.04$, $F_5 = 0.4$ and $F_6 = 0$, and in Figure 46 were $F_2 = 0.44$, $F_3 = -0.95$, $F_4 = -0.03$ and $F_1 = F_5 = F_6 = 0$.

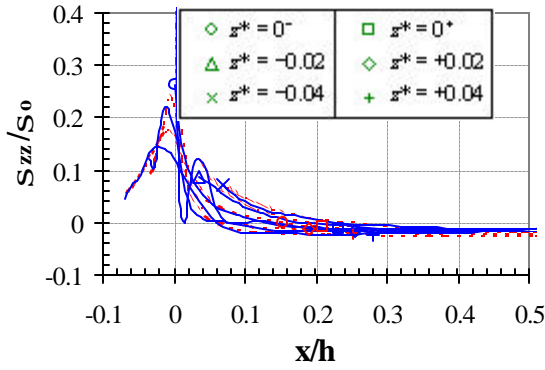
In Figure 45, with the range of $x/h > 0.01$, excellent agreement was observed between the full-field numerical solution and two-term asymptotic one for all stresses with one set of the



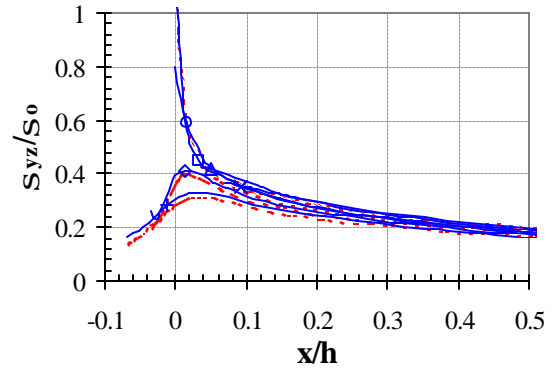
(a) In-plane normal stress (\mathbf{S}_{xx})



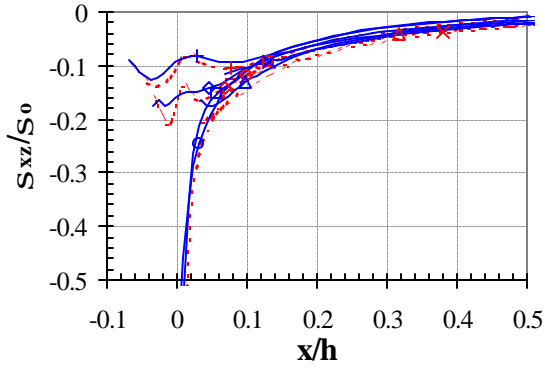
(b) In-plane normal stress (\mathbf{S}_{yy})



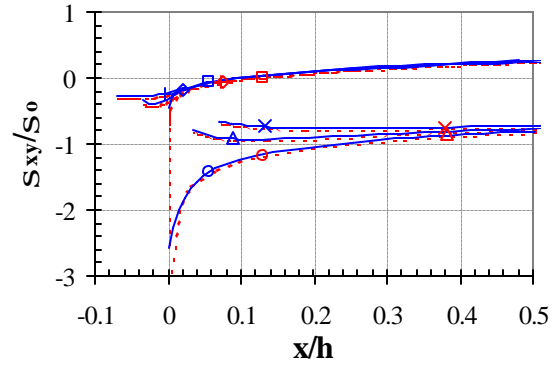
(c) Interlaminar normal stress (\mathbf{S}_{zz})



(d) Interlaminar shear stress (\mathbf{S}_{yz})

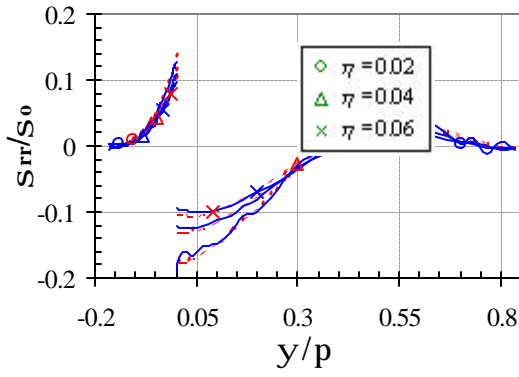


(e) Interlaminar shear stress (\mathbf{S}_{xz})

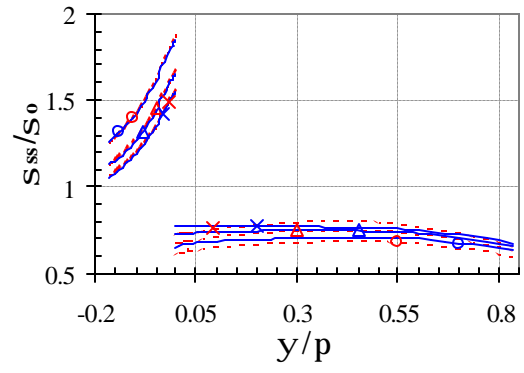


(f) In-plane shear stress (\mathbf{S}_{xy})

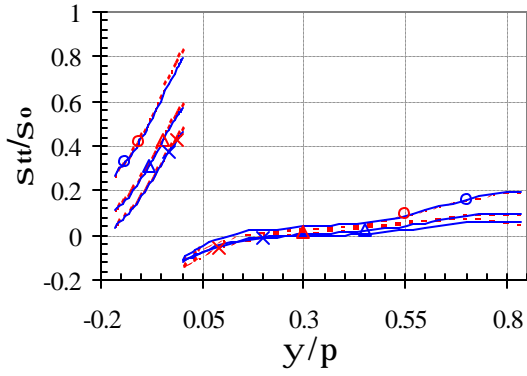
Figure 45. Stress Distribution in Global xyz -Axes by Asymptotic and Numerical Analyses near the Singular Point Along Straight Lines Parallel to the Interface between Two Plies.



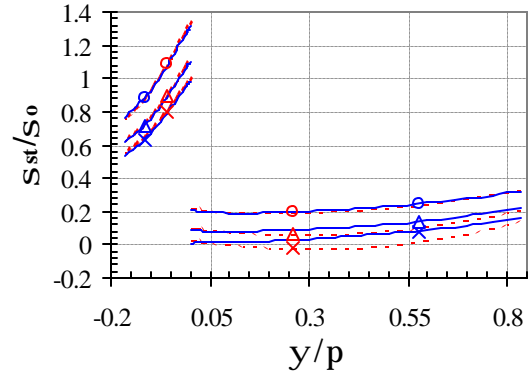
(a) In-plane normal stress (\mathbf{S}_{rr})



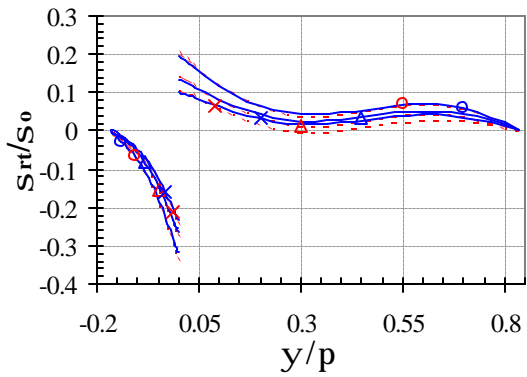
(b) In-plane normal stress (\mathbf{S}_{ss})



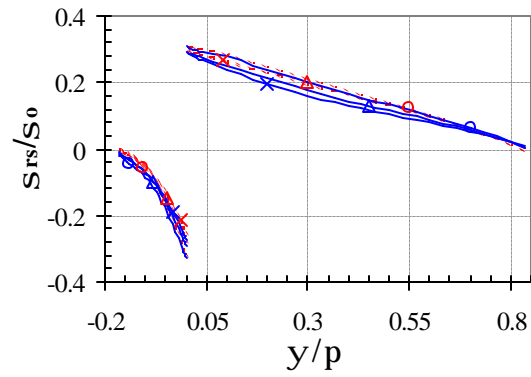
(c) Interlaminar normal stress (\mathbf{S}_{tt})



(d) Interlaminar shear stress (\mathbf{S}_{st})



(e) Interlaminar shear stress (\mathbf{S}_{rt})



(f) In-plane shear stress (\mathbf{S}_{rs})

Figure 46. Stress Distribution in Local rst -Axes with $f = 60^\circ$ by Asymptotic and Numerical Analyses Along Contours of Constant Radii with the Center at the Singular Point.

multiplicative factors and the additives. One exception was the interlaminar normal stress (\mathbf{s}_{zz}), which showed a rapid increase in the asymptotic solution as the point moved away from the singular point. All stress components grew infinitely on approaching the singular point along the interface line ($z^* = \pm 0$) in the asymptotic solution but yielded finite values in the numerical solution.

In Figure 46 three stress components ($\bar{\mathbf{s}}_{rr}$, $\bar{\mathbf{s}}_{rs}$ and $\bar{\mathbf{s}}_{rt}$) from the asymptotic analyses were identically zero at the free edge ($\mathbf{y} = \pm \mathbf{p}/2 + \mathbf{f}$), which satisfied the traction-free boundary condition in Eq. (19), while the numerical solution yielded nearly zero stresses. Excellent agreement was also observed between the full-field numerical solution and two-term asymptotic one for all stresses along the three contours. One exception was again the interlaminar normal stress (\mathbf{s}_{tt}), which showed more discrepancy as the radius of the contour increased.

6.4 SUMMARY AND RECOMMENDATIONS

Asymptotic and numerical analyses were performed to provide an accurate stress field of laminated composites with slanted free edges in the vicinity of the ply interface and the free edge. The analyses were performed with various slanted angles. The numerical analysis was developed based on the B-spline approximation method of displacement functions. Stress components by the numerical method were obtained for a laminated composite with the lay-up of [45/-45]_s AS4/3501-6 laminate under a uniaxial loading.

The behavior of power of singularity was highly dependent on the slanted angles of the free edge. The power of singularities was found with two real numbers at $0^\circ \leq \mathbf{f} \leq 2^\circ$ and $38^\circ \leq \mathbf{f} \leq 90^\circ$, and with complex conjugated numbers at $3^\circ \leq \mathbf{f} \leq 37^\circ$. At every slanted angle, excellent agreement was observed for the stress distributions to a distance of approximately

one-half-ply thickness from the singular point between the full-field numerical solution and the two-term singular asymptotic solution with appropriate multiplicative coefficients and constant additives.

7. MECHANICAL MODELING AND PREDICTION OF BULK PROPERTIES OF OPEN-CELL CARBON FOAM

Carbon foam is emerging as an ultralightweight and efficient thermal management material for many multifunctional applications, such as high-density electronics, hybrid diesel-electric vehicles, communication satellites, and advanced aircraft [37]. Carbon foam was shown to demonstrate numerous unique properties that make it an attractive material for the use of the low-cost, lightweight, insulating, energy-absorbing structural components [38].

The carbon foam is expected to possess isotropic properties macroscopically. However, a microstructure of an open-cell foam, based on the minimum surface energy during the foaming process, possesses a tetrahedral structure of the foam ligaments oriented approximately 109 degrees with each other [39,40], as in Figure 47. Preliminary investigation reveals that the graphitic alignment of the cell ligaments varies along its longitudinal (axial) direction. Processing parameters, such as temperature, pressure, etc., control the porosity and the graphitic alignment of the carbon foam, which in turn determine its geometries and material properties. With an ongoing research effort to investigate an appropriate microstructural characterization technique to correlate the foam microstructure with the processing parameters, the microstructural geometry and material properties of the foam, including mechanical elastic moduli, Poisson's ratio, thermal conductivity, etc., will be used for the mechanical and thermal analysis.

Because of the tetrahedral cell microstructure of the carbon foam, the macroscopic properties, such as foam moduli and strengths, are critically influenced by the deformation characteristics of the cell ligaments. Further, as stated earlier, the cross-sectional area and the graphitic alignment (hence the directional material properties) of the cell ligaments vary along the ligament length. The tetrahedral cell microstructure consists of four ligaments as a frame

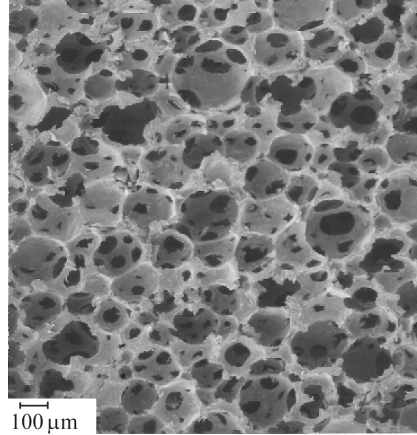


Figure 47. Microstructure of Carbon Foam.

structure, and the four ligaments connected to a common node are oriented approximately 109 degrees to one another in 3-D space. The cross-sectional area and the material properties vary along the longitudinal directions of the ligaments. Because of the complex geometry and anisotropic material properties, it is appropriate to perform the analysis numerically to obtain accurate displacement and stress field solutions.

The numerical model should be able to analyze the deformation of the ligaments that are connected and oriented in the 3-D space under arbitrary loading conditions. The analysis should be able to predict longitudinal and transverse displacements as well as rotations, and to calculate the stress and strain distributions along the ligaments. To achieve the above goals, the geometry of cell ligaments in the carbon foam needs to be characterized based on the bubble-forming process. With the geometry known, the stress analysis can be performed with the microstructure of the carbon foam under a certain boundary condition. By applying appropriate boundary conditions, we can then calculate effective elastic Young's moduli and Poisson's ratio of the foam in the macroscopic level.

7.1 MODELING OF CARBON FOAM

7.1.1 Characterization of Geometry of Unit Cell of Carbon Foam

Because of the randomness and complexity of the microstructure of the carbon foam, it is difficult to consider whole individual cells in the foam. Instead, an assumption is made that the behavior of the material is represented with a unit cell of the foam containing four ligaments. The microstructural characterization of the representative unit-cell ligaments will then be correlated with the macroscopic bulk properties in a statistical means. To obtain a representative response of the unit cell, the geometry and pertinent material properties of the unit cell are based on the collection of data on the size, shape, and property variation of the foam ligaments.

To analyze the materials behavior of the foam, we need to generate the geometry of the unit cell of the foam in an appropriate manner. The unit cell can be generated by making use of symmetry that exists in the bubble-forming process. Surface energy of nucleation and expansion of the bubbles during the foam-forming process are minimal when the centers of the bubbles coincide with the four vertices of a tetrahedron. The vertices of the tetrahedron are defined by first considering a cube. For the sake of simplicity of defining the unit cell, the dimension of the cube is taken as $2a \times 2a \times 2a$ in the x -, y - and z -directions, with its origin (point 0) located at the center of the cube, as in Figure 48. The vertices of the tetrahedron confined in the cube are the four corner points of the cube that are located diagonally with each other on the faces of the cube (e.g., points 2, 4, 5, 7 in Figure 48). Connecting the four corner points then generates a tetrahedron, whose volume is $V_{tetra} = 8a^3/3$. This tetrahedron can be divided into four equal subregions containing the origin of the tetrahedron. The vertices of the subregions are shown in Figure 48 as 0-2-7-4, 0-7-5-4, 0-4-5-2, and 0-2-7-5, respectively.

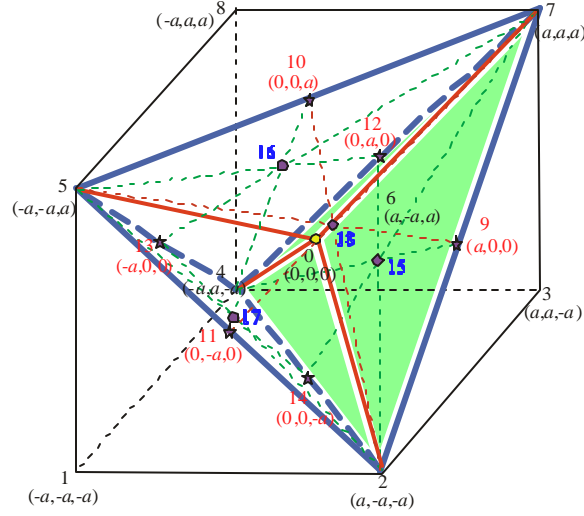


Figure 48. Points and Lines in a Cube and a Tetrahedron for Generating a Unit Cell of Carbon Foam.

The next step is to generate four spheres growing from the four vertices (the four corner points) of the tetrahedron. The spheres represent bubbles that are produced during the foaming process. The radii of the spheres will determine the porosity of the unit cell of the foam. Subtracting the volume of the bubbles (spheres) from that of the tetrahedron creates the unit cell of the carbon foam, as Figure 49 shows. The porosity (f) of the foam is thus calculated by $f = 1 - V_{unit}/V_{tetra}$, where V_{unit} is the volume of the unit cell. Figure 50 shows the unit cells with three different levels of porosity.

For convenience, local coordinate systems, whose x -directions are parallel to the longitudinal directions (axes) of the ligaments, are defined by using four lines that connect the points (0-15, 0-16, 0-17, and 0-18) in Figure 48. The local coordinate systems are useful because the ligaments possess material symmetry along its longitudinal axes due to the graphitic alignment.

For the numerical analysis using an FEM, the ligaments of the foam generated above are discretized into FEs along the local longitudinal directions.

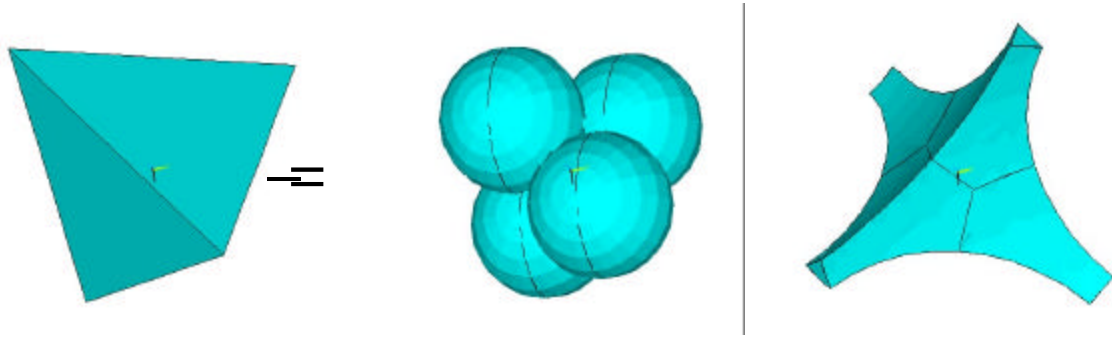


Figure 49. A Tetrahedron and Spheres to Generate a Unit Cell of Carbon Foam.

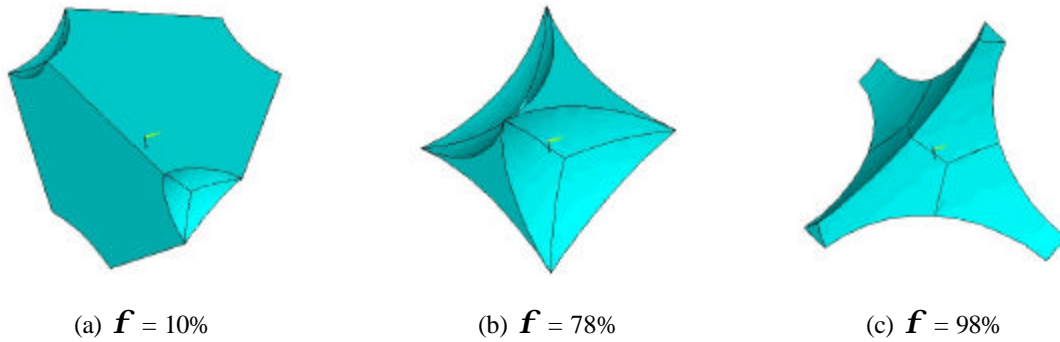


Figure 50. Unit Cells of Carbon Foam with Various Porosities.

The coordinates of the cross-sectional area as well as the nodal points along the longitudinal directions are calculated by the following method: a shaded volume in Figure 48 is selected as one of the four subtetrahedra and plotted in Figure 51. The selected subtetrahedron can be subdivided further into three sub-subtetrahedra (0-15-2-7, 0-15-7-4, and 0-15-4-2) with respect to symmetry planes.

As the bubble grows from the three vertices of the subtetrahedron, increasing the porosity, the unit cell undergoes three different shapes. Figure 52 shows the three different cross-sectional slices in plane 2-4-7 during the bubble-forming process. When the porosity of the carbon foam is 78 percent, the bubbles contact with each other. For the open-cell carbon

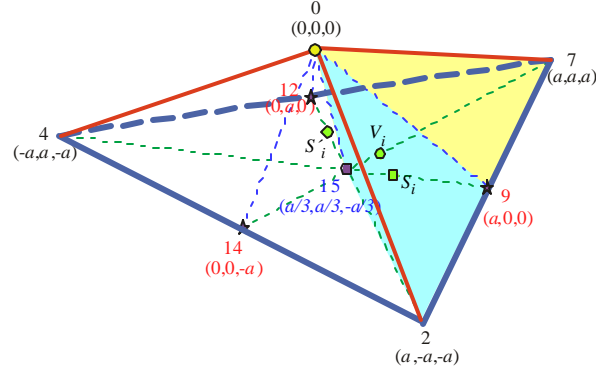


Figure 51. One of Four Subtetrahedra Considering Symmetry in Figure 48.

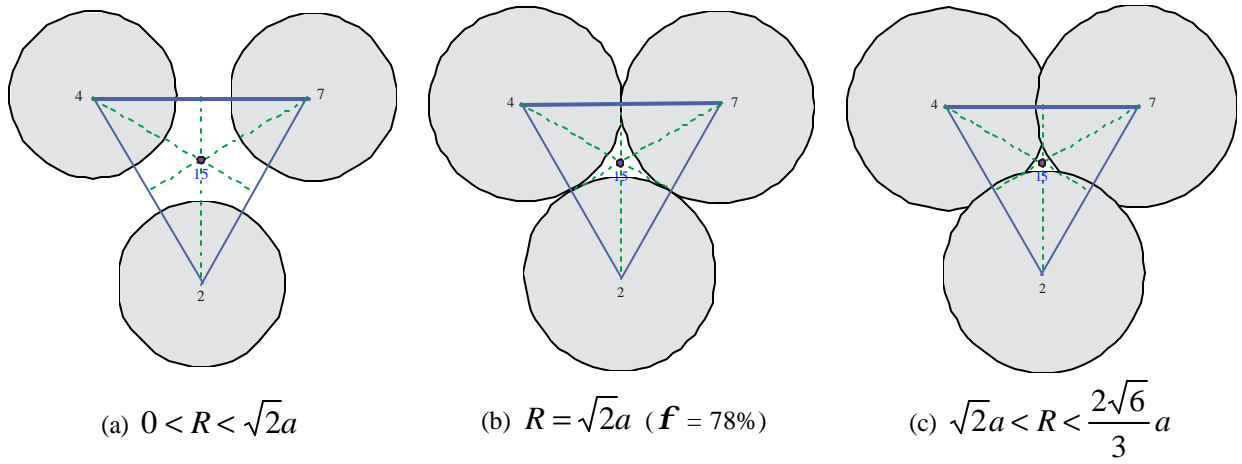


Figure 52. Cross-Sectional Slices During Bubble-Forming Process (R is the Radius of Spheres).

foams, whose typical porosities are higher than 80 percent, the bubbles coalesce with each other, as shown in Figure 52(c).

Figure 53 shows the intersection of the subtetrahedron and the bubble spheres. The subtetrahedron subtracted from the bubbles defines the ligament of the carbon foam. As Figure 53 shows, points A , B and a , b are the intersections of the half of the sub-subtetrahedron (0-15-9-7) and a bubble sphere with the radius of R . The coordinates of these points are as follows:

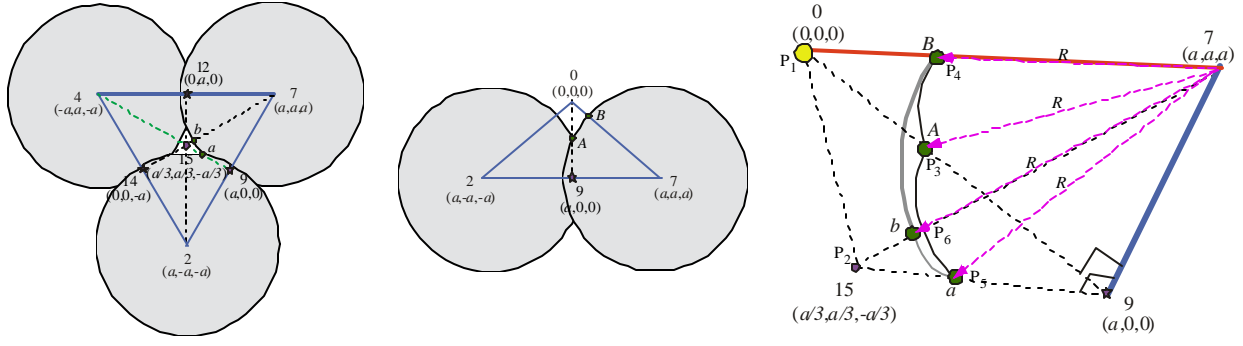


Figure 53. Intersection of a Subtetrahedron and Bubble Spheres ($\sqrt{2}a < R < \frac{2\sqrt{6}}{3}a$).

$$\begin{aligned}
 (x_1, y_1, z_1) &= (0, 0, 0) \\
 (x_2, y_2, z_2) &= \left(\frac{a}{3}, \frac{a}{3}, -\frac{a}{3} \right) \\
 (x_3, y_3, z_3) &= (a - \sqrt{R^2 - 2a^2}, 0, 0) \\
 (x_4, y_4, z_4) &= \left(a - \frac{R}{\sqrt{3}}, a - \frac{R}{\sqrt{3}}, a - \frac{R}{\sqrt{3}} \right) \\
 (x_5, y_5, z_5) &= \left(a - \sqrt{\frac{2}{3}(R^2 - 2a^2)}, \frac{1}{2}\sqrt{\frac{2}{3}(R^2 - 2a^2)}, -\frac{1}{2}\sqrt{\frac{2}{3}(R^2 - 2a^2)} \right) \\
 (x_6, y_6, z_6) &= \left(a - \frac{R}{\sqrt{6}}, a - \frac{R}{\sqrt{6}}, a - \frac{2R}{\sqrt{6}} \right).
 \end{aligned} \tag{32}$$

The subtracted sub-subtetrahedron in Figure 53 is further discretized into the finite volumes along the ligament axis ($\overline{P_1 P_2}$). Discretized points ($Q_1, Q_x, \Lambda, Q_{n+1}$) on the ligament axis form discretization planes perpendicular to the ligament axis, which intersect with the lines ($\overline{P_3 P_5}$ and $\overline{P_4 P_6}$) on the ligament surface at points $S_1, S_x, \Lambda, S_{n+1}$ and $V_1, V_x, \Lambda, V_{n+1}$, respectively, as shown in Figure 54. The coordinates of the points (Q_i, S_i and V_i) are obtained by using geometric arithmetic as follows:

$$\begin{aligned}
 x_{Q_i} &= \frac{1}{3} \left[a + \left(\frac{i-1}{n} - 1 \right) \sqrt{R^2 - 2a^2} \right], \quad y_{Q_i} = x_{Q_i}, \quad z_{Q_i} = -x_{Q_i} \\
 x_{S_i} &= \frac{1}{3} \left[2a + 3x_{Q_i} - \sqrt{2} \sqrt{3R^2 - 6a^2 - (3x_{Q_i} - a)^2} \right], \quad y_{S_i} = -\frac{1}{2}(x_{S_i} - 3x_{Q_i}), \quad z_{S_i} = -y_{S_i} \\
 x_{V_i} &= \frac{1}{6} \left[4a + 6x_{Q_i} - \sqrt{2} \sqrt{3R^2 - (3x_{Q_i} - a)^2} \right], \quad y_{V_i} = x_{V_i}, \quad z_{V_i} = 2x_{V_i} - 3x_{Q_i}.
 \end{aligned} \tag{33}$$

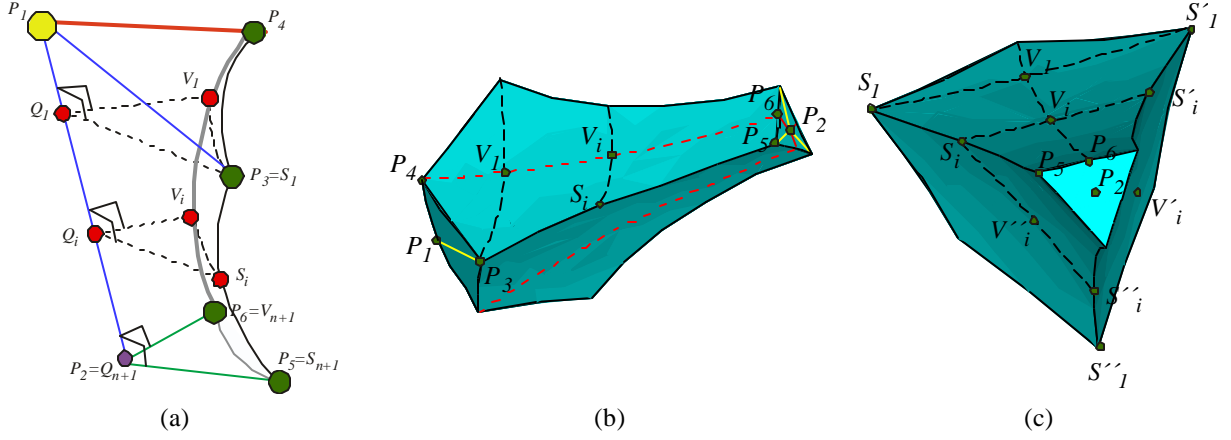


Figure 54. A Sub-subtetrahedron Discretized into Finite Volumes Along a Ligament Axis.

The coordinates of the points in other sub-subtetrahedra are obtained by reflection with respect to symmetry planes. For example, a point S'_i on a plane (0-15-12) is the reflection of the point S_i on a plane (0-15-9) with respect to a symmetry plane (0-15-7), as can be inferred from Figure 51. The formula for the reflection in a plane with equation $ax + by + cz + d = 0$ is

$$(x, y) \propto \frac{1}{a^2 + b^2 + c^2} [M(x_o, y_o, z_o) - (2ad, 2bd, 2cd)], \quad (34)$$

where M is a matrix given by

$$M = \begin{bmatrix} -a^2 + b^2 + c^2 & -2ab & -2ac \\ -2ab & a^2 - b^2 + c^2 & -2bc \\ -2ac & -2bc & a^2 + b^2 - c^2 \end{bmatrix}, \quad (35)$$

and the formula for the plane going through (x_o, y_o, z_o) , (x_1, y_1, z_1) and (x_2, y_2, z_2) is given by

$$\begin{vmatrix} x - x_o & y - y_o & z - z_o \\ x_1 - x_o & y_1 - y_o & z_1 - z_o \\ x_2 - x_o & y_2 - y_o & z_2 - z_o \end{vmatrix} = 0. \quad (36)$$

Once the coordinates of the points in Figure 54 (c) are obtained by using Eqs. (33) through (36), the ligament geometry of the unit cell as well as the material property distribution

along the ligaments can be generated with the nodal points (Q_i) with the cross-sectional information ($S_i, V_i, S'_i, V'_i, S''_i, V''_i$).

The above procedure of defining the model geometry can be used in either developing a simplistic FE model, assuming the ligaments behave like beam elements, or generating 3-D FE meshes with commercial FE model packages, such as ANSYS. Figure 55 shows 3-D FE meshes generated by ANSYS and equivalent 1-D beam meshes. The solution of the beam FEA requires further development of the beam model and thus is not included in this section. However, the stress analysis of the unit cell using the 3-D meshes is presented in this section.

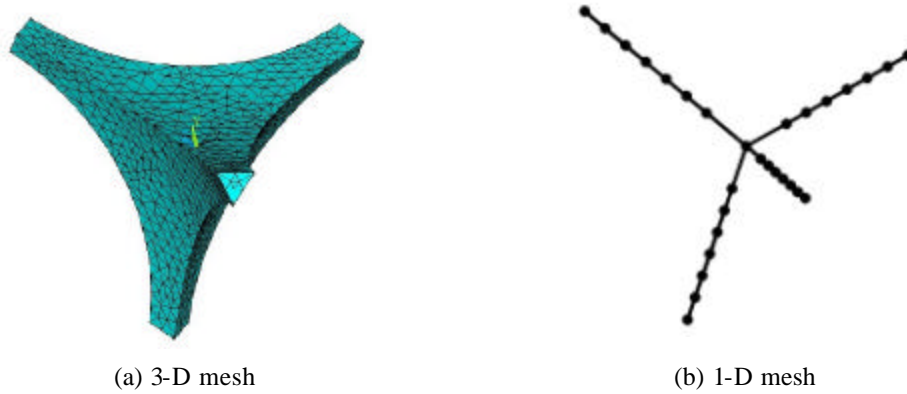


Figure 55. 3-D Mesh versus 1-D Beam Mesh of the Unit Cell of Carbon Foam.

7.1.2 Determination of Boundary Condition

The FEA requires appropriate loading and boundary conditions to be applied on the unit cell of the foam. For the analysis of the unit cell, we need to correlate the overall loading/boundary conditions (OBC) with the ligament boundary conditions (LBC). The LBC varies with the location, size and orientation of the unit cell in the carbon foam under an OBC. However, to correlate LBC with OBC, the macroscopic (bulk) material symmetry of the foam

needs to be known. The measured macroscopic (bulk) properties of several carbon foams indicate that the bulk properties of carbon foam are, in general, isotropic [41,42]. The bulk material isotropy is thus assumed in this study.

The LBC can be determined by generating an imaginary tetrahedron inside which a unit cell of the foam is to be located, as in Figure 56. The OBCs are then applied to the surfaces of the tetrahedron. Under the OBC, the bulk tetrahedron is assumed to be isotropic, and the displacements in the tetrahedron are calculated point by point. The displacements are collected for the points that coincide with the tips of the ligament. The FEA is then run by assigning the corresponding displacement boundary conditions to the unit cell that was generated in the previous section.

The FEA is repeated with the variation of size and orientation, as the unit cells are distributed randomly in the bulk of carbon foam. As the selection of the input parameters (size, orientation) increases, the computational time for numerical analysis increases rapidly, and therefore, we need the 1-D beam analysis instead of the 3-D analysis. A statistical approach should be incorporated for the random cell size and its orientations.

7.2 NUMERICAL CALCULATION

7.2.1 Prediction Method of Effective Bulk Moduli of Foam

To assess the validity of the model, effective bulk moduli were predicted for polyurethane foam as well as the carbon foam, based on the ligament material properties. Although the material orthotropy of the ligaments can be included in the effective properties prediction, at present for convenience, ligaments are assumed as isotropic material. Densities of the ligaments ($\rho_{ligament}$) in the polyurethane, carbonized and graphitized foams were taken as 1.2,

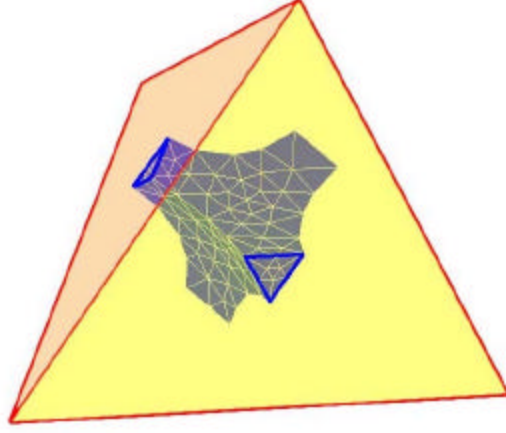


Figure 56. An Imaginary Tetrahedron inside which a Unit Cell of the Foam is Located.

1.8, and 2.2 g/cm³, respectively. The foam bulk density (ρ_{bulk}) can then be related with the material density of the ligament as

$$\rho_{bulk} = \rho_{ligament} (1 - f) . \quad (37)$$

Since the size of the bubbles determined the porosity, the foam density can be related with the bubble size (radius) as well, as plotted in Figure 57.

The FEA was performed with ANSYS. The FE meshes of the unit cell were generated with unit length of cube, tetrahedron and bubble spheres with radius determined by Figure 57. The unit cell was loaded under a constant uniaxial strain in a loading direction, and constrained to prevent deformation in the other two perpendicular directions. The uniform uniaxial strain boundary condition was achieved by applying a prescribed displacement boundary condition on nodal points on the tip surfaces of the ligaments, where the tip surfaces coincided with the surfaces of the tetrahedron, as explained earlier. The values of the prescribed displacements in the loading direction varied with the location of the nodal points, whereas those in other directions perpendicular to the loading direction were set to zero. For example, if the loading was applied in the x -direction, the displacement values were

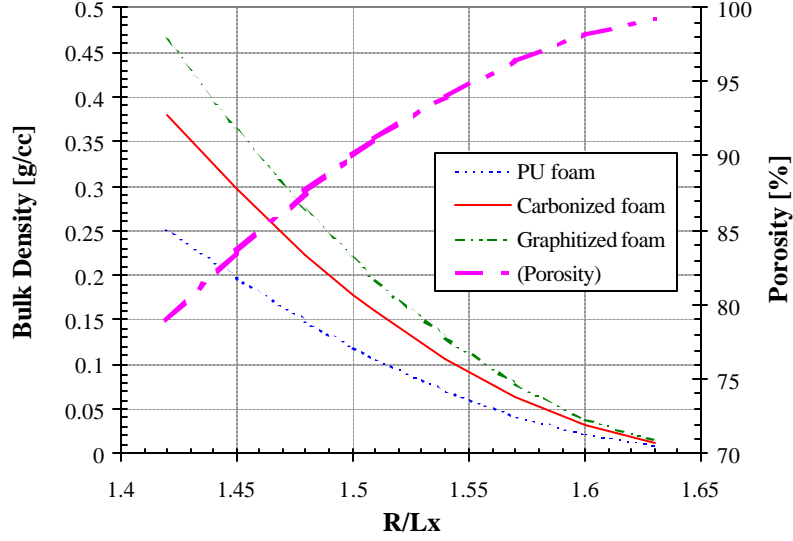


Figure 57. Relation between Bulk Density, Porosity and Bubble Size for Open-Cell Foams.

$$d_x = x/\mathbf{e}_x^o, \quad d_y = 0, \quad d_z = 0, \quad (38)$$

where x and \mathbf{e}_x^o are the nodal coordinate and the applied constant strain, respectively.

Effective stress components ($\bar{\mathbf{s}}_i$) can be calculated by taking volumetric averages of resultant stress field over the volume of the tetrahedron, such as

$$\bar{\mathbf{s}}_i = \frac{\sum_e \mathbf{s}_i^e v^e}{V_{tetra}} = \frac{\sum_e \mathbf{s}_i^e v^e}{V_{unit}} (1-f), \quad (39)$$

where \mathbf{s}_i^e and v^e are the elemental stress and volume of the unit cell, respectively. According to the 3-D constitutive law of isotropic material, the effective moduli (\bar{E}) and Poisson's ratio ($\bar{\nu}$) of the unit cell were calculated as follows:

$$\bar{E} = \frac{1}{\mathbf{e}_i^o} [\bar{\mathbf{s}}_i - \bar{\nu} (\bar{\mathbf{s}}_j + \bar{\mathbf{s}}_k)] \quad (40)$$

$$\bar{\nu} = \frac{\bar{\mathbf{s}}_j}{\bar{\mathbf{s}}_i + \bar{\mathbf{s}}_k},$$

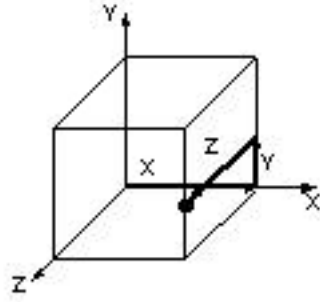
where \bar{S}_i is the volumetric average of stress components in the loading direction, and \bar{S}_j and \bar{S}_k are those in the other two directions perpendicular to the loading direction.

The carbon foam is filled with the unit cells that are randomly oriented in 3-D space and connected with each other at the tips of the ligaments. The random nature of orientation leads to the isotropic properties. Therefore, collection of the randomly oriented unit cells needed to be considered in the calculation of the effective bulk moduli of the carbon foam. Instead of the rigorous random generation of the orientation, however, different orientation schemes were employed in this study in a less rigorous manner using mutually orthogonal coordinate systems: Cartesian and spherical coordinate systems, as shown in Figure 58.

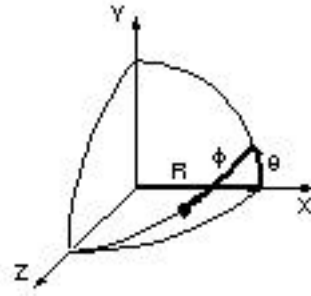
When the Cartesian coordinate system was used to rotate the unit cell with respect to x -, y - and z -axes, as shown in Figure 58(a), only two axes among the three axes were considered, since the orientation with respect to the axis parallel to the uniaxial loading did not alter the effective moduli of the unit cell. For example, when the load was applied to the direction parallel to the x -axis, only two rotations with respect to y - and z -axes were considered in the moduli calculation. Meanwhile, with the spherical coordinate system, two angles, zenith (q) and azimuth (f) angles, were used to rotate the unit cell, as shown in Figure 58(b). Three different rotating schemes tried in these coordinate systems were

1. Scheme I: first rotation in y -axis (q_y) and the second rotation in z -axis (q_z).
2. Scheme II: first rotation in z -axis (q_z) and the second rotation in y -axis (q_y).
3. Scheme III: first rotation in zenith (q) and the second rotation in azimuth (f).

Young's moduli of the unit cells were calculated by using Eq. (40) for an isotropic foam with the changes of angles in Schemes I, II and III, and the results were plotted in Figures 59, 60, and 61, respectively. The bulk Young's modulus and Poisson's ratio of the

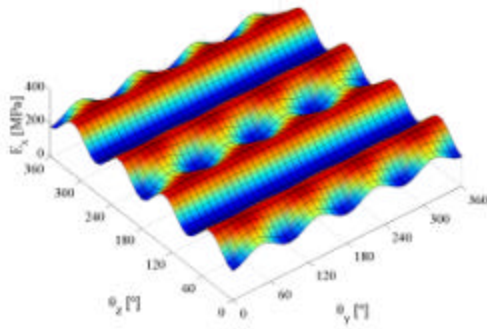


(a) Cartesian coordinate

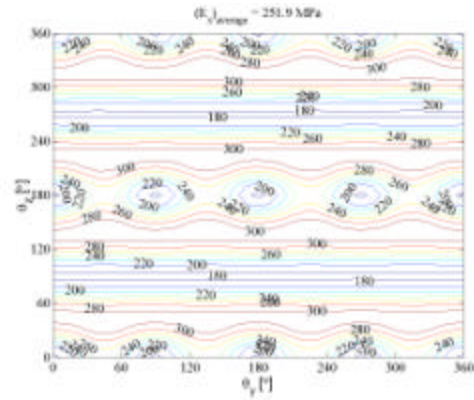


(b) Spherical coordinate

Figure 58. Coordinate Systems for Rotating Unit Cell for Simulating Random Orientation.

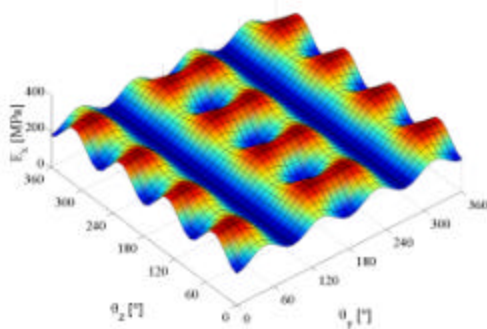


(a) Surface plot

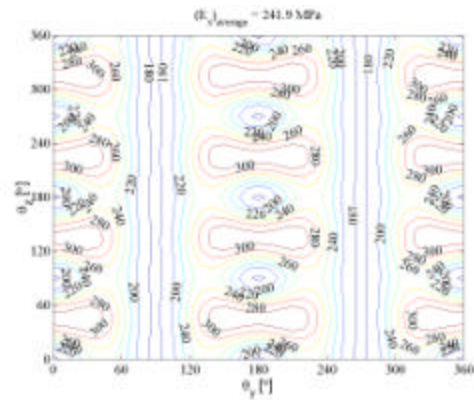


(b) Contour plot

Figure 59. Variation of Young's Moduli of Unit Cells of Isotropic Foam on the Changes of Angles in Cartesian Coordinate Axes, with the First Rotation in the y-Axis and the Second Rotation in the z-Axis.



(a) Surface plot



(b) Contour plot

Figure 60. Variation of Young's Moduli of Unit Cells of Isotropic Foam on the Changes of Angles in Cartesian Coordinate Axes, with the First Rotation in the z-Axis and the Second Rotation in the y-Axis.

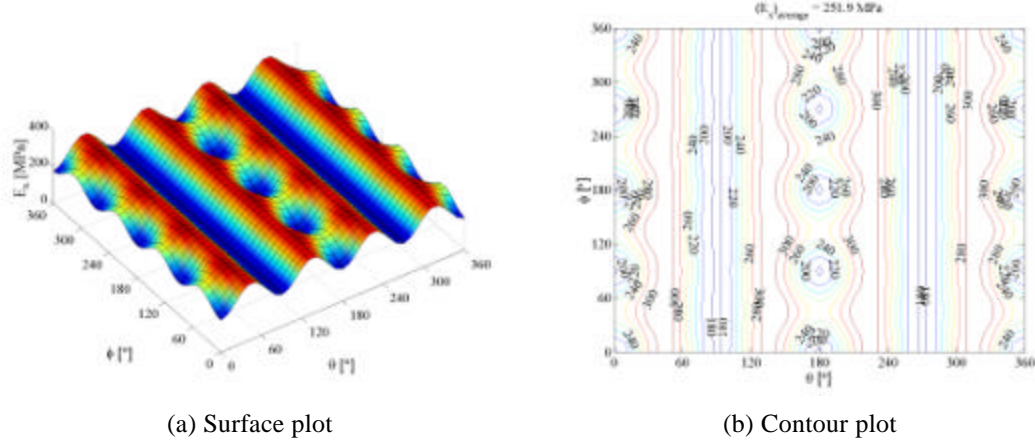


Figure 61. Variation of Young's Moduli of Unit Cells of Isotropic Foam on the Change of Angles in Spherical Coordinate Axes.

material were 4.5 GPa and 0.33, respectively. Both mesh and contour plots were drawn for the orientation angles from 0° to 360° . Average Young's moduli and Poisson's ratios are listed in Table 8. The figures show periodic patterns of the moduli in both rotating angles either in a symmetric way or an antisymmetric way. The periodic variations observed in each scheme were as follows:

1. Scheme I:

$$E(\mathbf{q}_y, \mathbf{q}_z) = E(\mathbf{q}_y, \mathbf{q}_z + 180^\circ) = E(\mathbf{q}_y + 180^\circ, 180^\circ - \mathbf{q}_z) = E(\mathbf{q}_y + 180^\circ, 360^\circ - \mathbf{q}_z) \quad (41)$$

2. Scheme II:

$$E(\mathbf{q}_y, \mathbf{q}_z) = E(\mathbf{q}_y + 180^\circ, \mathbf{q}_z) = E(180^\circ - \mathbf{q}_y, \mathbf{q}_z + 180^\circ) = E(360^\circ - \mathbf{q}_y, \mathbf{q}_z + 180^\circ) \quad (42)$$

3. Scheme III:

$$E(\mathbf{q}, \mathbf{f}) = E(\mathbf{q} + 180^\circ, \mathbf{f}) = E(180^\circ - \mathbf{q}, \mathbf{f} + 180^\circ) = E(360^\circ - \mathbf{q}, \mathbf{f} + 180^\circ) \quad (43)$$

Because of the periodicity, to completely fill the isotropic bulk foam with the unit cells, it was necessary to rotate the unit cell only from 0° to 180° in both axes. Since the moduli were calculated by taking the average over all orientations, it was not sensitive on the selection of the coordinate system. In this study the spherical coordinate system was chosen as the rotating method in the moduli calculation.

Table 8
Predicted Effective Young's Moduli and Poisson's Ratio of an Isotropic Foam

	E (MPa)	n
Scheme I	251.9	0.37
Scheme II	241.9	0.39
Scheme III	251.9	0.37

7.2.2 Results: Polyurethane Foam

Effective bulk properties of the polyurethane foam were calculated with the present method at various densities. The Young's modulus and Poisson's ratio of the polyurethane as the ligament properties were 1.8 GPa and 0.33, respectively. The property predictions by the present method were compared with those both in a handbook [37] and an existing formula suggested by Warren and Kraynik [39], as shown in Figure 62. The latter was formulated based on a similar unit-cell model as the present one, but limited to the ligaments that possess the isotropic material properties and uniform cross sections, such as circular, triangular, and plateau border cross sections. The plateau border cross section corresponds to the space between three identical, mutually tangent circles. Meanwhile, the handbook provides only shear moduli at various ranges of densities. Therefore, the Young's moduli were back calculated from the shear moduli, along with an assumed Poisson's ratio of 0.33. Note that since the radius of the bubbles for the open-cell foams was greater than $\sqrt{2}a$, the bulk density of the open-cell foams should be less than 0.266 g/cm^3 .

For low-density foams, the bending compliance of the ligaments is much greater than the axial compliance. Therefore the bulk Young's modulus is dominated by the bending behavior of foam ligaments. The dominance on the bending behavior results in quadratic variation of the modulus with the density increment, as was also concluded in the previous

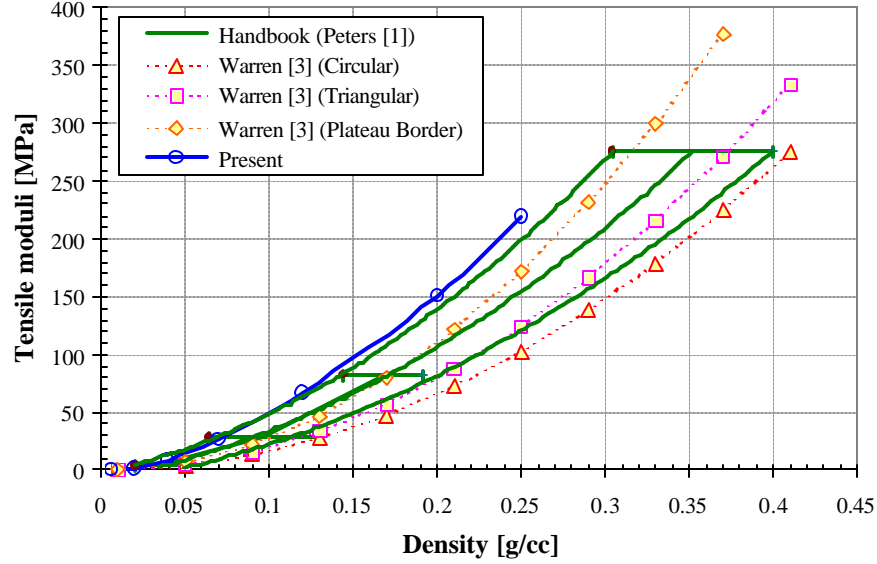


Figure 62. Prediction of Bulk Young's Moduli of Polyurethane Foam at Various Densities.

prediction method by Warren and Kraynik. As lying on upper bound, the present results agreed well with both the existing formula and the measured data.

Figure 63 shows predicted Poisson's ratios of the polyurethane foam at various densities. At the nearly zero foam density, both predictions of the Poisson's ratio approached 0.5. While Warren's predictions decreased monotonically with the increase of the density, the present prediction kept constant, or slightly increased, except at the low-density range where the Poisson's ratio changed rapidly. However, note that the moduli by the Warren's method were calculated with the formula for low-density foams and were extrapolated to the high-density range. Therefore, we can conclude that the Poisson's ratio of the polyurethane foam was dominated by the bending behavior at low-density range, but became influenced by the axial compliance as the density increased.

7.2.3 Results: Carbon Foam with Isotropic Properties

Effective bulk properties of the carbon foam were calculated at various densities. Since the material properties were not well known at the ligament level, the prediction was made

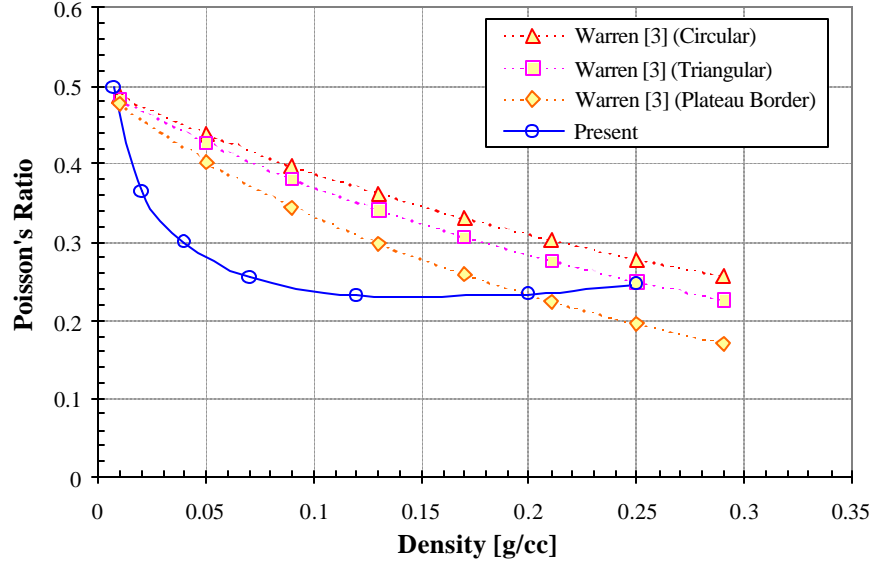


Figure 63. Prediction of Bulk Poisson's Ratio of Polyurethane Foam at Various Densities.

both on the isotropic and anisotropic assumptions on the foam ligament properties. This section first demonstrated the results based on the isotropic assumption. Poisson's ratio was assumed to be 0.33. The density of the carbon material was 1.8 g/cm^3 , assuming the foam was carbonized but not graphitized. Note that since the radius of the bubbles for the open-cell foams was greater than $\sqrt{2}a$, the bulk density of the open-cell carbon foams should be less than 0.398 g/cm^3 .

Effective tensile modulus predicted by the present method as well as those by Warren for the isotropic foams are shown in Figure 64. The Young's modulus of the foam ligament was assumed 15.61 GPa , which was the transverse Young's modulus of a pitch-based carbon fiber, AS4 [43]. Both predictions resulted in quadratic variation of the moduli with the density increment. The present method for the carbon foam agreed well with Warren's prediction with plateau border cross section at a low-density region and with the circular cross section at a high-density region. Note that for the polyurethane foam, the present method yielded the upper bound of Warren's prediction at all ranges of density.

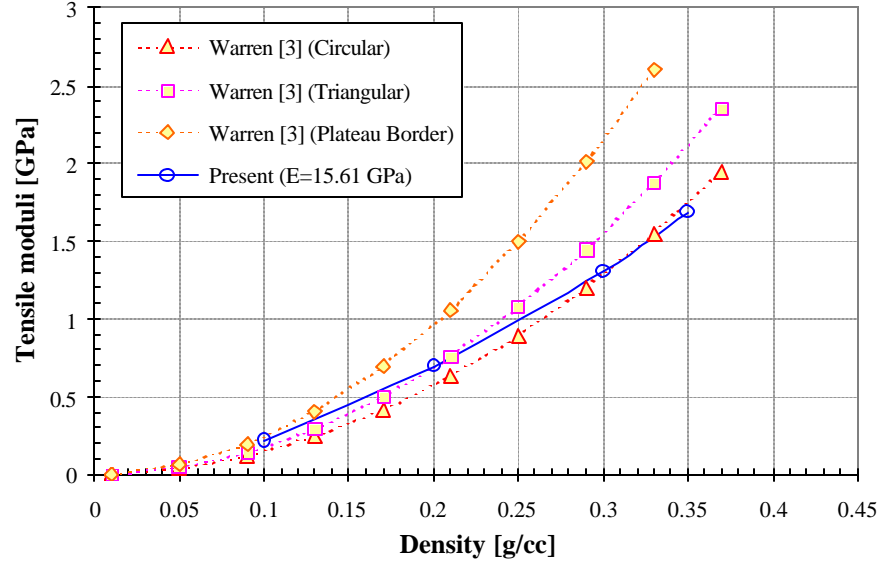


Figure 64. Prediction of Bulk Tensile Moduli of Carbon Foam at Various Densities.

To understand the influence of the ligament properties on the bulk foam properties, the Young's modulus of the foam ligament varied from 7, 20, and 25 GPa, and the corresponding bulk moduli at various densities were plotted in Figure 65. The prediction was compared with limited experimental data measured with MER carbon foam [44]. Figure 65 shows that the present method yielded a fairly reasonable prediction of the effective bulk properties of the carbon foam. Note that the present method can also be utilized to estimate the ligament properties of the foam when the bulk properties were measured by experiments.

Figure 66 shows the predicted Poisson's ratio of the carbon foam at various densities. As in the case of the polyurethane foam, the present method yielded nearly constant values unless the carbon foam was of low density.

7.2.4 Results: Carbon Foam with Anisotropic Properties

Microstructural observation on the carbon foam revealed that the foam ligaments had anisotropic material properties, and the degree of anisotropy varied with foam processes, such as carbonization or graphitization. The isotropic assumption made earlier in this study was

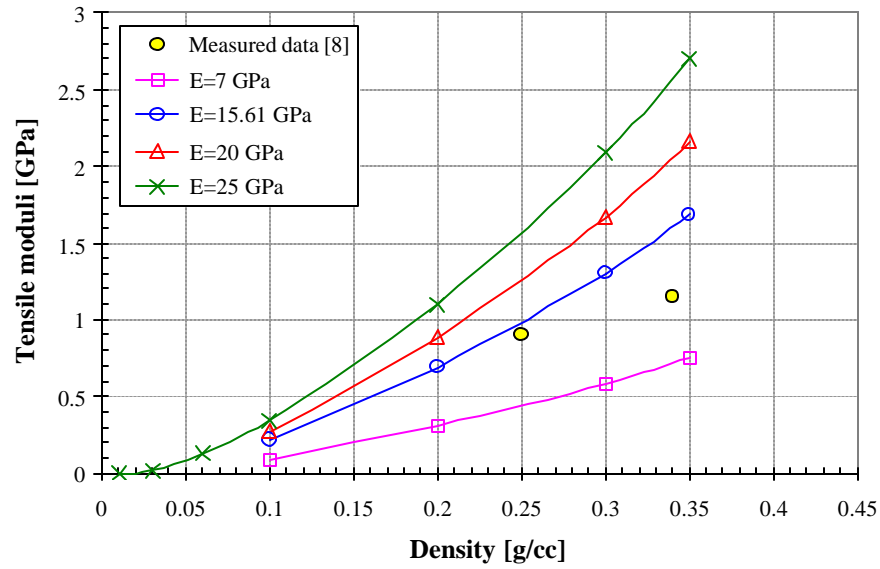


Figure 65. Prediction of Bulk Tensile Moduli of Carbon Foam at Various Densities with Several Assumed Ligament Properties of Carbon Material. The present model was compared with experimental data [44].

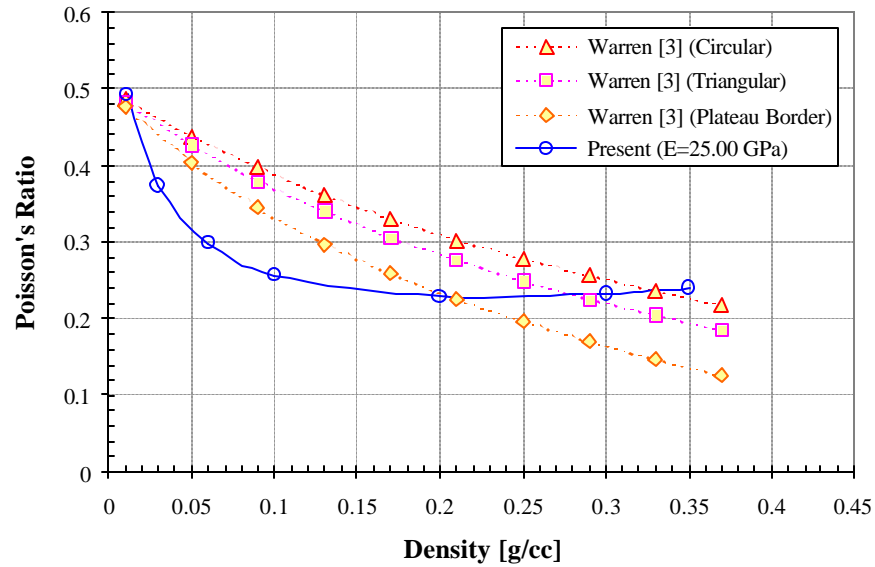


Figure 66. Prediction of Bulk Poisson's Ratio of Carbon Foam at Various Densities.

dropped by varying the properties in the longitudinal and transverse directions parallel and perpendicular to the foam ligament axes, respectively. With the absence of well-known bulk properties of the carbon, several assumptions were made as follows: (1) the foam ligaments possessed transversely anisotropic properties; (2) in-plane and out-of-plane major Poisson's ratios were assumed as $\nu_{12} = \nu_{13} = 0.33$ and $\nu_{23} = 0.5$, respectively; and (3) in-plane (G_{12} and G_{13}) and out-of-plane (G_{23}) shear moduli were calculated by

$$G_{12} = G_{13} = \frac{E_2}{2(1+\nu_{21})} \quad \text{and} \quad G_{23} = \frac{E_2}{2(1+\nu_{23})}, \quad (44)$$

where $\nu_{21} = \nu_{12} E_2 / E_1$.

Effective bulk properties of the carbon foam predicted with the present method at various densities were plotted in Figures 67 through 71. Results with the anisotropic material properties were compared with those with isotropic ones. The bulk moduli of the carbon foam were predicted: (1) when the longitudinal modulus of the ligament was fixed at 200 GPa, while transverse modulus varied from 10 GPa to 40 GPa, and (2) when the transverse modulus was fixed at 20 GPa, while longitudinal modulus varied from 20 GPa to 1000 GPa.

Figure 67 shows that the effective moduli of the carbon foam highly depended on the change of transverse modulus of the foam ligaments. The moduli prediction with the anisotropic ligament properties of $E_1 = 200$ GPa and $E_2 = 20$ GPa yielded similar bulk tensile moduli of the carbon foam with the isotropic ligament property of $E = 25$ GPa. Meanwhile, Figure 68 shows that the change of the longitudinal bulk moduli affected the foam moduli less significantly than the change of the transverse ones as observed in Figure 67. As Figure 69 shows, the rate of increment of the bulk foam moduli decreased as the longitudinal moduli of the ligament increased at all densities. Higher dependency on the transverse moduli of the foam

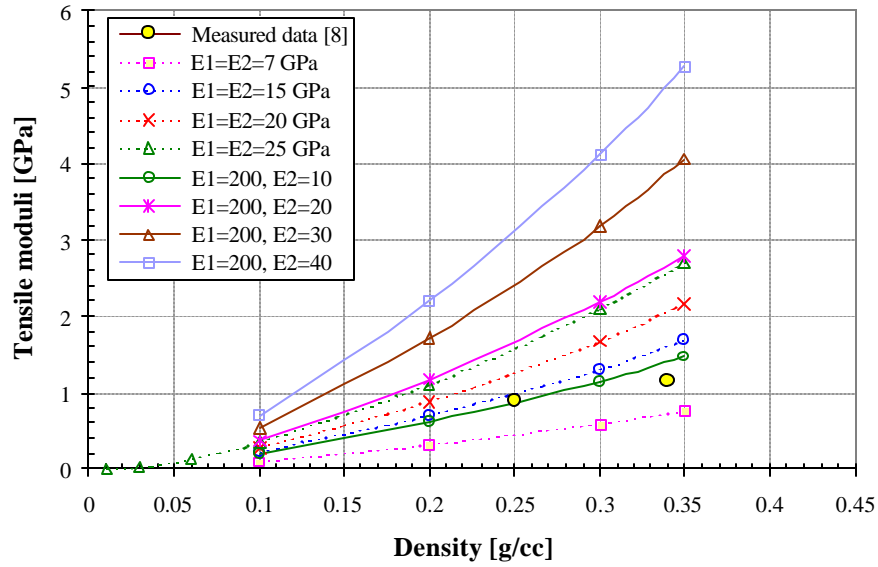


Figure 67. Prediction of Bulk Tensile Moduli of the Carbon Foam Predicted with Isotropic and Anisotropic Properties of Foam Ligaments. Longitudinal modulus of the ligament was fixed at 200 GPa, while transverse modulus varied from 10 GPa to 40 GPa.

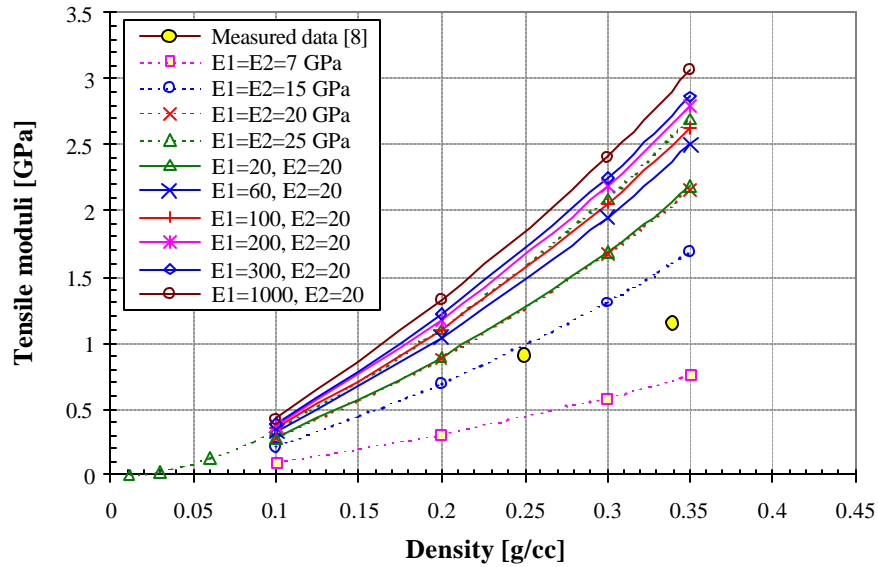


Figure 68. Prediction of Bulk Tensile Moduli of the Carbon Foam Predicted with Isotropic and Anisotropic Properties of Foam Ligaments. Transverse modulus of the ligament was fixed at 20 GPa, while longitudinal modulus varied from 20 GPa to 1000 GPa.

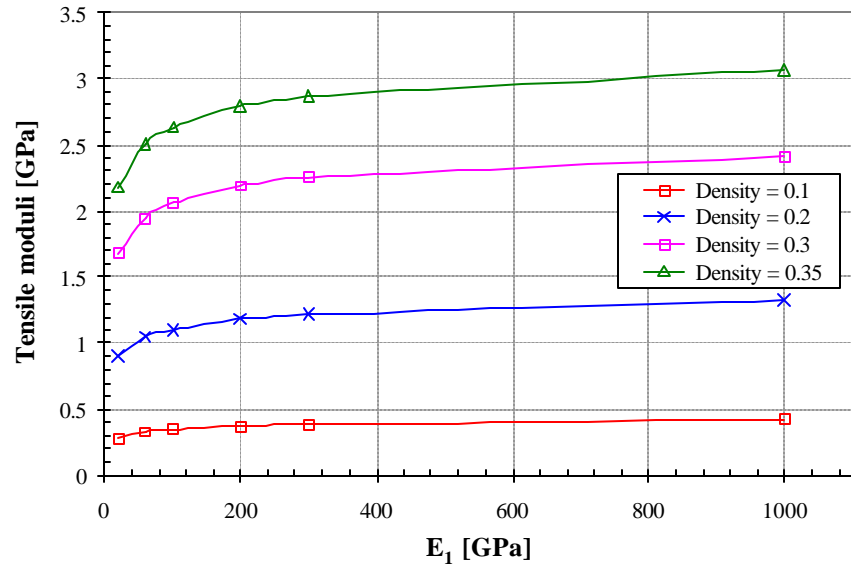


Figure 69. Variation of Bulk Tensile Moduli of the Carbon Foam with the Increase of Longitudinal Modulus of Foam Ligament. Rate of increment in the foam moduli decreased as the longitudinal moduli increased at all densities.

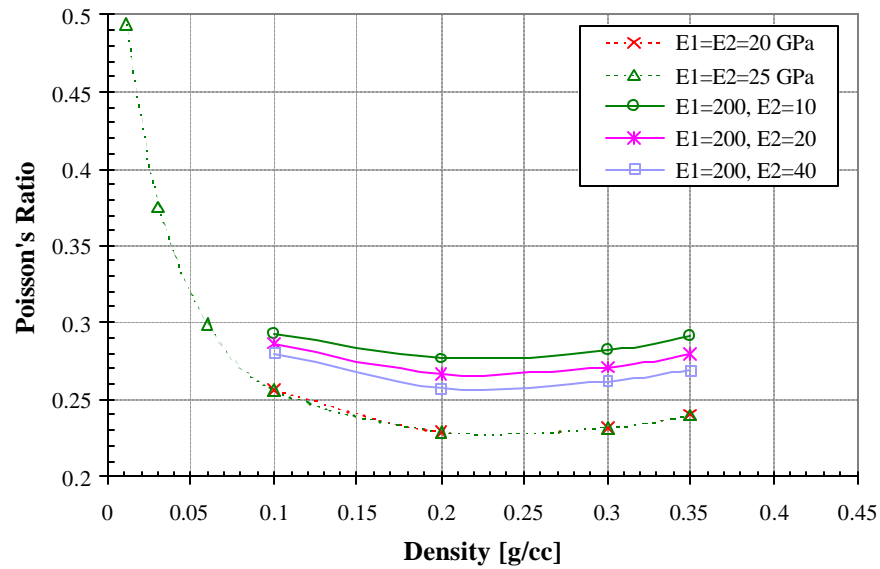


Figure 70. Prediction of Bulk Poisson's Ratio of the Carbon Foam Predicted with Isotropic and Anisotropic Properties of Foam Ligaments. Longitudinal modulus of the ligament was fixed at 200 GPa, while transverse modulus varied from 10 GPa to 40 GPa.

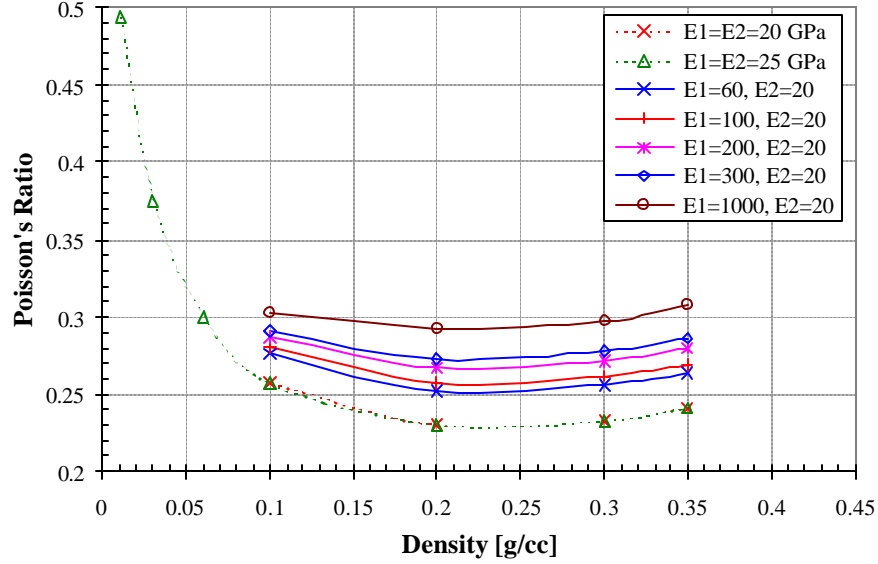


Figure 71. Prediction of Bulk Poisson's Ratio of the Carbon Foam Predicted with Isotropic and Anisotropic Properties of Foam Ligaments. Transverse modulus of the ligament was fixed at 20 GPa, while longitudinal modulus varied from 60 GPa to 1000 GPa.

ligaments than on the longitudinal ones illustrated that the foam ligaments were under not only axial deformation but also significant bending deformation. Furthermore, the bending deformation occurred as a combination of pure bending and transverse shear deformation, which can be explained with Timoshenko's beam theory.

Figures 70 and 71 show the predicted Poisson's ratio of the carbon foam at various densities. As in the case of the isotropic ligament properties, the present prediction yielded nearly constant Poisson's ratios unless the carbon foam was of low density. Unlike the bulk tensile modulus, the Poisson's ratio was dependent on both the longitudinal and transverse moduli of the foam ligament, as shown in both figures.

7.3 SUMMARY AND RECOMMENDATIONS

The emerging ultralightweight material, carbon foam, was modeled with 3-D microstructures to develop a basic understanding of the performance of open-cell foam materials.

To develop a reliable model for the carbon foam, a quantitative microstructural characterization of foam ligaments and nodes should be complemented with the model development.

Because of the randomness and complexity of the microstructure of the carbon foam, the representative cell ligaments were first characterized in detail at the microstructural level. The microstructural characteristics (or properties) were then correlated with the bulk properties through the present model. A series of databases should be collected for various size and spatial orientation of the cell ligaments, as well as the property variation due to the graphitic alignment along the longitudinal direction of the ligaments. The model is thus expected to provide a basis for establishing a process-property relationship and optimizing foam properties.

The present model yielded a fairly reasonable prediction of the effective bulk properties of the foams. The present predictions were compared with the existing simpler model and/or experimental measurement. We observed that the elastic bulk properties of the foams were dominated by the bending behavior at low-density range but became influenced more and more by the axial compliance as the density increased. The prediction indicated that the effective bulk moduli of the carbon foam were dependent more on the transverse modulus of the foam ligaments than on the longitudinal one. The rate of increment in the foam moduli decreased as the longitudinal moduli increased at all densities. Unlike the Young's modulus, the Poisson's ratio was dependent on both the longitudinal and transverse moduli.

8. SCANNING ELECTRON MICROSCOPY INVESTIGATION OF DEFORMATION IN THE VICINITY OF A MODE II CRACK TIP IN UNIDIRECTIONAL TOUGHENED EPOXY COMPOSITES

Delamination-related research on fiber-reinforced composites has attracted considerable interest due to its significant practical importance. Significant differences in deformation patterns in the crack tip vicinity were observed for Mode I and Mode II delaminations and reported by several authors, including [45-47]. A sequence of 45° (with respect to the crack plane) microcracks is believed to form beyond the Mode II crack tip in polymer composites. The propagation of a Mode II crack is believed to be a result of rupture and coalescence of these tension microcracks.

8.1 SPECIMEN PREPARATION

Two types of specimens were utilized for testing. A 24-ply unidirectional miniature specimen (1.4" long and 0.25" wide) was cut out of a standard size (8" long, 1" wide) specimen after a shear crack formed in the course of end notch flexure (ENF) testing. The miniature specimen was cut out so that the end of the shear crack observed in the optical microscope would be halfway between the bottom support and the bending load application point. The material system utilized in the experiment was a toughened carbon epoxy unidirectional composite, IM7/977-3.

The second type of specimen utilized was a sandwich plate with eight-ply IM7/5250-4 face sheets and a 0.017"-thick 828 neat epoxy layer in between. The sandwich plate was manufactured by using 0.005" spacers on each sheet filled with resin and then assembled into the sandwich at room temperature cure. A Teflon tape was inserted between the two assemblies to create a starter crack. The same size specimens (1.4" by 0.25") were cut out from the sandwich

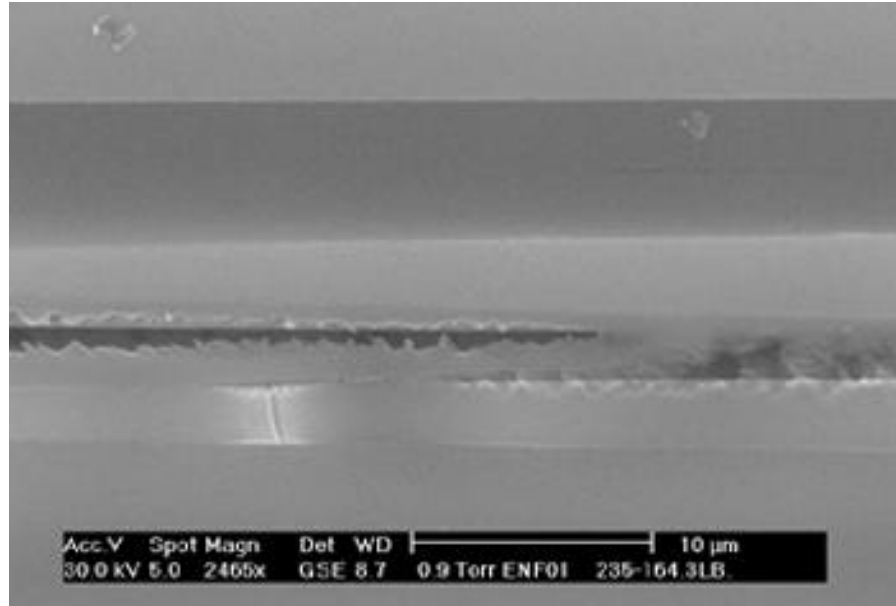
panel so the Teflon tape would end halfway between the bottom support and the bending load application point.

8.2 EXPERIMENTAL PROCEDURE

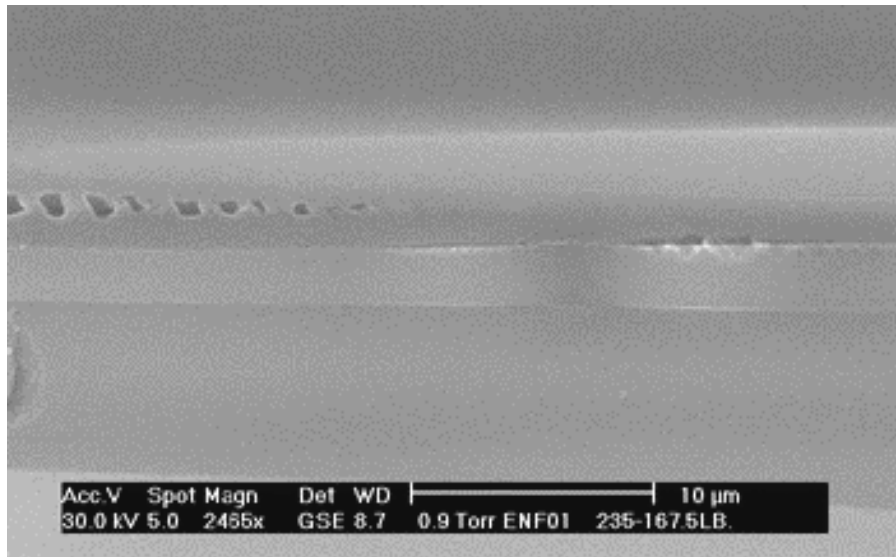
A Philips XL30 environmental scanning electron microscope (E-SEM) was used for testing. A three-point bending fixture with a 1000-lb tensile substage for XL30 E-SEM was used to perform *in situ* ENF tests on miniature specimens described in the previous section. The distance between the lateral supports was 0.8". The load cell was equipped with force and head displacement controller with digital readout. Compressive load was applied to create three-point transverse bending of the specimens.

8.3 RESULTS AND DISCUSSION

First, the 24-ply precracked IM7/977-3 specimen was tested. After setting up the specimen in the SEM, it was loaded in bending until crack extension took place. The examination of the crack tip zone revealed details of deformation patterns, which at first appeared similar to those reported in the literature [45,47]. A typical sequence of 45-degree microcracks was observed in the crack tip area, as shown in Figure 72(a). However, as can be seen in the same figure, the damage has already extended beyond this microcracking area. It appears that the microcracking pattern in this case may be a post-fracture effect when a thin surface layer of polymer remains intact after delamination and then ruptures when the opening displacement increases. To confirm that the shadowed area on the right side of the figure is a delamination, another micrograph was taken at a slightly higher load and shown in Figure 72(b). A clear delamination can be seen on the right side of the figure, confirming that the area ahead of the microcracking in Figure 72(a) was a delamination. The surface layer microcracks ruptured and coalesced but after the Mode II delamination had already propagated.



(a)



(b)

Figure 72. SEM Image of the Mode II Crack Tip Region at Two Consecutive Load Levels.

The behavior observed in the present work can be attributed to the following factors. The resin system utilized in the experiments is a toughened epoxy, which can exhibit very ductile behavior and form surface films behaving as described above. However it is believed that the main difference between the composite tested in the present work and that reported in [45-47] is the absence of the resin-rich area where the Mode II crack propagated in the present study.

A sandwich-type specimen containing Teflon tape to start the interlaminar crack in the resin-rich region was tested next. Figure 73 shows the image of the region inside the resin layer near the end of the Teflon tape under 135 lbs of transverse load with the starter crack just emanating from the edge of the Teflon sublayer. One can observe several fragments of the crack parallel to the face sheet plane. It was determined that the plane of crack propagation coincided with the artificial interface created in the center of the adhesive layer during manufacture of the sandwich. This interface was created by assembling the two face sheets with the 828 resin spread on each face sheet. The shear crack continued to extend under loading up to 186 lb until deflecting from the plane toward the outer layer and forming a cavity, shown in Figure 74(a). The cavity continued to increase [Figure 74(b)]; however, no longitudinal extension of the crack took place. This behavior is consistent with the fact that the transverse shear stress vanishes at the center (under the bending fixture) of the specimen at its midplane. It is also consistent with the crack termination location from specimen to specimen; a total of three replicas were investigated.

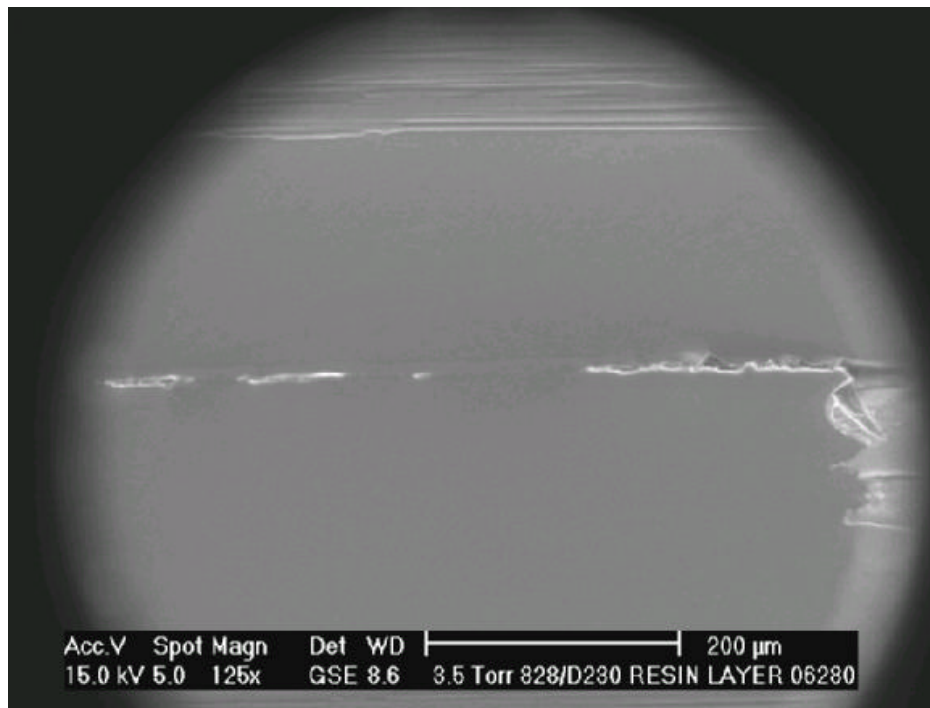
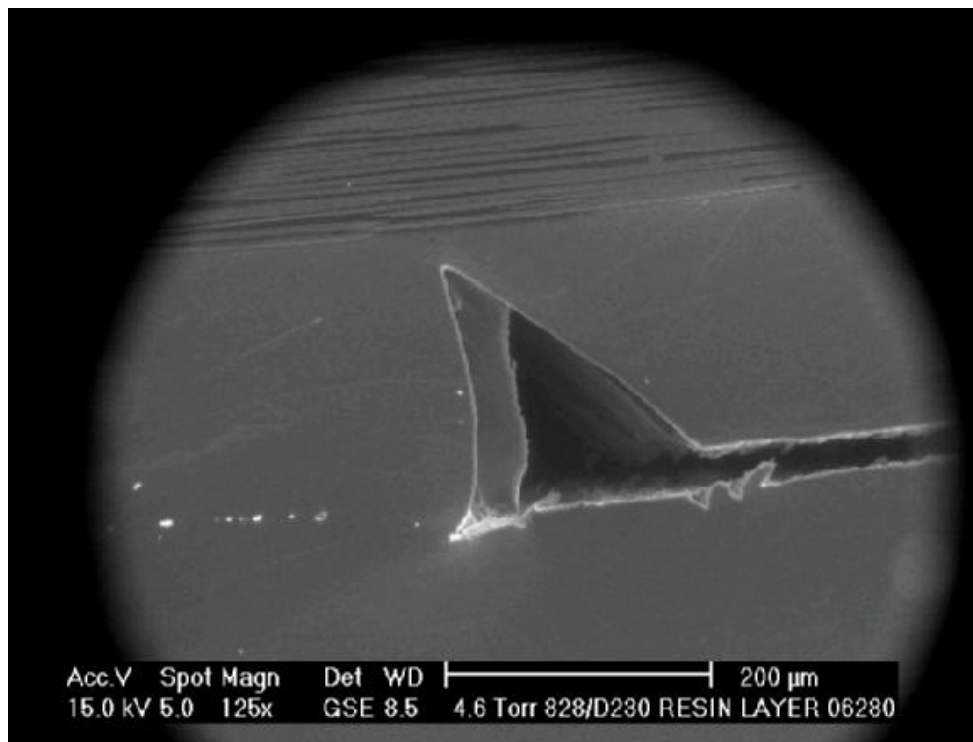


Figure 73. SEM Image of the Mode II Crack Tip Region in the Resin-Rich Region of the Sandwich Specimen.



(a)



(b)

Figure 74. Fully Extended Interlaminar Crack at (a) 186-lb Loading and (b) 226-lb loading.

Further loading led to fiber failure, including compression failure near the inner surface of the lower face sheet, as shown in Figure 75. It is interesting to note that only distributed fiber breakage was observed on the surface of the lower face sheet, which was loaded in tension.

8.4 SUMMARY AND RECOMMENDATIONS

In situ observation of deformation and failure phenomena in advanced composite materials was conducted in a high-resolution Philips XL30 E-SEM. Interlaminar crack tip features were examined in unidirectional fiber-reinforced composites with and without the resin-rich area at the midsurface of the laminate. Face sheet failure was observed in the sandwich plates at relatively small extension of the Mode II crack in the adhesive. Further work is required to investigate the Mode II crack extension mechanism in a resin-rich region.

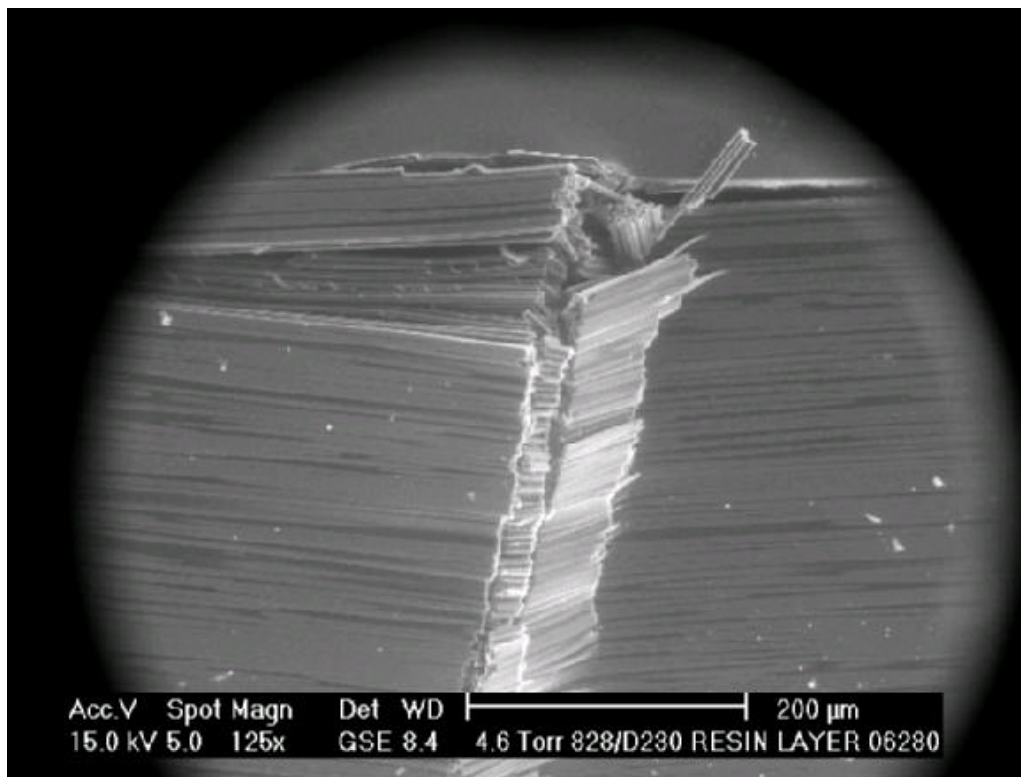


Figure 75. Compression Fiber Failure on Inner Surface of the Bottom Face Sheet at 226-lb Load.

9. NONLOCAL MODELS OF STRESS FIELD CONCENTRATIONS AND EFFECTIVE THERMOELASTIC PROPERTIES OF RANDOM STRUCTURE COMPOSITES [48]

In this section we consider a linearly thermoelastic composite medium, which consists of a homogeneous matrix containing a statistically homogeneous set of ellipsoidal inclusions. The multiparticle effective field method (MEFM) (see for reference [49]) based on the theory of functions of random variables and Green's functions is used. Within this method a hierarchy of statistical moment equations for conditional averages of the stresses in the inclusions is derived. The hierarchy is established by introducing the notion of an effective field. In this way the interaction of different inclusions is taken directly into account in the framework of the homogeneity hypothesis of the effective field. Combining the MEFM with the standard scheme of the iteration method (IM) and Fourier transform method (FTM) permits one to obtain the explicit representations for the nonlocal integral and differential operators, respectively, of any order describing overall effective properties as well as the stress concentrator factor in the components. It is shown that the reduction of the integral operator to the differential one for sufficiently smooth statistical average stress fields is superior to the FTM. After some additional assumptions the method proposed is reduced to the perturbation method as well as to the quasicrystalline approach. For some concrete numerical examples, one can demonstrate the advantage of the IM over the FTM.

The prediction of the behavior of composite materials by the use of mechanical properties of constituents and their microstructure is a central problem of micromechanics, which is eventually reduced to the estimation of stress fields in constituents. A considerable number of methods are known in the linear theory of statistically homogeneous composites being considered in this paper which yield the effective elastic constants and stress field averages in the

components. Appropriate, but by no means exhaustive, references are provided by the reviews [48,50]. When the statistical average stress in a composite medium varies sufficiently slowly compared to the size scale of the microstructure (i.e., roughly speaking, the separation of the external and internal scales takes place), the material macroscopically behaves as a homogeneous body with some effective moduli, which can be estimated by the different methods referred to above. If the condition of the separation of scales summarized above is not valid, the material's response cannot be adequately described in the framework of the local theory of elasticity for the homogeneous medium.

For the analysis of the widely separated scales (but not too widely), a number of phenomenological approaches have been proposed to enhance the continuum model by nonlocal terms, either introduced through an integral equation or through an additional gradient equation based on the assumption that the forces between material points can be long range in character (see for reference [48]). The different modifications of these phenomenological constitutive relations were used for the analyses of various size effects, such as strain gradient hardening, size effect in torsion and indentation, strain gradient plasticity, and nonlocal damage mechanics.

The micromechanical models are used to answer a fundamental question of how length scales in the effective constitutive equations could be directly derived from the geometrical and mechanical properties of constituent phases. It is known that the eventual abandonment of this hypothesis of statistically homogeneous fields leads to a nonlocal coupling between statistical averages of the stress and strain tensors when the statistical average stress is given by an integral of the field quantity weighted by some tensorial kernel, i.e., the nonlocal effective elastic operator. Analysis of highly contrasted statistically homogeneous media is simplified for sufficiently smooth external loading permitting the use of the Taylor expansion for the statistical

average of a stress field and the application of an FTM. In so doing the initial integral equation is reduced to an algebraic polynomial equation with constant coefficients in a Fourier space with forthcoming solution and the implementation of the inverse Fourier transform. The scheme summarized informally above is usually based on the hypothesis of the homogeneity of the effective field in which each particle is located. The quasicrystalline approximation by Lax is often used for truncation of the hierarchy of integral equations involved, leading to neglect of direct multiparticle interactions of inclusions. This reduced the analysis to the use of statistical information of up to two-point correlation functions and allowed one to derive explicit relations for the nonlocal overall differential operator by the different methods: by the effective field method or by the method of conditional moments (see for reference [48]).

The main disadvantage of the quasicrystalline approximation, consisting of the neglect of direct multiparticle interactions of inclusions, was overcome recently by the MEFM (references may be found in the survey [49]). The MEFM is based on the theory of functions of random variables and Green's functions. Within this method a hierarchy of statistical moment equations for conditional averages of the stresses in the inclusions is derived. The hierarchy is established by introducing the notion of an effective field. In this way the interaction of different inclusions is taken directly into account in the framework of the homogeneity hypothesis of the effective field. Combining the MEFM with the standard scheme of the FTM usually used for the analysis of the statistically inhomogeneous stress fields allowed (see [51,52]) to obtain the explicit representation of a nonlocal overall operator in the form of the second-order differential operator. The author [53] estimated the nonlocal integral operator of the overall constitutive equation for periodic structure composites by the use of the first iteration of the IM and showed the reduction of the integral operator obtained to the differential operator involved derived by the FTM.

The last approach is generalized in this report for the analysis of statistically homogeneous random structure composites. By the use of the IM and FTM, one obtains the explicit representations for the nonlocal integral and differential operators, respectively, of any order describing overall effective properties as well as the stress concentrator factor in the components. We show the reduction of the integral operator to the differential one for sufficiently smooth statistical average stress fields. After some additional assumptions the method proposed is reduced to the perturbation method as well as to the quasicrystalline approach. In some concrete numerical examples, one demonstrates the advantage of the IM over the FTM.

9.1 THE GENERAL SCHEME

Let a linear elastic body occupy an open-bounded domain with a smooth boundary and contain a homogeneous matrix and a statistically homogeneous set X of ellipsoidal inclusions v_i . It is assumed that the inclusions can be grouped into components (phases) $v^{(k)}$ with identical mechanical and geometrical properties (such as the shape, size, orientation, and microstructure of inclusions). For the sake of definiteness, in the 2-D case we will consider a plane-strain problem. At first no restrictions are imposed on the elastic moduli $L(\mathbf{x})$ of phases.

To simplify the exact infinite system of integral equations obtained, we now apply the main hypothesis of many micromechanical methods, the approximation called the effective field hypothesis:

- H1)** Each inclusion v_i has an ellipsoidal form and is located in the homogeneous effective field which is found from self-consistent estimations.
- H2)** For a sufficiently large number of interacting inclusions n , the effective fields acting on the n and $n+1$ inclusions coincide.

The fundamental differences of hypothesis **H2** and the quasicrystalline approximation by Lax were discussed. According to hypothesis **H1** and in view of the linearity of the problem, there exist constant fourth- and second-rank tensors describing the average response of n inclusions subjected to the effective field.

Then the infinite system of integral equations can be reduced to single integral equations

$$\langle \mathbf{S} \rangle_i = \mathbf{Y} \mathbf{S}^{\text{average}} + \mathbf{K} \langle \mathbf{S} \rangle_i, \quad (45)$$

for statistical average of stresses in the inclusions $\langle \mathbf{S} \rangle_i$, where \mathbf{Y} is a tensor and \mathbf{K} is an integral operator.

Thus we reduced the infinite system of integral equations to the standard form of operator Eq. (45) with the regular integral kernel of convolution type that can be solved by such known methods as the method of mechanical quadratures, successive approximations, and FTM.

Application of the method of mechanical quadratures is very popular, although it is required to solve a linear system of very high order even for a smoothly varying load. Because of this, at first we will solve Eq. (45) by the method of successive approximations, which is also called the Neumann series method. Their connection with the FTM is considered in [48].

The IM is based on the recursion formula,

$$\langle \mathbf{S} \rangle_i^{(k+1)} = \mathbf{Y} \mathbf{S}^{\text{average}} + \mathbf{K} \langle \mathbf{S} \rangle_i^{(k)}, \quad (46)$$

to construct a sequence of functions $\langle \mathbf{S} \rangle_i^{(k)}$ that can be treated as an approximation of the solution of Eq. (45). In effect the IM (Eq. 46) transforms the integral equation problem (Eq. 45) into the linear algebra problem in any case. Usually the driving term of this equation is used as an initial approximation.

Now we will consider the FTM. One assumes that the statistical average of stress polarization tensor belongs to the class of m times continuously differential functions. Since we

desire an explicit representation for the stress concentrator factor, we will approximate stresses by the first terms of its Taylor expansion and reduce Eq. (45) to the following symbolic equation:

$$\mathbf{R}(\mathbf{x},?) \langle \mathbf{S} \rangle_i(\mathbf{x}) = \mathbf{S}^{\text{averaged}}(\mathbf{x}). \quad (47)$$

The operator $\mathbf{R}(\mathbf{x},?)$ is a linear partial differential operator with the constant coefficients for statistically homogeneous media. Considering that Eq. (47) is a differential equation with constant coefficients, the method of solution that first comes to mind is using the FTM to transform the differential problem of solving Eq. (47) into the division problem of solving the multiplicative equation. Then the solution of Eq. (47) is represented by the differential operator

$$\langle \mathbf{S} \rangle_i(\mathbf{x}) = \mathbf{Q}(?) \mathbf{S}^{\text{averaged}}(\mathbf{x}), \quad (48)$$

where an explicit form of the differential operator $\mathbf{Q}(?)$ of an infinite order is presented in [48].

We obtained the representations of integral and differential operators of an infinite order for the stress concentrator factors as well as for the effective thermoelastic properties. The relations obtained were simplified for some particular cases such as weakly inhomogeneous media as well as the quasicrystalline approximation. We demonstrated the reduction of integral operators to the differential ones.

9.2 NUMERICAL RESULTS

Just for demonstration of the comparison of available experimental data with the predicting opportunity of the method proposed, we will consider the zero-order approximation of the method that is the estimation of the effective elastic moduli \mathbf{L}^* . Assume the matrix is epoxy resin ($k^{(0)}=4.27$ GPa and $\mu^{(0)}=1.53$ GPa) which contains identical circular glass fibers ($k^{(1)}=50.89$ GPa and $\mu^{(1)}=35.04$ GPa). Two alternative radial distribution functions $g(r)$ of inclusion distribution will be examined: the step function and the function proposed in [54] that takes into account a neighboring order in the distribution of the inclusions. As can be seen in Figure 76, the

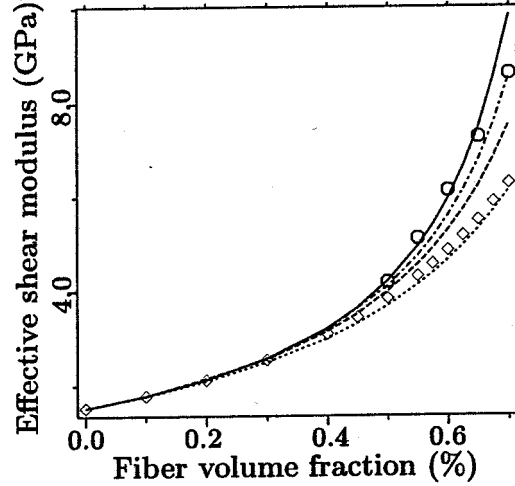


Figure 76. Variation of the Effective Shear Modulus m^* as a Function of a Concentration of the Inclusions c . Experimental data (circles) and curves calculated by MEFM and nonstep function $g(r)$ (solid line), MEFM and step function $g(r)$ (dot-dashed line), perturbation method and nonstep $g(r)$ (dashed line), perturbation method and step function $g(r)$ (diamonds), Mori-Tanaka approach (dotted line).

use of the approach based on the quasicrystalline approximation [also called Mori-Tanaka (MT) approach] leads to an underestimation of the effective shear modulus by 1.85 times for $c=0.7$ compared to the experimental data as well as to the more exact approximation of the MEFM, which provides the best comparison with experimental data (see [55]). It should be mentioned that the estimations by the MEFM are slightly sensitive to the choice of the radial distribution function g . It was observed that the proposed formulation compared well with experimental data for c up to 65 percent; for fiber volume fractions greater than 70 percent, microdefects existing in experimental specimens may significantly affect the overall elastic moduli. At the same time, the MT solution differs from the perturbation method approximation by not more than five percent for the concentration of the inclusions $c < 0.7$ and does not depend on the radial distribution function (in contrast to the perturbation method).

Our approach to addressing this section will be to employ the nonlocal equations for stress concentrator tensors we derived in the previous sections by the IM and FTM. We will consider

ensemble-averaged stresses, and determine the stress concentrator factors at the inclusions by the IM and, in some particular cases, by the FTM. The quantitative results we obtain will be for the 2-D case (plane strain problem) for the two-phase composites consisting of an isotropic matrix reinforced by a random dispersion of isotropic identical circle particles.

Let us now demonstrate the application of the theoretical results by considering an isotropic composite made of an incompressible isotropic matrix filled with rigid circle inclusions of one size. This example was chosen deliberately because it provides the maximum difference of predictions of effective elastic response estimated by various methods, and was considered by a number of authors. We shall consider the response for a normal loading that varies with position in its loading direction $\langle s_{ii} \rangle = f(x_I) d_{Ii} d_{Ij}$ with three specific cases of the functions

$$f_1(x_I) = \sin(\pi x_I/4), \quad (49)$$

$$f_2(x_I) = 0.6579 |x_I|^{2.001} e^{-0.2422 x_I^2}, \quad (50)$$

$$f_3(x_I) = 0.6584 |x_I|^{1.999} e^{-0.2422 x_I^2}, \quad (51)$$

$$f_4(x_I) = 0.6580 x_I^2 e^{-0.2420 x_I^2}. \quad (52)$$

The loading with f_1 belonging to $C^8(R)$ was analyzed by the FTM in detail for the different arguments and the different concentrations of the spherical inclusions. We can only define the m -th derivatives of the functions $f_j(0)$ ($j=2,3$) if $f^{(m)}(-0) = f^{(m)}(+0)$. Now f_2 belongs to C^2 and f_3 belongs to C^1 , and the third and the second derivatives do not exist for the functions f_2 and f_3 , respectively. The functions f_j ($j=2,3,4$) have approximately the same maximum, and the same maximum of their first derivatives, as the function f_1 (see Figure 77). In so doing, independently from the concrete micromechanical average scheme, the FTM will predict zero nonlocal effects at the point 0 for the function $f_2(x_I)$. Analogous analysis leads to a more dramatic conclusion for the function

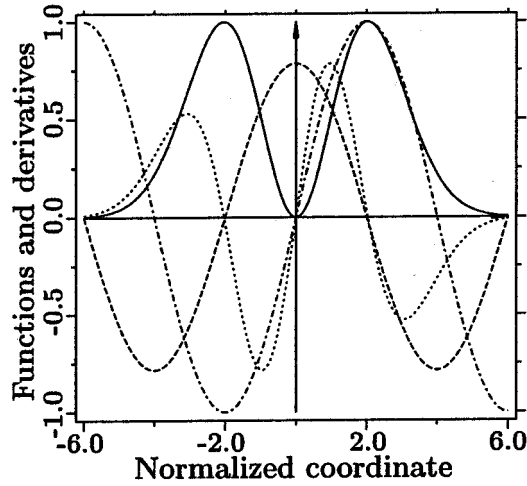


Figure 77. The Functions and their First Derivatives versus Argument x_1 : $f_2(x_1)$ (solid line), $f_1(x_1)$ (dot-dashed line), $f_1'(x_1)$ (dashed line), $f_2'(x_1)$ (dotted line).

f_3 , that is, the FTM cannot be applied in principle to the field described by f_3 because the differentiable function $f_3(x_1)$, which is very close to $f_2(x_1)$, is not twice differentiable at $x_1=0$.

The comparative results estimated by the MEFM for the nonstep radial distribution function and for different functions f_i ($i=1,2,3,4$) for the 0th and 7th iterations are presented in Reference [48]; the results for functions f_i differ from one another by less than one percent.

The first few iterations of estimations of stresses for the function f_2 are presented in Figure 78. As can be seen, a few order approximations of the IM lead to significantly different normalized stresses provided by the derivatives $f^{(m)}$ (if they exist), whereas the second-order approximation of the FTM leads to the degenerate results.

In [48] only the function f_2 is analyzed in the framework of the iteration scheme. The comparative analysis of the MEFM, MT method, and the perturbation method for the different radial correlation functions is presented. As is shown, the MEFM is most sensitive to the choice of radial distribution function and leads to the maximum nonlocal effects predicted. It is

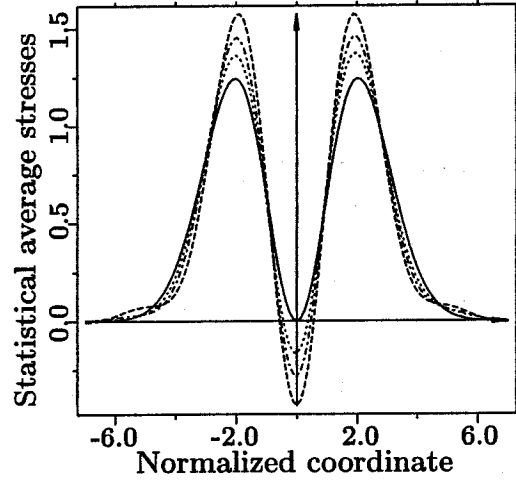


Figure 78. The First Few Iterations of Statistical Averages $\langle s_{11} \rangle_i(x_1)$ versus x_1 Estimated for the Functions $f_2(x_1)$ and Nonstop $g(r)$ by the MEFM. Zero-order (solid line), first-order (dotted line), second-order (dot-dashed line), seventh-order (dashed line) approximations.

interesting that nonlocal response, in contrast to the local one estimated by the MT method, depends on the radial distribution function $g(r)$.

9.3 SUMMARY AND RECOMMENDATIONS

Let us discuss the main scheme as well as the short sketch of limitations and of possible generalization and application of the methods proposed.

The obtained relations depend on the values associated with the mean distance between inclusions, and do not depend on the other characteristic size, i.e., the mean inclusion diameter. This fact may be explained by the initial use of hypothesis **H1** dealing with the homogeneity of the effect inside each inclusion. In the case of a variable representation of the effective field, for instance, in polynomial form, the mean size of the inclusions will be contained in the nonlocal dependence of microstresses on the average stress. Such an improvement based on the abandonment from the hypothesis **H1** was schematically considered in [49].

It should be mentioned that the IM and the FTM have a series of advantages and disadvantages, and it is crucial for the analyst to be aware of their range of application. The IM has two known drawbacks. First, the Neumann series ensures the existence of solutions to integral equations of the second kind only for sufficiently small kernels involved, and second, in general, it cannot be summed in closed form. Of course Eq. (45) can be solved directly by the quadrature method even if the condition of smallness of the kernels is not valid. However, strongly inhomogeneous problems may lead to much larger numbers of quadrature points, making iteration potentially worthwhile. Moreover, increasing the problem dimensionality (from 2-D to 3-D) raises the number of nodes to the dimensional power, and the situation changes radically. As was shown, only a few iterations are necessary; these iterations prove very much faster than a direct inversion of the nonlocal operator by the quadrature method.

The reduction of integral operators to the differential ones allows an understanding of drawbacks of the FTM. The first one is that for obtaining an m -order differential operator, it is necessary that $\mathbf{s}^{\text{average}}$ belongs to C^m . In so doing, the IM providing the accuracy of differential operator of an infinite order does not have even continuity of $\mathbf{s}^{\text{average}}$, since integration is a smoothing operation and the right-hand-side integral (Eq. 45) is likely to be a rather smooth function even when $\mathbf{s}^{\text{average}}$ is very jagged. However, even the m -th approximation of the IM contains the differential operators of infinite orders that are lost in the FTM. The question of the convenience of using one method over another is solved also in favor of the IM, because in the FTM it is necessary to calculate the cumbersome tensors and completeness of estimation, which increases dramatically with m , while in the IM it is enough to estimate a single tensor and consecutively to apply the recursion scheme (Eq. 46), the completeness of which does not depend on the iteration number. Thus, the single advantage of the FTM comprised of obtaining

analytically explicit relations dwindle in light of the disadvantages mentioned above, such as a requirement of smoothness of $\mathbf{s}^{\text{average}}$ belongs to C^m , and the intricacy of analytical calculations. We indicated only mathematical and computational difficulties in the use of the FTM, which can be solved, at least in principle, at a cost of great efforts if the analytical solution is necessary.

However, it should be mentioned that there is an extremely important class of micromechanical problems for statistically inhomogeneous media (such as functionally graded and clustered materials), analysis of which by the FTM is questionable in principle. The breakdown of the assumption of statistical homogeneity leads to the inequality $\mathbf{Y}(\mathbf{x}) \neq \text{const}$. Then the average stresses are not a constant. However, even this simplest case of homogeneous boundary conditions leads to a fundamental prohibitive obstacle against the use of the FTM. Indeed, the inhomogeneity of average stresses yields the fact that the linear differential operator (Eq. 47) has variable coefficients. Then the jump from Eq. (47) to Eq. (48), respectively, based on the properties of the Fourier transform, is difficult, and an applicability of the FTM is questionable. In so doing, the use for statistically inhomogeneous media of the IM inserts requires slight modification of the scheme presented [Eqs. (45) and (46)] (see, e.g., [49]) for application of the IM for research of periodic graded composites). However, the analysis of these problems is beyond the scope of the current study and will be considered in forthcoming publications by the authors.

10. MICROMECHANICS OF NONLOCAL EFFECTS IN GRADED MATERIALS

A considerable number of methods are known in the linear theory of statistically homogeneous composites; appropriate, but by no means exhaustive, references are provided by the reviews [49,50]. Significantly less research has been performed for *statistically inhomogeneous* composites. In such a case, the ergodicity fails, and ensemble and averages do not coincide. The degenerate case of this material is a random matrix composite bonded in some directions as well as the composite medium for which the inclusions are located in a region bonded in some directions, although unrestrictedness of the domain of inclusion locations does not preclude statistical inhomogeneity. For example, any laminated composite material randomly reinforced by aligned fibers in each ply is a statistically inhomogeneous material. The authors [56] proposed statistical descriptions for particulate, statistically inhomogeneous two-phase random media by the use of the theory of a general Poisson process and estimated for some simulated fully penetrable (Poisson distribution) spheres the canonical n -point microstructure function, the nearest-neighbor function, and the linear-path function that, unlike the homogeneous case, will depend on the absolute positions of their argument.

The concept of clusters is similar to that of fractal structures, and the role of statistical descriptor can be treated by such parameters as cluster size, fractal dimension, and the radius of gyration. Even though these and some other parameters are used for the identification of clustered structures, it is not sufficient to predict the overall properties of composites due to several reasons. The first one is that these parameters are not complete enough for the characterization of the micromorphology of fillers simply because one can present other morphology with the same descriptors. More informative characteristics of the random configurations use statistical second-order quantities, which examine the association fillers

relative to other particles in an immediate local neighborhood of the reference filler. Another reason is that the prediction of mechanical properties requires one or another micromechanical model. Advanced micromechanical models normally use two different sorts of statistical descriptors such as n -point probability density and an alternative descriptor of location of m inclusions with the centers $\mathbf{x}_1, \mathbf{x}_2, \dots, \mathbf{x}_m$ described by the probability density $\mathbf{j}_m(\mathbf{x}_1, \mathbf{x}_2, \dots, \mathbf{x}_m)$.

The interest in one or another cluster shape is defined by the physical problem being considered. If the problem is recrystallization or residual stresses, it is reasonable that the important clusters have a convex shape. If one is concerned by the damage properties of dielectric breakdown, a long chain of broken or conducting particles forming a percolating network can be more deleterious than the same number of particles arranged in a convex cluster. For chain clusters, not only the local density of particles but also their arrangement is relevant that are demonstrated as in a limiting case in a concept of weakest link. Due to the numerous possible cluster configurations and limited opportunity of prediction models, we will consider the degenerate case of cluster materials that, nevertheless, has wide applications. Namely, we will analyze so-called ideal cluster materials (see, e.g., [57]) that contain either finite or infinite, deterministic or random ellipsoidal domains called particle clouds distributed in the composed matrix. In so doing the concentration of particles is a piecewise and homogeneous one within the areas of ellipsoidal clouds and composed matrix. In particular, in this section we consider a single particle cloud with the shape of a thick ply located in an infinite matrix with zero concentration of particles. The ideal cluster configuration may be created by distributing cloud centers deterministically or randomly and placing offspring points randomly and uniformly around parent points within a predetermined area. For a description of the cluster arrangement, the notion of cluster radius is used for the presentation of a cluster as a particle of the second

generation with the radius defined by the average distances between the particles. Usually the cluster covers 80 to 90 percent of the total volume of the sphere with the cluster radius.

In many cases, the spatial arrangement of the fibers is neither uniformly random nor periodic. For a statistical description of the microstructure of ceramic matrix composites containing fiber-rich and fiber-poor regions that have a laminated structure, the authors [58] have proposed the so-called strip model. The key parameters of the strip model are the number of densities of fiber in the fiber-poor and fiber-rich regions, the widths of some fiber-poor and fiber-rich regions, and the global number of densities of the fibers is defined by the averaging of these parameters. Thus, the number of densities in a strip model is described by a piecewise constant function. Generalization of this model is based on the introduction of a variable number of densities $n(x_2)$, defined as the average number of disk centers per unit in a thin ply parallel to the axis $x_2=0$.

In this section we consider a linearly elastic composite medium, which consists of a homogeneous matrix containing statistically inhomogeneous, so-called graded random field of inclusions. For functionally graded materials, when the concentration of the inclusions is a function of the coordinates, the micromechanical approach is based on the generalization of the MEFM, previously proposed for statistically homogeneous random structure composites by the author (see for reference and details [49]). The nonlocal integral effective operator of elastic effective properties is estimated. The nonlocal dependencies of the effective elastic moduli, as well as of conditional averages of the strains in the components, on the concentration of the inclusions in a certain neighborhood of points considered are detected.

10.1 GENERAL SCHEME OF THE APPROACH PROPOSED

The trivial generalization of the approach presented by Eq. (45) leads to the estimation of statistical average of strains inside the inclusions as well as the effective properties:

$$\langle \mathbf{s} \rangle_i(\mathbf{x}) = \mathbf{Y}(\mathbf{x}) \mathbf{s}^{\text{average}}(\mathbf{x}) + \mathbf{K}(\mathbf{x}) \langle \mathbf{s} \rangle_i. \quad (53)$$

The relations are the first-order approximation of the nonlocal theory. The construction of the next approximation is obvious. Only at first glance, Eq. (53) is equivalent to the corresponding ones obtained for global effective properties. The main difference is that $\mathbf{Y}(\mathbf{x})$ and, therefore, $\mathbf{L}^*(\mathbf{x})$ depend on the parameters of the inclusion distribution not only at the point \mathbf{x} , but also in a certain neighborhood of that point leading to a so-called nonlocal effect, though, of course, the effective parameters $\mathbf{L}^*(\mathbf{x})$ are the local ones in the sense of the nonlocal elasticity theory. The diameter of this region mentioned above is estimated as three times the characteristic dimension of the inclusions. As a result, a statistically inhomogeneous composite medium behaves like a macroscopically inhomogeneous medium with local effective modulus $\mathbf{L}^*(\mathbf{x})$ determined for a nonlocal distribution of the inclusions in a certain neighborhood of the point considered.

10.2 PREVIOUS NUMERICAL RESULTS

Let us consider a strip model of ideal fiber cluster with probability densities $j_1(\mathbf{x})=n$ and $j_2(\mathbf{x}_1/\mathbf{x}_2)=ng(|\mathbf{x}_1-\mathbf{x}_2|)$ inside the thick ply $|\mathbf{x}|<a_w$ and 0 otherwise. We will consider the fiber volume fraction inside the ply $c=0.65$, and two radial distribution functions $g(r)$ (step and nonstep [54] functions). The neglect of the binary interaction of inclusions for statistically homogeneous medium $n(\mathbf{x})=\text{const.}$ reduces the formula for the effective elastic moduli to the analogous relation obtained by the MT method which is invariant to the $g(r)$. Assume the matrix is epoxy resin ($k^{(0)}=4.27$ GPa and $\mu^{(0)}=1.53$ GPa) which contains identical circular glass fibers ($k^{(1)}=50.89$ GPa and $\mu^{(1)}=35.04$ GPa). As can be seen in Figure 79, the use of the approach based on the

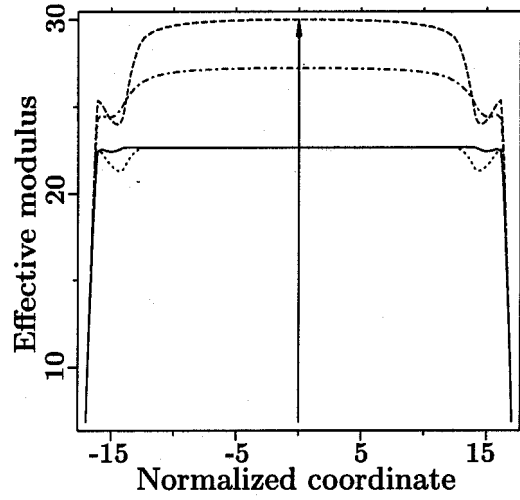


Figure 79. Variation of the Effective Modulus L_{2222}^* as a Function of a Coordinate x_2 Estimated by: MEFM and Nonstep Function $g(r)$ (dashed line), MEFM and Step Function $g(r)$ (dot-dashed line), MT and Nonstep $g(r)$ (dotted line), MT and Step Function $g(r)$ (dotted line).

quasicrystalline approximation (also called the MT approach) leads to an underestimate of the effective moduli L_{2222}^* , compared to the more exact approximation of the MEFM which provides a good comparison with experimental data for statistically homogeneous media (see Figure 76). The distribution $L^*(x) = L^*(x_2)$ was used for estimation of statistical average stresses inside the ply $\langle S \rangle(x)$ by FEA. The stress concentrator factors found at the previous local evaluations permit one to estimate the stresses in the inclusions $\langle S \rangle_i(x_2)$ (see Figure 80).

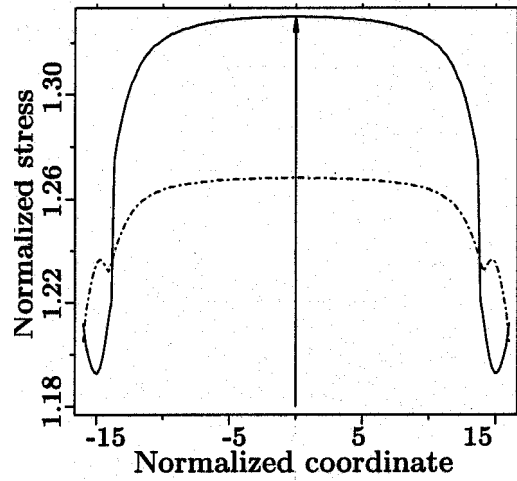


Figure 80. Variation of Statistical Average Stresses Inside the Inclusions $\langle S_{22} \rangle_i(x_2)$ (solid line) and $\langle S_{12} \rangle_i(x_2)$ (dot-dashed line) for the External Loading at the Infinity $S_{ij}^g = d_{i2}d_{j2}$ and $S_{ij}^g = d_{i1}d_{j2}$, respectively, and a Step Function g .

11. QUANTITATIVE DESCRIPTION AND NUMERICAL SIMULATION OF RANDOM MICROSTRUCTURES OF COMPOSITES AND THEIR EFFECTIVE ELASTIC MODULI [59]

A digital image processing technique is used for measurement of centroid coordinates of fibers with forthcoming estimation of statistical parameters and functions describing the stoichiastic structure of a real fiber composite. Comparative statistical analysis of the real and numerically simulated structure was performed. Accompanying known methods of the generation of random configurations by the random shaking procedure allows creation of the most homogenized and mixed structures that do not depend on the initial protocol of particle generation. We consider a linearly elastic composite medium, which consists of a homogeneous matrix containing a statistically homogeneous set of ellipsoidal inclusions. The MEFM (see for reference [49]), based on the theory of functions of random variables and Green's functions, is used for demonstration of the dependence of effective elastic moduli of fiber composites on the radial distribution functions estimated from the real experimental data as well as from the ensembles generated by the method proposed.

The quantitative description of the microtopology of heterogeneous media – such as composite materials, porous and cracked solids, suspensions and amorphous materials – is crucial in the prediction of overall physical properties of these materials. After many years of comprehensive study by direct measurements and empirical relations that is extremely laborious, the structure of microinhomogeneous materials is not completely understood. Computer simulation of topologically disordered structures by the random packing of hard spherical particles in 2-D and 3-D cases has a long history originated in the theory of liquids. This problem is closely connected with the known fundamental problem of statistical physics – description of the behavior of the particle system with the interaction potential of hard spheres (see for reference

[59]). The random packing of spheres has been studied very extensively due to the technological importance, and the opportunity to model the simple liquid, concentrated suspensions, amorphous and powder materials.

Computer simulation of packing problems can be classified into three groups of methods: molecular dynamic, Monte Carlo, and dense random packing. Much progress in the theory of the dense random packing has been made by the use of two kinds of methods: the sequential generation models and the collective rearrangement models. In the sequential model (see for reference [59]), so-called cluster growth model, a particle added to the surface of the particle cluster which grows outwards is placed sequentially to the point closest to the original such that the new particle established contact with three existing spheres in the cluster. Overlapping is ruled out by checking the center-center distance of the particle. The phenomenological character of the construction algorithm posed by the particle cluster from the initial term containing three particles leads to the inhomogeneous and anisotropic inclusion fields with a different density. Moreover, the configurations generated do not demonstrate the characteristic split-second peak in the radial distribution function observed in the experimental packing. In the second part of the sequential generation models, called the model of “rigid sphere free-fall into a virtual box,” one particle is dropped vertically each time from the random point onto the surface of an existing particle cluster growing upward. The different densities were approached by introduction of the phenomenological parameter limiting the number of rotations of a fallen sphere up to its setting in the structure. The effects of boundaries of the virtual box are eliminated by introducing the conventional cyclic boundary conditions. The algorithms described belong to the class of static method where the particles are placed at a given time step and cannot thereafter move. For contrast, the dynamic methods assume the reorganization of whole packing due to the short- or

long-range interactions between particles. So, in collective rearrangement, model N points randomly distributed in a virtual box are assigned the radii and the random vector of moving. Each sphere is moved until there are no overlaps. Then the radii are increased, and the process is repeated until any further increase in radii or any displacement of the spheres create overlaps that cannot be eliminated (the references on the different versions of this method can be found in [59]). More recently, numerical simulations were performed to realize homogeneous and isotropic packing of spheres by various methods, for instance, assuming a hypothetical sphere having dual structure whose inner diameter defines the true density and the outer one a nominal density. An alternative approach eliminating boundary effects of the virtual box is based on the use of spherical boundary conditions instead of the periodic ones. There, one simulates hard disks (more exactly, a circular cap visualized as a contact lens on the surface of an eyeball) on the surface of the ordinary 3-D sphere and hard spheres on the “surface” of a 4-D hypersphere. The advantage of this procedure is that there is no preferential direction, and it is impossible to pack particles into perfect regular periodic configurations.

A close random ensemble of spheres has been studied for many years, and the following quantitative parameters are well known. Packing densities for close lattice packing are 0.9069 (triangular) in the case of disks packed into the plane and 0.7405 (fcc or hcp) in the case of spheres packed into R^3 . Model experiments were performed using steel balls of equal size randomly packed into the shaking containers while forthcoming extrapolating the measured densities to eliminate finite-size effects that provided the conventional value of random close packing, such as 0.6366. Random loose packing equal to 0.60 is observed at the gentle rolling of steel balls into the packing container without shaking. In two dimensions, the experimental numbers for close and loose random packing are estimated with less accuracy, $c=0.8225$ and

$c=0.601$ (see for reference [59]). It should be mentioned that in contradiction to the periodic packing, a random close packing is an ill-defined problem which has no unique theoretical definition, and its final states are protocol dependent in both the numerical simulation and experimental sense (see for details [50]).

In subsection 11.1, the quantitative descriptors of the dispersion of fibers in unidirectional composites will be analyzed in order to describe the pattern of fiber location as it really exists rather than as described by some assumed model. Since the structure of random packing is strongly dependent on the procedure of their generation, we will consider a few popular algorithms and their combinations adapted for obtaining most homogeneous configurations, and will compare the statistical parameters of configurations generated by the different methods. In subsection 11.2 one will estimate the dependence of effective elastic properties of fiber composites on the radial distribution functions estimated from the real experimental data as well as from the ensembles generated by the method proposed.

11.1 STATISTICAL DESCRIPTION AND NUMERICAL SIMULATION OF RANDOM STRUCTURE COMPOSITES

The widely used informative function describing the point distribution is a second-order intensity function $K(r)$ defined as the number of further points expected to locate within a distance r of an arbitrary point dividing on the number of points per unit area n . Since points lying outside the observation window w are not observed, it is known that the estimator for $K(r)$ should be corrected. The function $K(r)$ is obtained by averaging over all inclusions at each value of r . Due to the wide utilization of periodic boundary conditions at the numerical simulation of the random packing, an alternative *toroidal edge collection* is used in which rectangular regions w can be regarded as a torus so that points on opposite edges are considered to be closed. Then w is

considered as part of a grid of identical rectangles, forming a border of the pattern inside w , and the distances are measured from the point in the central rectangle w to the points in the surrounding periodic rectangles.

The radial distribution function (RDF), $g(r)$, playing a role similar to the variance in a classical analysis of random variables, is defined as the radial distribution of the average number of sphere centers per unit area in a spherical shell and can be estimated from second-order intensity factor as $g(r)=(2\pi r)^{-1}dK(r)/dr$. The RDF is related to the derivative of the $K(r)$, and therefore it is more sensitive to changes in the spatial order than is the $K(r)$ function.

Digital images of transverse sections through the fiber composite material were obtained by digitizing high-resolution optical micrographs using standard methods. Image processing was then carried out on the 1024 by 1024 digital images using a commercially available desktop software package (Adobe Photoshop 5.5) in conjunction with a plug-in Image Processing Tool Kit (IPTK 3.0 by John Russ, 1996-1999 Reindeer Games, Inc.).

Since the structures of random packing are strongly dependent on the procedure of their generation, we will consider a few popular algorithms and their combinations and compare the statistical parameters of configurations generated by the different methods.

Poisson distribution. If the radius spheres are small enough, then their placement is described by the stationary (or homogeneous) Poisson point process. Although the hypothesis of the Poisson set of centers of nonoverlapping spheres is not fulfilled for the finite radius of spheres, it can be sometimes used as a useful approximate description of an observed pattern. We recall that for Poisson distribution ($d=2$) $K(r)=\pi r^2$ and $g(r)=1$.

Hard core model (HCM). In this model (also called random sequential adsorption), the disks with radius a are placed one by one with the center positions $X=\mathbf{x}_1, \dots, \mathbf{x}_N$ being distributed

randomly and uniformly over the set of all points in a rectangular region w . One supposes that periodic boundary conditions, that is, w and X , are periodically replicated in all directions. If the new disk does not overlap already deposited disks, its position is fixed and does not move anymore; otherwise, it is rejected and another random center position is generated. The process is finished when either a preassigned packing fraction is achieved or when no particles can be added anymore (jamming limit), which occurs at a volume fraction $c = 0.55$ (2-D case) or $c = 0.38$ (3-D case). The HCM provides a more realistic reference model than a Poisson point process, in which arbitrary small distances between points are allowed. The advantage of the HCM as a protocol independence is sacrificed in the case of generation of the binary or polydisperse structures. The geometrical blocking effect and the process irreversibility leads to the configuration packing that is essentially different from corresponding equilibrium configuration. To prevent just this kind of low-density jam from occurring in the following model, we will shake the disks.

Hard core shaking model (HCSM). This is a sort of HCM generating increasing number of inclusions in a virtual box w , accompanied by the shaking process, by giving each disk a small random displacement independent of its neighbors' positions that make it possible to unlock the disks from the jamming configuration (taking place for HCM at $c = 0.55$), and allows them to find the most homogeneous and mixed arrangement. Various algorithms have been devised to simulate reordering due to shaking or vibration of dense packing, which reduces the volume concentration of the high-density jam configuration. The packing with a wide concentration of inclusions has been investigated less and necessitates some additional consideration. In Figure 81 the comparative analysis of the RDF $g(r)$ as a function of r estimated by the HCM and HCSM is presented for the fiber concentration $c = 0.5, 0.55$. The plot of $g(r)$ of the configuration generated by the HCM was obtained by averaging over 30 realizations; other curves correspond to one

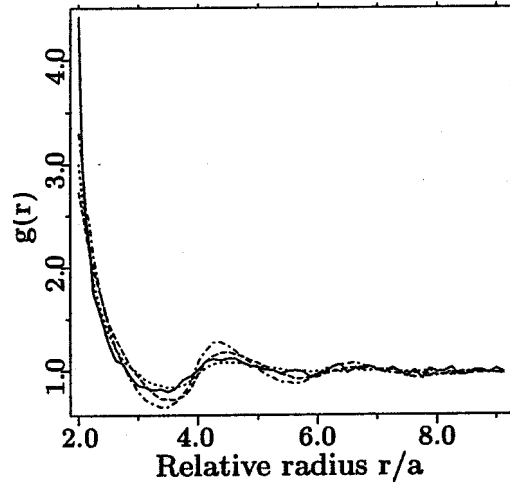


Figure 81. The Radial Distribution Functions $g(r)$ versus Relative Radius r/a Estimated by the HCM at $c=0.55$ (solid line) and $c=0.5$ (dotted line), and by HCSM at $c=0.55$ (dot-dashed line) and $c=0.5$ (dashed line).

realization. In so doing, the regular shaking procedure of the HCSM yields the fitting of averaging curves. As can be seen, the HCSM leads to more long-range ordering than HCM, and at the same c the RDF $g(r)$ for a small r is higher in the case of structure simulation by the HCM rather than by HCSM. It should be mentioned that for a population of finite-size fibers, a value of $g(r)$ higher than 1 does not necessarily imply that the fibers are clustered. The comparison of the histograms of the average number n_l of inclusions in the rectangular testing window $w_l^t = \{x: |x_l - x_{il}| < R_l, l=1,2\}$ ($R_l=3a$) is presented in Figure 82, from which we notice that the compromise of the shaking procedure with the modified HCM leads to a more homogeneous and mixed arrangement; the fraction $p(n_l)$ of the testing windows containing both the small and large numbers n_l of inclusions is diminished. Obviously, the descriptor n_l is a more sensitive measure of the local statistical homogeneity of the configuration analyzed than the RDF $g(r)$.

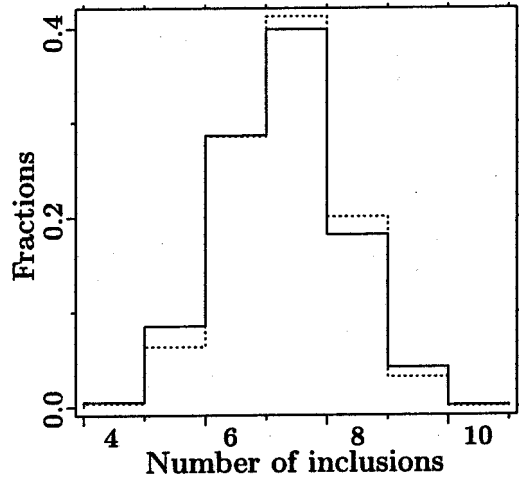


Figure 82. Histogram of Fractions $p(n_i)$ of Testing Window Containing n_i Inclusions Generated by the HCM (solid curve) and by the HCSM (dotted curve).

Monte Carlo shaking process. The Monte Carlo shaking process is, structurally, the most influential, and, computationally, the most intensive part of the whole packing process. The duration of this phase, which can be measured in terms of the number of Monte Carlo steps per particle, N^{MC}/N , can be changed by variation of the size of the shake-up window, the frequency ratio of the alternation of the processes in the generation of a new particle, and the shaking. However, the results of total simulation are not related trivially to the detailed separate stage. In Figure 83 we have plotted for one plausible input parameter set, the volume fraction against the length of Monte Carlo simulation N^{MC}/N . The HCM allows one to generate the random packing more steeply than the HCSM, only at the small particle concentration $c < 0.52$. As the packing density grows, the percent of trial nonaccepted generations dramatically increases in the vicinity of the jamming limit, and equals, for example, 99.998 percent at $c = 0.5445$ and $N = 3130$ with CPU time expended equal to five hours for a PC with a 644 MHz processor. At $c = 0.65$ the advantage of the HCSM comprising in creating more homogeneous configurations in comparison with the HCM (see Figure 82) degenerates. Additional shortcomings are the absence of the testing

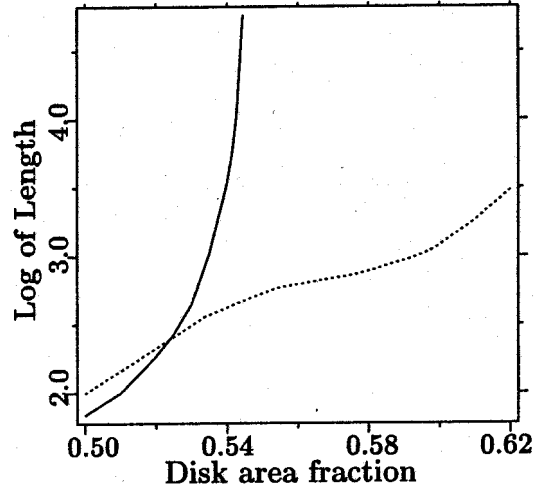


Figure 83. Length of Monte Carlo Simulation N^{MC}/N vs. an Area Fraction c Appropriate to the HCM (solid curve) and to the HCSM (dotted curve).

windows, with a small number of particles and a finite empty volume with a diameter more than $2a$. Thus, the HCSM stumbles on an intrinsic obstacle in the form of the jamming limits $c^{HCHM}=0.67$ that is more fuzzy than the jamming limit for the HCM, $c^{HCM}=0.55$. Forthcoming expansion of the particle concentration is possible through the utilization of the growth of the particle radius considered [60].

Initially periodic shaking model (IPSM). The periodic lattice packing $\mathbf{x}_m = m_1 \mathbf{e}_1 + m_2 \mathbf{e}_2$ of centers of the disks with the radius a was chosen as an initial system. Here \mathbf{e}_1 and \mathbf{e}_2 are linearly independent vectors. The rearrangement of initially periodic structure is conducted by the shaking procedure described in [59]. As can be seen in Figure 84, where $g(r)$ is estimated by IPSM with initial triangular packing of inclusions with different numbers of global shaking presented at $c=0.65$, the evaluation of RDF becomes stable if the numbers of global shaking are more than 50. In so doing, CPU time expended for one global shaking equals 10^3 sec. at $N=3700$, $R_t=3.1a$. Comparison of $g(r)$, estimated by IPSM with initial triangular and square packing of inclusions at 100 global shakings as well as by the HCSM, was estimated also at $c=0.65$, from which there is reason to believe that a sufficiently intensive shaking process eliminates the

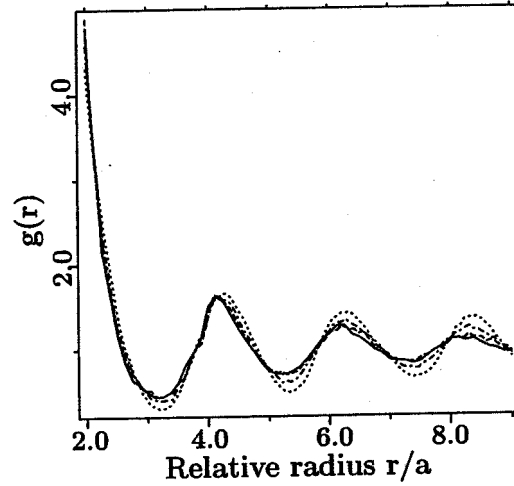


Figure 84. The Radial Distribution Functions $g(r)$ versus Relative Radius r/a Estimated by the IPSM at $c=0.65$, $N=3700$: 150 Shaking (solid curve), 100 Shaking (dashed curve), 30 Shaking (dot-dashed curve), 10 Shaking (dotted curve).

sensitivity of results obtained on the concrete algorithm of the simulation of the random inclusion ensemble, as well as on the initial arrangement of inclusions. Estimations of the real $g(r)$ are presented in Figure 85.

Collective rearrangement model (CRM). The CRM proposed in [60] leads to close packing. Because our goal is different and consists of the simulation of well-mixed random structures in a complete range of the inclusion concentration, some corrections of known algorithms summarized above were carried out. The modification lies in the fact that after a few steps of the estimation of the new velocities of colliding inclusions, both procedures in the generation of new inclusions in low-density testing windows and of inclusion shaking described in [59] are realized. It should be mentioned that modified CRM is not as optimal as an original CRM in the sense of modeling of close-packing configuration, simply because an added procedure of random shaking is just focused on the destruction of dense, locked local configurations in some testing windows and on the generation of most homogeneous structures. On the other hand, the support of the known simulation protocol by a shaking procedure has some

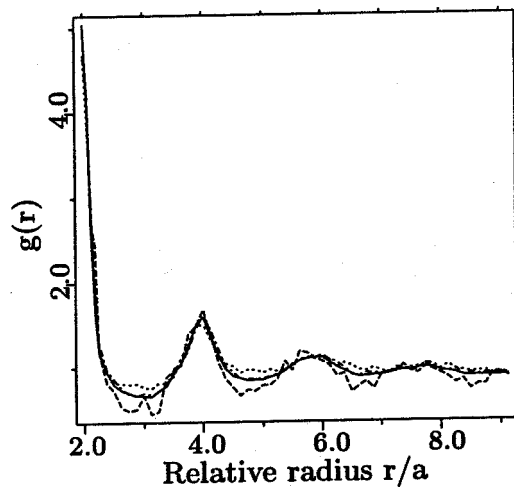


Figure 85. The Radial Distribution Functions $g(r)$ versus Relative Radius r/a : Single Sample 546-0181 (dashed curve), Averaged Over 10 Samples of 546-0161 (dotted curve), at $c=0.65$, Averaged Over 10 Samples of 546-0181 (dot-dashed curve), Averaged Over Eight Materials Produced by the Different Technological Regime (solid curve).

additional benefits. So, in the HCM, CRM, and sequential generation model, the parameters and functions are calculated only from one simulation of the generated configuration. Such data should be considered as just a single realization of a random generation process. To provide statistically more reliable results, it would be necessary to average several realizations. However, this repeating procedure is not necessary in the protocols accompanied by a shaking procedure because a configuration generated by a few global shakings can be regarded as a separate realization. Experiments and simulations give a suggestion of a transition between random and ordered configurations in the vicinity of a density $c=0.8$, where the density increases much more slowly beyond this point. The understanding of this transition is more obvious after quantitative analysis, shown in Figures 86 and 87, of the RDFs estimated by the modified CRM for different disk concentrations of $c=0.60-0.75$ and $c=0.75-0.90$, respectively. As can be seen for large disk concentration, the plot of the RDF has the characteristic split-second peak observed in the experimental packing, demonstrating the availability of large clusters with the triangular disk

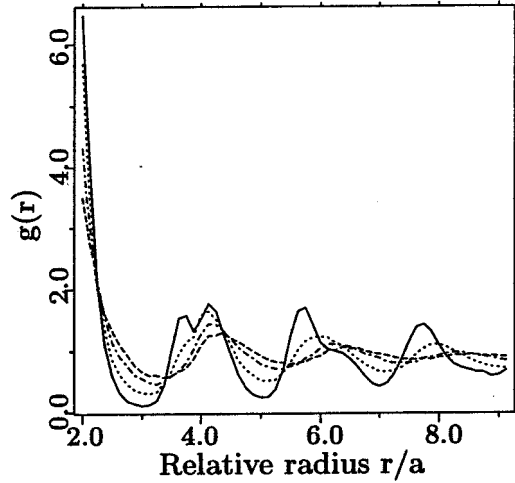


Figure 86. Radial Distribution Functions $g(r)$ versus Relative Radius r/a Estimated by the Modified CRM at $c=0.60$ (dashed curve), $c=0.65$ (dot-dashed curve), $c=0.70$ (dotted curve), $c=0.75$ (solid curve); N grows from 799 to 811.

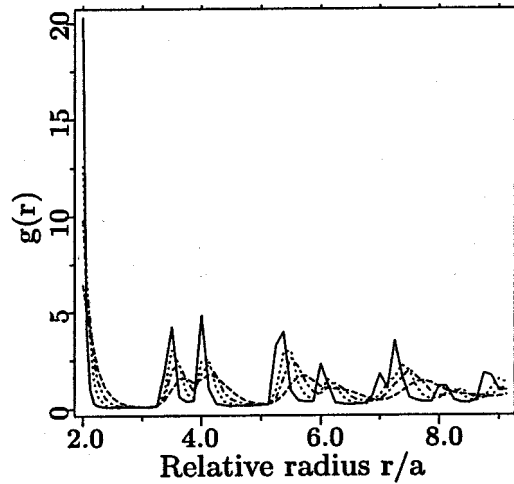


Figure 87. Radial Distribution Functions $g(r)$ versus Relative Radius r/a Estimated by the Modified CRM at $N=811$ and $c=0.90$ (solid curve), $c=0.85$ (dotted curve), $c=0.80$ (dot-dashed curve), $c=0.75$ (dashed curve).

packing. For analysis of peculiarity of the plots $g(r) \sim r$ in Figure 86, we will compare the coordinates of their peaks with the analogous peaks for close triangular and square packing. A distinguishing characteristic of the last regular packing is the availability of the fixed peaks corresponding to $r=2a, 4a, 6a, \dots$ and floating subpeaks, the location of which depends on the

specific structure of the unit cell. So, for the triangular and square packing, the coordinates of the subpeaks are $r=3.46a, 5.32a, \dots$ and $r=2.83a, 4.44a, 6.3a, \dots$, respectively. Imperfections, both in the identification of the ball centers and in the lattice itself, broaden the peaks and raise the heights of the intervening values. Thus, one can presuppose that the second subpeak in Figure 85 at $r=3.47a$ is caused by the influence of local ordering in the form of clusters with the triangular structure.

In Figure 88 we compared the RDF estimated from experimental data, numerical simulation by the CRM, as well as the RDF proposed in [54] and having analytical representation which takes into account a neighboring order in the distribution of the inclusions. The so-called well-stirred approximation of the RDF differs from the RDF for Poisson distribution by the availability of included volume, with the center \mathbf{x}_i where $g(r)=0$. Figure 88 shows a good fit of the RDFs estimated from experimental data and from numerical simulation by the modified CRM and their large dissimilarity from analytical representation of $g(r)$.

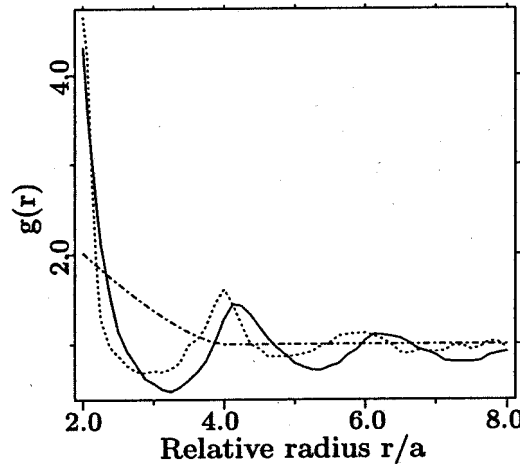


Figure 88. Radial Distribution Functions $g(r)$ versus Relative Radius r/a Estimated by the Numerical Simulation (solid curve), from Experimental Data (dotted curve), by the Analytical Approximation [54] (dot-dashed curve).

11.2 EFFECTIVE ELASTIC PROPERTIES

For a detailed discussion and numerous references of MEFM and related methods, readers are referred to [49]. Just for demonstration of the comparison of available experimental data with the predicting opportunity of the method proposed, we will consider the estimation of the effective elastic moduli L^* . Assume that the matrix is epoxy resin ($k^{(0)}=4.27$ GPa and $\mu^{(0)}=1.53$ GPa) that contains identical circular glass fibers ($k^{(1)}=50.89$ GPa and $\mu^{(1)}=35.04$ GPa). As can be seen from Figure 89, the use of the approach based on the quasicrystalline approximation (MT approach) leads to an underestimation of the effective shear modulus by 1.85 times for $c=0.7$, compared to the experimental data as well as to the more exact approximation of the MEFM, which provides a good comparison with experimental data [55]. In so doing, the best fitting is provided by the RDF simulated by the modified CRM.

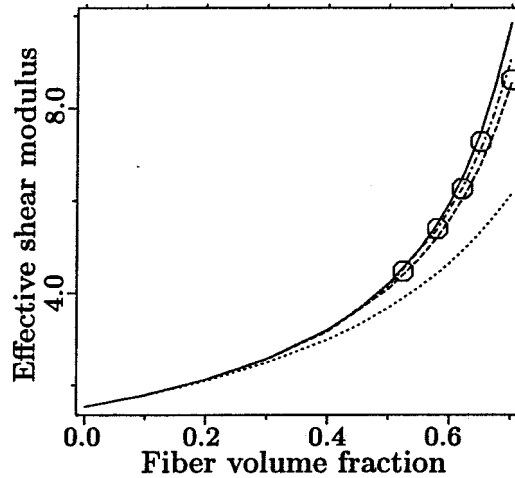


Figure 89. Variation of the Effective Shear Modulus μ^* as a Function of a Concentration of the Inclusions c . Experimental data \circ and curves calculated by the MEFM and $g(r)$ [54] (solid line), by MEFM with the RDF simulated by the modified CRM (dot-dashed line), by the MEFM with well steered $g(r)$ (dashed curve), and by the Mori-Tanaka method (dotted line).

Let us now demonstrate the application of the theoretical results by considering an isotropic composite made of an incompressible isotropic matrix, filled with rigid circle

inclusions of one size. This example was chosen deliberately because it provides the maximum difference of predictions of effective elastic response estimated by various methods. In Figure 90 the most advanced micromechanical model is analyzed for the different RDFs. As can be seen, the effective shear moduli can differ by a factor of two or more for the different RDFs. In so doing, the RDF simulated by the modified CRM provides the estimations of $\mu^*/\mu^{(0)}$ that are very close to those obtained by the real RDF at $c=0.65$. It is interesting to note that all RDFs lead to the infinite values of μ^* for large values of c , but the simulated RDF provides a limiting upper value of $c=0.72$.

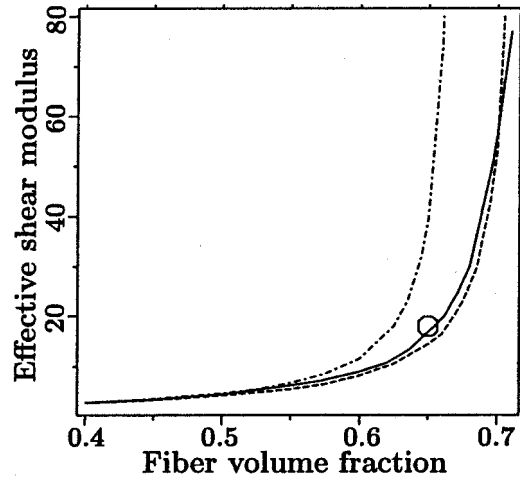


Figure 90. Variation of the Relative Effective Shear Modulus $\mu^*/\mu^{(0)}$ as a Function of a Concentration of the Inclusions c Estimated by the MEFM with $g(r)$ [54] (dot-dashed line), by the MEFM with the RDF Simulated by the Modified CRM (solid curve), by the MEFM with Well Steered $g(r)$ (dashed curve), and by the MEFM with Experimentally Estimated RDF \circ .

11.3 SUMMARY AND RECOMMENDATIONS

It should be mentioned that for computer-simulated configurations, the particle reorganization induced by shaking is subjected only to geometrical constraints, whereas for real structures, the packing is far more complicated and caused by the elastic, hydrodynamic, and cohesive forces and others. Our simulation technique is able to isolate the fundamental

geometrical constraints from other physics-mechanical and chemical effects, and the results provide a valuable benchmark for evaluating sophisticated packing schemes used to model real composite materials. It was shown that a sufficiently intensive shaking process leads to the stabilization of statistical distribution of the structure simulated that is most homogeneous, mixed and protocol independent (in the sense that the statistical parameters estimated do not depend on the basic simulated algorithm such as HCM, CRM, or other). The arguments justified in the last statement are plausible rather than rigorous and require additional investigation.

It is known that taking only one point probability density (volume fraction) into account can provide just a rough estimation of bounds of effective properties and statistical averages of stresses in the constitutive equations of composite materials. More informative characteristics of the point set are obtained using statistical second-order quantities (such as two-point probability density, second-order intensity function, and nearest neighbor distribution) which examine the association of a point relative to other points. Few contributions have paid attention to the application of these statistical distributions for generation of concrete realization of locations of a final number of interacting inclusions with their forthcoming elastic analysis. More rigorous estimation of statistical average of stress fields in the constituents and, therefore, of effective elastic moduli are based on the statistical averaging of random integral equations involved with the infinite number of inclusions whose configurations are described by the statistical second-order functions (see for reference [49,50]). In particular, in this study we demonstrated the strong dependence of effective moduli on the concrete form of radial distribution function and demonstrated strong differences between apparently similar distributions.

It should be mentioned, however, that estimation of effective elastic moduli is a linear problem with respect to the stress field analyzed, which is less sensitive to the local stress

distribution than nonlinear micromechanical problems of elastoplastic deformation, fracture, and fatigue of composite materials. Therefore, the author [49] estimated the second moment of stresses averaged over the volume of the constitutives by the use of the RDF with their application for the analysis of a wide class of nonlinear problems. These estimations of second moments of stress are defined by both the random stress fluctuations in the components and the inhomogeneity of the stress fields in the constituents that cannot be separated in the framework of the method proposed. There are a few models (see for reference [59]) based on the idea that at high inclusion concentration, the effective properties are dominated by the interaction forces between neighboring particles that are proportional to the ratio of the mean gap between neighboring particles to particle diameter. Obviously, the use of the average value as a mean gap instead of random distribution leads to the loss of statistical information about microtopology of the composite and is conceptually questionable, because the estimation problem of the average of the output parameter (such as effective properties) by the use of the average of the random input parameter (such as nearest neighbor distance) is essentially nonlinear. The approach by [61] based on the elastic solution for two interacting inclusions in an infinite matrix with forthcoming averaging is more in perspective, because it is more sensitive to the local configuration of inclusions. In so doing, the crude assumption by [61] that two inclusions are subjected to the external loading can be relaxed by the use of more accurate estimations by [49] of the correlation function of the effective field acting on two inclusions and fixed in the composite material. However, more detailed realization of this scheme is beyond the scope of the current study and will be considered in forthcoming publications by the authors.

PUBLICATIONS AND PRESENTATIONS

The following is a list of publications and presentations that were generated during this reporting period.

- (1) Bechel, V. T., & G. P. Tandon. (2001). *Interfacial Toughness Measurement for a Model SiC/Epoxy Composite*. Presented at SEM - X, San Diego, CA.
- (2) Bechel, V. T., C. Janke, M. Wilenski, & G. P. Tandon. (2001). Constituent Level Examination of an E-beam Cured Graphite/Epoxy Composite. *Proceedings 46th International SAMPE Symposium* (2115-2126).
- (3) Bechel, V. T., & G. P. Tandon. (2002, in preparation). Characterization of Interfacial Failure Using a Reflected Light Technique. To appear in *Experimental Mechanics*.
- (4) Bechel, V. T., & G. P. Tandon. (2002, in preparation). Modified Cruciform Test for Application to Graphite/Epoxy Composites. To appear in *Mechanics of Composite Materials and Structures*.
- (5) Buryachenko, V. A. (2001). Locality Principle and General Integral Equations of Micromechanics of Composite Materials. *Math. Mech. of Solids* 6 (299-321).
- (6) Buryachenko, V. A. (2001). Multiparticle Effective Field and Related Methods in Micromechanics of Random Composite Materials. *Math. Mech. of Solids* 6 (577-612).
- (7) Buryachenko, V. A., & N. J. Pagano. (2001, submitted). Multiscale Analysis of Multiple Interacting Inclusions Problem: Finite Number of Interacting Inclusions. *Int. J. Solid Str.*
- (8) Buryachenko, V. A. (2001). Multiparticle Effective Field and Related Methods in Micromechanics of Composite Materials. *Applied Mechanics Review* 54(1) (1-47).
- (9) Buryachenko, V. A., & N. J. Pagano. (2001, submitted). Nonlocal Models of Stress Concentrations and Effective Thermoelastic Properties of Random Structure Composites. *Int. J. Solid Str.*
- (10) Buryachenko, V. A., N. J. Pagano, R. Y. Kim, & J. E. Spowart. (2002, in preparation). Quantitative Description of Random Microstructures of Composites and their Effective Elastic Moduli. *Int. J. Solid Str.*
- (11) Buryachenko, V. A. (2001). *Micromechanics of Nonlocal Effects in Heterogeneous Materials*. Presented at Mechanics and Materials Summer Conference, La Jolla, CA.

- (12) Buryachenko, V. A., & N. J. Pagano. (2001). *Multiscale Modeling for Multi-interacting Inclusion Problems Including Edge Effect*. Presented at Mechanics and Materials Summer Conference, La Jolla, CA.
- (13) Foster, D. C., G. P. Tandon, N. J. Pagano, & M. Zoghi. (2001, November). *Failure Initiation in a Multi-Fiber Cruciform Specimen Under Transverse Loading*. Presented at Winter Annual Meeting of ASME, New York, NY.
- (14) Iarve, E. V., & W. Ragland. (2001). Scanning Electron Microscopy Investigation of Deformation in the Vicinity of a Mode II Crack Tip in Unidirectional Toughened Epoxy Composites. *Microscopy and Microanalysis Symposium* 7(2) (1122-1124).
- (15) Pagano, N. J., & G. P. Tandon. (2001, October). *Micromechanical Response of a Multi-Phase Composite*. Presented at 2001 Contractors Meeting for the AFOSR Program in Mechanics of Composite Materials and Structural Mechanics, Washington, DC.
- (16) Pochiraju, K. V., G. P. Tandon, & N. J. Pagano. (2001). Analyses of Single Fiber Pushout Considering Interfacial Friction and Adhesion. *Journal of the Mechanics and Physics of Solids* 49 (2307-2338).
- (17) Pochiraju, K. V., G. P. Tandon, & N. J. Pagano. (2001, November). *Coupled Multi-Physics Prediction of Residual Stress Development During Curing of Polymer Matrix Composites*. Presented at Winter Annual Meeting of ASME, New York, NY, Nov 11-16, 2001.
- (18) Sihm, S., & A. K. Roy. (2001). Modeling and Stress Analysis of Open-Cell Carbon Foam. *Proceedings of 46th Int. SAMPE Symposium*.
- (19) Sihm, S. (2001). Mechanical Analysis of Carbon Foam. *Proceedings of U.S.-Korea Conference on Science, Technology, and Entrepreneurship*.
- (20) Sihm, S., & D. Mollenhauer. (2001). Parametric Design, Analysis and Testing of a Model Woven Composite with a Cruciform Geometric Configuration. *Proceedings of 16th ASC Technical Conference*.
- (21) Sihm, S., & A. K. Roy. (2001, October). *Modeling and Testing of Carbon Foam*. Presented at the 3rd Carbon Foam Workshop, Materials and Manufacturing Directorate, Air Force Research Laboratory, Wright-Patterson AFB, OH.
- (22) Sihm, S. (2001, October). *Testing of MER Carbon Foam*. Presented at the 3rd Carbon Foam Workshop, Materials and Manufacturing Directorate, Air Force Research Laboratory, Wright-Patterson AFB, OH.
- (23) Sihm, S., & A. K. Roy. (2001). Modeling to Correlate Macroscopic Properties with Microstructure of Open-Cell Carbon Foam. *Proceedings of ASME Int. Mech. Eng. Congress & Expo*.

- (24) Tandon, G. P., D. Buchanan, N. J. Pagano, & R. John. (2001). Analytical And Experimental Characterization of Thermo-Mechanical Properties of a Damaged Woven Oxide-Oxide Composite. *Ceramic Engineering and Science Proceedings* 22(3) (687-694). 25th Annual International Conference on Advanced Ceramics and Composites, American Ceramic Society.
- (25) Tandon, G. P., R. Y. Kim, & V. T. Bechel. (2001). Mixed-Mode Failure Criteria Using Cruciform Geometry. *Proceedings of 16th Annual ASC Technical Conference*.
- (26) Tandon, G. P., R. Y. Kim, & B. P. Rice. (2001, September). *Analyzing Nanocomposites Using Continuum Mechanics Approaches*. Presented at Air Force Workshop on Nanocomposites, Blacksburg, VA.
- (27) Tandon, G. P., & R. Y. Kim. (2001). Damage Evolution and Failure Modeling in Unidirectional Graphite/Epoxy Composite. *Proceedings of 2001 ASME International Mechanical Engineering Congress and Exposition, IMECE2001/AD-25302*.
- (28) Tandon, G. P., R. Y. Kim, & V. T. Bechel. (2001, submitted). Fiber-Matrix Interfacial Failure Characterization Using a Cruciform-Shaped Specimen. *Journal of Composite Materials*.

REFERENCES

1. Tandon, G. P., R. Y. Kim, & V. T. Bechel. (2001, Sep). *Mixed-Mode Failure Criteria Using Cruciform Geometry*. Presented at 16th Annual Technical Conference of the American Society for Composites, Blacksburg, VA.
2. Bechel, V. T., & N. R. Sottos. (1998). Application of Debond Length Measurements to Examine the Mechanics of Fiber Pushout. *J. Mech. Phys. Solids* 46(9) (1675-1697).
3. Bechel, V. T., & G. P. Tandon. (2001, submitted). Characterization of Interfacial Failure Using a Reflected Light Technique. *Experimental Mechanics*.
4. *ABAQUS Theory Manual for Version 5.7*. (1997). Pawtucket, RI: Hibbitt, Karlsson, and Sorenson, Inc.
5. Whitney, J. M., & R. J. Nuismer. (1974). Stress Fracture Criteria for Laminated Composites Containing Stress Concentrations. *Journal of Composite Materials* 8 (253-265).
6. Tandon, G. P., R. Y. Kim, R. Y., & V. T. Bechel. (2000). Evaluation of Interfacial Normal Strength in SCS-0/Epoxy Composite Using Cruciform Specimen. *Composites Science and Technology* 60 (2281-2295).
7. Warriar, S. G., B. S. Majumdar, & D. B. Miracle. (1997). Determination of the Interface Failure Mechanism During Transverse Loading of Single Fibre SiC/Ti-6Al-4V Composites from Torsion Tests. *Acta Mater.* 45(1) (309-320).
8. Pagano, N. J. (1991). Axisymmetric Micromechanical Stress Fields in Composites. *Proceedings 1991 IUTAM Symposium on Local Mechanics Concepts for Composite Material Systems* (1-26). Springer, Verlag.
9. Pagano, N. J., & G. P. Tandon. (1994). 2-D Damage Model for Unidirectional Composites Under Transverse Tension and/or Shear. *Mechanics of Composite Materials and Structures* 1 (119-155).
10. *Hercules Product Data Sheet Number 868-2*. (1991). Hercules Advanced Materials and Systems Company, Composite Product Group, Magna, Utah.
11. Pagano, N. J., & G. P. Tandon. (1988). Elastic Response of Multi-Directional Coated-Fiber Composites. *Composites Science and Technology* 31 (273-293).
12. Pagano, N. J., & H. W. Brown, III. (1993). The Full-Cell Cracking Mode in Unidirectional Brittle-Matrix Composites. *Composites* 24 (69-83).
13. Weng, G. J. (1984). Some Elastic Properties of Reinforced Solids, with Special Reference to Isotropic Ones Containing Spherical Inclusions. *Int. J. Eng. Sci.* 22(7) (845-856).

14. Weng, G. J., & H. H. Pan. (1992). Thermal Stress and Volume Change During a Cooling Process Involving Phase Transformation. *J. Thermal Stress* 15 (1-23).
15. Norris, A. N. (1989). An Examination of the Mori-Tanaka Effective Medium Approximation for Multiphase Composites. *J. Applied Mechanics* 56 (83-88).
16. Naik, R. A. (1994). Analysis of Woven and Braided Fabric Reinforced Composites. *NASA Contractor Report 194930*. NASA Langley Research Center, Hampton, VA.
17. Schoeppner, G. A., & N. J. Pagano. (1998). Stress Fields and Energy Release Rates in Cross-Ply Laminates. *Int. J. Solids & Structures* 35 (1025-1055).
18. Pagano, N. J. (1974). Exact Moduli of Anisotropic Laminates. In L. J. Broutman and R. H. Krock, eds., *Composite Materials, Vol. 2: Mechanics of Composite Materials* (G. P. Sendeckyj, ed.) (23-44).
19. John, R., D. J. Buchanan, & L. P. Zawada. (2000). *Notch-Sensitivity of a Woven Oxide/Oxide Ceramic Matrix Composite* (ASTM STP 1392). In M. G. Jenkins, E. Lara-Curzio, and S. T. Gonczy, eds., American Society for Testing and Materials, West Conshohocken, PA (172-181).
20. Lu, T. J., & J. W. Hutchinson. (1995). Effect of Matrix Cracking on the Overall Thermal Conductivity of Fibre-Reinforced Composites. *Phil. Trans. R. Soc. Lond. A* 351 (595-610).
21. Islam, MD. R., & A. Pramila. (1999). Thermal Conductivity of Fiber Reinforced Composites by the FEM. *J. Composite Materials* 33 (1699-1715).
22. Pochiraju, K. V., G. P. Tandon, & N. J. Pagano. (2001). Analyses of Single Fiber Pushout Considering Interfacial Friction and Adhesion. *Journal of the Mechanics and Physics of Solids* 49 (2307-2338).
23. Roy, A. K. (1996). In Situ Damage Observation and Failure in Model Laminates Containing Planar Yarn Crimping of Woven Composites. *Mechanics of Composite Materials and Structures* 3 (101-117).
24. Pullman, D., & J. R. Schaff. (1996). Three Dimensional Spline Variational and Finite Element Theory: A Comparison for a Laminate with a Circular Hole. *Proceedings of ASC Technical Conference* (20-29).
25. Iarve, E. V. (1996). 3-D Asymptotic and B-Spline Based Numerical Analysis. *Proceedings of ASC Technical Conference* (1086-1095).
26. Iarve, E. V. (1996). Spline Variational Three Dimensional Stress Analysis of Laminated Composite Plates with Open Holes. *International Journal of Solids and Structures* 33(14) (2095-2118).

27. Sihh, S., & A. K. Roy. (2000, November). *Prediction of Stiffness and Strength of Plain Weave Composites by Mixed Finite Element Method*. Presented at 2000 ASME International Mechanical Engineering Congress & Exposition, Orlando, FL.
28. Post, D., B. Han, B., & P. Ifju. (1994). *High Sensitivity Moiré: Experimental Analysis for Mechanics and Materials*. New York: Springer-Verlag Inc.
29. Lassahn, G., P. Taylor, V. Deason, & J. Lassahn. (1994). Multiphase Fringe Analysis with Unknown Phase Shifts. *Optical Engineering* 33(6) (2039-2044).
30. Pagano, N. J. (1978). Stress Fields in Composite Laminates. *International Journal of Solids and Structures* 14 (385-400).
31. Pagano, N. J. (1978). Free Edge Stress Field in Composite Laminates. *International Journal of Solids and Structures* 14 (401-406).
32. Wang, S. S., & I. Choi. (1982). Boundary-Layer Effects in Composite Laminates: Part 1, Free-Edge Stress Singularities. *Journal of Applied Mechanics* 49 (541-560).
33. Folias, E. S. (1992). On the Interlaminar Stresses of a Composite Plate Around the Neighborhood of a Hole. *International Journal of Solids and Structures* 25 (1193-1200).
34. Wang, S. S., & X. Lu. (1993). Three-Dimensional Asymptotic Solutions for Interlaminar Stresses Around Cutouts in Fiber Composite Laminates. *Mechanics of Thick Composites, AMD-Vol. 1962* (41-50).
35. Iarve, E. V. (1996). Spline Variational Three-Dimensional Stress Analysis of Laminated Composite Plates with Open Holes. *Int. J. of Solids and Structures* 44(14) (2095-2118).
36. Pullman, D., & J. R. Schaff. (1996). Three Dimensional Spline Variational and Finite Element Theory: A Comparison for a Laminate with a Circular Hole. *Proceedings of ASC Technical Conference* (20-29).
37. Peters, S. T. (1998). *Handbook of Composites* (2nd Edition, 258-259). London: Chapman & Hall.
38. Rogers, D. K., et al. (2000). Low-Cost Carbon Foams for Thermal Protection and Reinforcement Applications. *Proceedings of 45th Int. SAMPE Symposium*.
39. Warren, W. E., & A. M. Kraynik. (1988). The Linear Elastic Properties of Open-Cell Foams. *Journal of Applied Mechanics* 55 (341-346).
40. Bikerman, J. J. (1973). *Foams* (33-64). New York: Springer-Verlag.
41. Roy, A. K., & J. D. Camping. (2002). Development of a Portable Shear Test Fixture for Low Modulus Porous (Foam) Materials. Manuscript under review.

42. Roy, A. K. (2000). Measuring Poisson's Ratio of Carbon Foam by Optical Microscopy. *Proceedings of the 15th ASC Conference*.
43. Tsai, S. W. (1992). *Theory of Composites Design*. Dayton, OH: Think Composites.
44. Jeon, H. G., et al. (2001). Investigations of Novel Methods to Extend the Use Temperatures of Polymers. Wright-Patterson Air Force Base, OH.
45. O'Brien, T. K. (1998). Composite Interlaminar Shear Fracture Toughness, G_{IIC} : Shear Measurement or Shear Myth. In R. B. Bucinell, ed., *Composite Materials Fatigue and Fracture 7* (ASTM STP 1330) (3-18).
46. O'Brien, T. K. (1998). Interlaminar Fracture Toughness: the Long and Winding Road to Standardization. *Composites Part B* (57-62).
47. Corleto, C., W. Bradley, & M. Henriksen. (1987). Correspondence between Fields and Damage Zones Ahead of Crack Tip of Composites Under Mode I and Mode II Delamination. *ICCM-VI Proceedings 3* (378-387).
48. Buryachenko V. A., & N. J. Pagano. (2001, submitted). Nonlocal Models of Stress Field Concentrations and Effective Thermoelastic Properties of Random Structure Composites. *Int. J. Solids Structures* 25.
49. Buryachenko, V. A. (2001). Multiparticle Effective Field and Related Methods in Micromechanics of Composite Materials. *Appl. Mech. Reviews* 54 (1-47).
50. Torquato, S. (2001). *Random Heterogeneous Materials: Microstructure and Macroscopic Properties*. New York: Springer-Verlag.
51. Buryachenko, V. A. (1998). Some Nonlocal Effects in Graded Random Structure Matrix Composites. *Mech. Res. Commun.* 25 (117-122).
52. Buryachenko, V. A., & F. G. Rammerstorfer. (1998). Micromechanics and Nonlocal Effects in Graded Random Structure Matrix Composites. *IUTAM Symp. On Transformation Problems in Composite and Active Materials* (197-206) (eds. Y.A. Bahei-El-Din and G. J. Dvorak). Dordrecht: Kluwer Academic Publ.
53. Buryachenko, V. A. (1999). Effective Thermoelastic Properties of Graded Doubly Periodic Particulate Composites in Varying External Stress Fields. *Int. J. Solids Structures*. 36 (3861-3885).
54. Torquato, S., & F. Lado. (1992). Improved Bounds on the Effective Elastic Moduli of Random Arrays of Cylinders. *ASME. J. Appl. Mech.* 59 (1-6).
55. Lee, J. A., & D. L. Mykkanen. (1987). *Metal and Polymer Matrix Composites*. New York: Noyes Data Corporation.

56. J. Quintanilla, & S. Torquato. (1987). Microstructure Functions for a Model of Statistically Inhomogeneous Random Media. *Phys. Rev. E* 55 (1558-1565).
57. Taya, M. (1990). Some Thoughts on Inhomogeneous Distribution of Fillers in Composites. *Micromechanics and Inhomogeneity* (433-447). The Toshio Mura 65th Anniversary Volume (eds. G. J. Weng, M. Taya, H. Abe). New York: Springer-Verlag.
58. Yang, S., A. M. Gokhale, & Z. Shan. (2000). Utility of Microstructure Modeling for Simulation of Micromechanical Response of Composites Containing Nonuniformly Distributed Fibers. *Acta Materialia* 48 (2307-2322).
59. Buryachenko, V. A., N. J. Pagano, R. Y. Kim, & J. E. Spowart. (2001, in preparation). Quantitative Description and Numerical Simulation of Random Microstructures of Composites and their Effective Elastic Moduli.
60. Lubachevsky, B. D., F. H. Stillinger, & E. N. Pinson. (1991). Disks vs. Spheres: Contrasting Properties of Random Packing. *J. Statistical Phys.* 64 (501-524).
61. Pyrz, R. (1994). Quantitative Description of the Microstructure of Composites, Part I: Morphology of Unidirectional Composite Systems. *Composites Sci. Technology* 50 (197-208).

LIST OF ACRONYMS

ADM	axisymmetric damage model
AE	acoustic emission
B-SAM	B-spline analysis method
CRM	collective rearrangement model
ENF	end notch flexure
E-SEM	environmental scanning electron microscope
FE	finite element
FEA	finite element analysis
FEM	finite element method
FTM	Fourier transform method
HCM	hard core model
HCSM	hard core shaking model
IM	iteration method
IPSM	initially periodic shaking model
LBC	ligament boundary conditions
MEFM	multiparticle effective field method
MT	Mori-Tanaka
NDE	nondestructive evaluation
OBC	overall loading/boundary conditions
RDF	radial distribution function
SEM	scanning electron microscope